

UCLA School of Engineering and Applied Science

AD-A263 759



"Planar Active Antennas and Quasi-Optical Power Combining Arrays
Using FET's and Slots"

By: Shigeo Kawasaki and Tatsuo Itoh
Electrical Engineering Department

United States Army Research Office
Contract Number DAAH 04-92-C-0068

UCLA Report Number ENG 92-22

DTIC
ELECTE
MAY 05 1993
S E



~~RESTRICTED~~ STATE
Approved for public release
Distribution Unlimited

REPORT DOCUMENTATION PAGE

1a. REPORT SECURITY CLASSIFICATION Unclassified		1b. RESTRICTIVE MARKINGS	
2a. SECURITY CLASSIFICATION AUTHORITY		3. DISTRIBUTION/AVAILABILITY OF REPORT Approved for public release; distribution unlimited.	
2b. DECLASSIFICATION/DOWNGRADING SCHEDULE		5. MONITORING ORGANIZATION REPORT NUMBER(S) ARO 30921-1-EL	
4. PERFORMING ORGANIZATION REPORT NUMBER(S) UCLA Report No. ENG-93-22		7a. NAME OF MONITORING ORGANIZATION U. S. Army Research Office	
6a. NAME OF PERFORMING ORGANIZATION The University of Texas / UCLA	6b. OFFICE SYMBOL (If applicable)	7b. ADDRESS (City, State, and ZIP Code) P. O. Box 12211 Research Triangle Park, NC 27709-2211	
6c. ADDRESS (City, State, and ZIP Code) 405 Hilgard Avenue Los Angeles, CA 90024		9. PROCUREMENT INSTRUMENT IDENTIFICATION NUMBER DAAH04-93-G-0068	
8a. NAME OF FUNDING/SPONSORING ORGANIZATION U. S. Army Research Office	8b. OFFICE SYMBOL (If applicable)	10. SOURCE OF FUNDING NUMBERS	
8c. ADDRESS (City, State, and ZIP Code) P. O. Box 12211 Research Triangle Park, NC 27709-2211		PROGRAM ELEMENT NO.	PROJECT NO.
		TASK NO.	WORK UNIT ACCESSION NO.
11. TITLE (Include Security Classification) Planar Active Antennas and Quasi-Optical Power Combining Arrays Using FET's and Slots			
12. PERSONAL AUTHOR(S) Shigeo Kawasaki and Tatsuo Itoh			
13a. TYPE OF REPORT	13b. TIME COVERED FROM TO	14. DATE OF REPORT (Year, Month, Day) 1993, March 20	15. PAGE COUNT 143
16. SUPPLEMENTARY NOTATION The view, opinions and/or findings contained in this report are those of the author(s) and should not be construed as an official Department of the Army position, policy, or decision, unless so designated by other documentation.			
17. COSATI CODES		18. SUBJECT TERMS (Continue on reverse if necessary and identify by block number)	
FIELD	GROUP	SUB-GROUP	
		Active Antenna, Quasi-Optical Technique	
		Optical Control, Spatial Power Combiner	
19. ABSTRACT (Continue on reverse if necessary and identify by block number) This report presents design concepts and experimental data of planar active antenna and quasi-optical power combining arrays with strong coupling to realize a compact and low-cost radar and communication system. The prototype circuits for this purpose were made in a layered configuration using microstrip lines and in a uniplanar structure using CPW's. As an active source, an FET was selected. As a unit cell of the power combining array, a single layered active antenna using microstrip lines and slots was fabricated. In the design, small signal S-parameters were used to determine the circuit configuration while a large signal analysis to the entire circuit involving the slot antenna input impedance was carried out. The circuit designed for 10 GHz was found to operate at 9.3 GHz and the other designed for 25 GHz at 24 GHz. In addition, the circuit with CPW's and slot designed for 10 GHz was found to operate at 8.6 GHz. Based on these successful results, (cont'd)			
20. DISTRIBUTION/AVAILABILITY OF ABSTRACT <input type="checkbox"/> UNCLASSIFIED/UNLIMITED <input type="checkbox"/> SAME AS RPT <input type="checkbox"/> DTIC USERS		21. ABSTRACT SECURITY CLASSIFICATION Unclassified	
22a. NAME OF RESPONSIBLE INDIVIDUAL Tatsuo Itoh		22b. TELEPHONE (Include Area Code) (310)206-4820	22c. OFFICE SYMBOL

(cont'd)

linear power combining arrays were made. For the strong coupling, each oscillator output is connected by a single transmission line. Several 6-element microstrip arrays and a 4-element CPW array were fabricated. In the former, sharp main beams were obtained. To obtain a millimeter-wave operating frequency, the second harmonic spatial power combining array made with FET's were demonstrated around 40 GHz. To show a topology of a 2-dimensional array, a 16-element dual polarized array at 7.8 GHz was made. To obtain the maximum in-phase radiation signal, impedance matching, a phase of the radiation signal and a signal phase of each oscillator were taken into account. As a variation of the active antenna, an active antenna integrated with reactive FET's was made and optical control of the active integrated antenna was investigated. In the former, a wide-band slot antenna was realized. In the latter, the maximum tuning range of 70 MHz around 8.8 GHz was obtained from a 2-element CPW active integrated antenna with floating gates. Future research directions were suggested for applications and analysis.

ABSTRACT

This report presents design concepts and experimental data of planar active antenna and quasi-optical power combining arrays with strong coupling to realize a compact and low-cost radar and communication system. The prototype circuits for this purpose were made in a layered configuration using microstrip lines and in a uniplanar structure using CPW's. As an active source, an FET was selected. As a unit cell of the power combining array, a single layered active antenna using microstrip lines and slots was fabricated. In the design, small signal S-paramaters were used to determine the circuit configuration while a large signal analysis to the entire circuit involving the slot antenna input impedance was carried out. The circuit designed for 10 GHz was found to operate at 9.3 GHz and the other designed for 25 GHz at 24 GHz. In addition, the circuit with CPW's and slot designed for 10 GHz was found to operate at 8.6 GHz. Based on these successful results, linear power combining arrays were made. For the strong coupling, each oscillator output is connected by a single transmission line. Several 6-element microstrip arrays and a 4-element CPW array were fabricated. In the former, sharp main beams were obtained. To obtain a millimeter-wave operating frequency, the second harmonic spatial power combining array made with FET's were demonstrated around 40 GHz. To show a topology of a 2-dimensional array, a 16-element dual polarized array at 7.8 GHz was made. To obtain

the maximum in-phase radiation signal, impedance matching, a phase of the radiation signal and a signal phase of each oscillator were taken into account. As a variation of the active antenna, an active antenna integrated with reactive FET's was made and optical control of the active integrated antenna was investigated. In the former, a wide-band slot antenna was realized. In the latter, the maximum tuning range of 70 MHz around 8.8 GHz was obtained from a 2-element CPW active integrated antenna with floating gates. Future research directions were suggested for applications and analysis.

Contents

Abstract	iii
Contents	v
List of Figures	ix
List of Tables	xiv
List of Symboles	xv
Chapters	
I Introduction	1
Part 1 : Active Antenna and Power Combining Array	9
II Planar Active Antenna	9
2.1 Oscillator Design	9
2.1.1 1-port Oscillator	9
2.1.2 2-port Negative Resistance Oscillator	14
2.1.3 FET Oscillator	17
2.2 Slot Radiator	20
2.2.1 Modified Booker's Formula	20
2.2.2 Dipole Antenna	21
2.2.3 Slot Radiator in Planar Active Antenna	25
2.3 Measured Characteristic	29
2.3.1 Isotropic Conversion Gain and ERP	29
2.3.2 Antenna Pattern and Tuning Range	29

2.4	Layered and Uniplanar Active Antenna	30
2.4.1	Design of Layered Active Antenna	30
2.4.2	CPW Active Antenna Configuration	34
2.4.3	Experimental Results	36
III	Linear Quasi-Optical Power Combining Array	40
3.1	Power Combining Array Design	40
3.1.1	Array	40
3.1.2	Power Combiner	41
3.2	Circuit Modeling	45
3.2.1	Periodic Boundary	45
3.2.2	Passive Part	46
3.2.3	Large Signal Analysis	51
3.3	2-element Array	55
3.3.1	Configuration	55
3.3.2	Experimental Results	57
3.4	6-element Linear Array	59
3.4.1	Configuration	59
3.4.2	Experimental Results	60
3.4.3	Empty Oscillator Array	64
3.5	Second Harmonic Spatial Power Combining Array	66
3.5.1	Concept	66
3.5.2	Configuration	67
3.5.3	Experimental Results	71
IV	2-dimensional Quasi-Optical Power Combining Array	77

4.1 Array with 1 Oscillator and 4 Slots	77
4.1.1 Configuration	77
4.1.2 Experimental Results	78
4.2 2x2 Array	81
4.2.1 Configuration	81
4.2.2 Analysis	84
4.2.3 Experimental Results	89
4.3 16-element Array	91
4.3.1 Configuration	91
4.3.2 Experimental Results	93
4.3.3 Analysis of 16-element Array	95
Part 2 : Variation of Quasi-Optical Technique	97
V FET Passive Component	97
5.1 Reactive FET Design	97
5.1.1 Design Criteria	97
5.1.2 Experimental Results of Reactive FET	98
5.2 Wide-band Slot Antenna and Active Integrated Antenna with Reactive FET	101
5.2.1 Operation Concept	101
5.2.2 Experimental Results	103
VI Optical Control of Active Integrated Antenna	106
6.1 Photo Detection	106
6.1.1 Photodetector	106

6.1.2 Illumination Effect on FET	107
6.2 Optically Controlled Reactive FET	112
6.2.1 Configuration	112
6.2.2 Experimental Results	114
6.3 Optical Tuning Range of Active Integrated Antenna	117
6.3.1 Circuit Configuration	117
6.3.2 Electrical and Optical Tuning Range	117
6.3.3 Antenna Pattern	122
6.4 2-element Optically Controlled Uniplanar Linear Array	123
6.4.1 Configuration	123
6.4.2 Experimental Results	125
 VII Conclusions	 131
7.1 Summary	131
7.2 Suggestions for Future Research	135
 Bibliography	 138

List of Figures

1.1 Category of Quasi-Optical Power Combining Array	4
2.1 1-port Negative Resistance Oscillator	10
2.2 Negative Resistance Variation of Active Device in Series Circuit Model	11
2.3 Parallel Circuit Model of Active Device and Negative Conductance Variation	12
2.4 Device and Load Line Locus	13
2.5 Two-port Oscillator	15
2.6 Negative Resistance FET Oscillator	18
2.7 Circuit Model with R_i for Large Signal Analysis	19
2.8 Input Impedance of Slot Antenna with Normalized Wavelength	27
2.9 Crossing Slot in Ground Plane of Microstrip Line Circuit	28
2.10 Definition of Isotropic Conversion Gain	30
2.11 Configuration of Single Active Antenna	31
2.12 Large Signal Model for Single Active Antenna	32
2.13 Variation of $R=V_{fb}/V_{in}$ of Single Active Antenna	33
2.14 Configuration of Single Uniplanar Active Antenna	35
2.15 CPW Active Antenna with Tuning Stub	36
2.16 Antenna Pattern Comparison of Microstrip Active Antenna	37
2.17 Stub Length Dependence of Oscillation Frequency and Tuning Range	39

3.1 Feed Network for Two Slots	42
3.2 Signal Flow for Two Unit Cells	45
3.3 Configuration of Infinite Array with Periodic Structure	47
3.4 Transmission Line Model for Reduced Infinite Array	48
3.5 Input Impedance of Passive Part of Reduced Infinite Periodic Array	51
3.6 Circuit Model of Reduced Infinite Periodic Array	52
3.7 Variation of R for Reduced Infinite Array	53, 54
3.8 2-element E-plane Microstrip Array	55
3.9 2-element H-plane CPW Array	56
3.10 Radiation pattern of 2-element Microstrip Array	58
3.11 Radiation pattern of 2-element CPW Array	59
3.12 6-element Periodic Linear Quasi-Optical Power Combining Array Using Microstrip Lines	61
3.13 6-element Nonperiodic Linear Quasi-Optical Power Combining Array Using Microstrip Lines	62
3.14 Antenna Pattern Comparison for 6-element Linear Arrays	63
3.15 Antenna Pattern Comparison for 6-element Empty Oscillator Array	65
3.16 Ideal Antenna Pattern of Second Harmonic Spatial Power Combining Array	66
3.17 3-element Second Harmonic Spatial Power Combining Array	68
3.18 4-element CPW Second Harmonic Spatial Power Combining Array	70

3.19 Antenna Pattern of 2-element E-plane Second Harmonic Array	73
3.20 Antenna Pattern of 3-element Second Harmonic Array with Short Path	74
3.21 Antenna Pattern of 3-element Second Harmonic Array with Long Path	75
3.22 Antenna Pattern of 4-element CPW Second Harmonic Array	76
4.1 Dual Polarized Array with 1 Oscillator and 4 Slots	78
4.2 Antenna Pattern of Dual Polarized Array with 1 Oscillator and 4 Slots	79, 80
4.3 2x2 Spatial Power Combining Array	82
4.4 Transmission Line Model of 2x2 Array	85
4.5 Input Impedance of Passive Part of Reduced 2x2 Array	88
4.6 Radiation Pattern of 2x2 Array	90
4.7 Configuration of 16-element Dual Polarized Array with 4 Oscillators	92
4.8 Antenna Pattern of 16-element Array	94
4.9 Variation of R for Reduced 16-element Array	96
5.1 Configuration of Reactive FET	98
5.2 Frequency Characteristics of Reflection Coefficient for Reactive FET with/without Inductive Element at Source Terminal	99
5.3 Experimental Tuning Range of Reactive FET	100
5.4 Field Distribution on 1λ Slot	101
5.5 Operation Concept of Reactive FET	102

5.6 Active Integrated Antenna with Reactive FET	103
5.7 S_{11} of Wide-band Slot Antenna	104
5.8 Antenna Patterns of Wide-band Slot Antenna	105
6.1 Photovoltaic Effect of Schottky-barrier Diode	107
6.2 Photoconductivity of Semiconductor Slab	108
6.3 Cross Section of FET's	109, 110
6.4 Energy Band Diagram at Gate of MESFET and HEMT	111
6.5 Optical Control of Reactive FET	113
6.6 Electrical and Optical Tuning Range	115, 116
6.7 Optically Controlled Active Integrated Antenna	118
6.8 Operation Spectrum Shift of Optically Controlled Active Integrated Antenna	120
6.9 Gate Voltage Dependence of Optical Tuning Range	121
6.10 Variation of R for Active Integrated Antenna	121
6.11 Antenna Pattern Comparison of Optically Controlled Active Integrated Antenna	123
6.12 2-element Uniplanar Linear Array	124
6.13 Operation Spectrum Shift of 2-element Optically Controlled Uniplanar Linear Array Using MESFET	126
6.14 Antenna Patterns of 2-element Optically Controlled Uniplanar Liner Array	127
6.15 Operation Spectrum Shift of 2-element Optically Controlled Uniplanar Linear Array Using GaAs HEMT	128

6.16 Operation Spectrum Shift of 2-element Optically Controlled Uniplanar Linear Array Using Pseudomorphic HEMT	129
6.17 Comparison of Voltage Dependent Tuning Range	130

List of Tables

Table I	Input Impedance of Passive Part at Resonant Frequency for Two Modes	50
Table II	Tuning Range Comparison of Active Integrated Antenna with Optically Controlled Reactive FET	114
Table III	Tuning Range Comparison of Optically Controlled Active Integrated Antenna	122

List of Symboles

A = vector potential

E = electric field

f_d = design frequency

G_d = device conductance

G_l = load conductance

H = magnetic field

I = general current

I_0 = initial current

J = current density

L_n = normalized slot length with respect to the second resonant slot length
($=\lambda_{sr}/\lambda$)

Q_l = loaded Q

R = general resistance

R_d = active device resistance

R_l = load resistance

S_{ij} = S -parameter (i, j = integer)

V = general voltage

V_0 = initial voltage or excitation voltage

X = general reactance

X_d = device reactance

X_l = load reactance

Y_d = device admittance

Y_l = load admittance

Z_d = device impedance

Z_{dpl} = dipole antenna input impedance

Z_l = load impedance

Z_0 = characteristic impedance of transmission line (=50 Ω)

Z_s = slot antenna input impedance

Z_t = termination impedance

Γ_{in} = reflection coefficient at input port

ϵ = general permittivity

ϵ_r = relative dielectric constant

λ = general wavelength

λ_s = slot guided wavelength

λ_{s2} = slot guided wavelength for the second harmonic

λ_c = CPW guided wavelength

λ_0 = wavelength in free-space

λ_{MoM} = wavelength used in MoM calculation

λ_{m1} = microstrip guided wavelength for the fundamental frequency

λ_{m2} = microstrip guided wavelength for the second harmonic frequency

λ_{s2} = the slot guided wavelength for the second harmonic frequency

λ_{of} = design wavelength in free-space

λ_{om} = microstrip guided wavelength at design frequency

ϕ = scalar potential

μ = general permeability

ω_0 = resonant angular frequency

Chapter I

Introduction

Over the past several years, radio engineers have discovered a need to create a new form of active circuits which consist of passive planar antenna elements and active semiconductor devices at higher frequencies. More compact and light-weight radars are required for military purposes, while simple and low-cost transceivers are essential for space and personal communication. In addition, a small and conformal radar is expected to be realized for mobile communication systems. Due to these requirements, the development of new components and a new way of implementing the components are necessary. The active antenna and quasi-optical technologies have been created to satisfy these requirements[1].

Since the active antenna is composed of direct connections of antenna elements and active devices, it is obvious that the loss is reduced in the transmission line between them. However, the significant feature of the active antenna or quasi-optical circuit is not to simply combine antennas with solid state devices, but to provide circuit characteristics resulting from antenna characteristics to form an integrated circuit antenna as a single entity[2]. Therefore, the circuit is integrated with appropriate radiation elements and solid state devices in a planar fashion so that their interactions are taken into account from the outset of the design.

In the early stage of the quasi-optical technology, the quasi-optical mixers were demonstrated[3]. This concept has been extended to quasi-optical active elements as described in this study. Combination of the quasi-optical technology and Monolithic Microwave Integrated Circuit (MMIC) technology results in a variety of active antenna and quasi-optical oscillators and power combining arrays[4].

As the active device of this single entity, the FET is frequently selected for application of MMIC technology. Several active antennas and quasi-optical oscillators have already been reported which demonstrate topology useful for the MMIC technology[5]. On the other hand, though the FET has high DC-RF conversion efficiency, an individual FET has limited capability for power generation at higher operating frequencies. Therefore, a power combining array made of a number of FET's is essential for a high power and high frequency system. Applying MMIC technology, a wafer-scale quasi-optical power combining array is promising to overcome the FET power limitation and to realize a low-cost communication system[2].

Among planar antennas coupled with an active source, a slot antenna as a radiator is extensively used in this study to demonstrate topology for the MMIC. Since a 1λ center-fed slot provides a load impedance of $50\ \Omega$ to the circuit, the slot is incorporated into a circuit made of microstrip lines[6]. If the slot is embedded in the circuit ground plane, design flexibility increases since both sides of the substrate can be effectively used[7]. As a result, the

structures for the antenna part and the circuit part are stratified. In addition, the effect on an antenna pattern measurement due to undesired radiation from the circuit discontinuity can be eliminated when the measurement is carried out in the ground plane side. The slot is electromagnetically coupled through a microstrip-to-slot line transition. Therefore, no soldering connection between the slot and the feed microstrip line is necessary. As an alternative technique, the slot can be composed of a coplanar waveguide (CPW) to create a uniplanar active integrated antenna[8]. This technique is necessary for a monolithic uniplanar active antenna array.

Therefore, the planar structure can be categorized into two forms; the uni-planar type which utilizes only one side of a substrate for simple interconnection, and the layered type which utilizes both sides of a substrate for reduction of the circuit dimension.

To date, several power combining arrays for the quasi-optical structures have been reported. A category of the quasi-optical power combining array is indicated in Fig. 1.1. There seems to be a division into two types due to their locking methods: the wave-beam type and the array type. The concept of the wave-beam type combiner[9] has been realized by a distributed grid oscillator using the Fabry-Perot resonator[10]. Meanwhile, the feature of the array type combiner is a planar or layered structure. In this type of spatial power combiner, the spacing between two adjacent radiators plays an important role for high power generation. The array type combiner is divided into two categories: the external injection locking type[11] and the

internal coupling type. The external injection locking combiner has features of wide tuning range and a possibility of beam steering. The internal coupling combiners can be further subdivided into two types; a combiner which utilizes the mutual coupling between antennas through free space or a reflection from a dielectric back plate (weak coupling)[12] and a combiner due to positively making use of RF signal generated from active sources through the direct connection with a transmission line (strong coupling)[13].

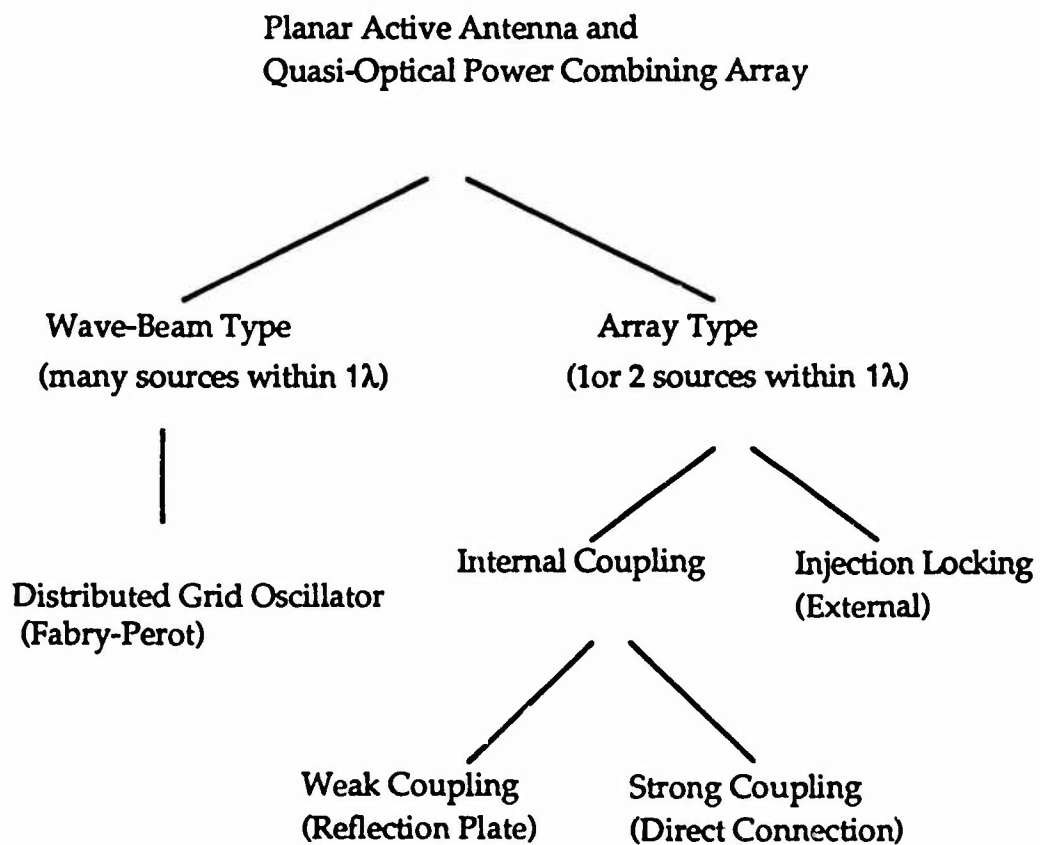


Fig. 1.1 Category of Quasi-Optical Power Combining Array

Perhaps due to possibilities of multimoding problems, the power combiner with strong coupling has not made great progress to date. Here, the strong coupling can be defined as the coupling using a direct connection by a transmission line and, further, RF energy generated from the active source is shared at the branching point. Therefore, strong RF energy is expected to transmit to adjacent active sources. From the analytical point of view, we can assume that the dominant coupling of the quasi-optical power combining array occurs through the transmission line and mutual coupling of the antennas can be neglected. Using the strong coupling technique, an external cavity for mode-locking as well as an external source for injection-locking can be eliminated since a single transmission line is used for the coupling[14].

It is well recognized that the capability of most solid state devices deteriorates as the frequency is increased. One way to alleviate this problem is to use harmonics generated by the nonlinearity of the device[15]. Since harmonics are typically much weaker than the fundamental, efficient power combining becomes even more important. For a millimeter-wave high frequency system with a monolithic quasi-optical power combining array, the array making use of the harmonic frequency generations due to the nonlinearity of the FET is promising.

However, when the packing density increases, the circuit should be as small as possible. Therefore, interconnections for controlling the devices should be minimized. To overcome these problems, optical control of

(microwave circuits has been developed[16]. The FET is found as a useful device for an optical control of microwave circuits[17] such as tuning of the active filter[18] and the HEMT oscillator tuning[19] by illuminating with a laser. If the optical control method is applied to the active integrated antennas and quasi-optical structures, design flexibility and simplification of the entire circuit may be enhanced. In addition, using this technique optical injection-locking[20] as well as optical phase shifting is feasible.

From the system point of view, it is essential that passive components are involved in the monolithic circuit. The FET can be used as a passive component in the quasi-optical power combining array. If the FET does not exhibit negative resistance, but has only a reactance component of the input impedance, this can work as a variable reactance component[21]. This is called a reactive FET in this study. Unlike a varactor diode, the advantage of this reactive FET is the separation of the output port from the control terminal. In addition, it is possible to insert the reactive FET into the microwave circuit. When the reactive FET is designed, it is important to minimize the current flow at the input port so as to operate in the stable condition to avoid oscillation. For this purpose, stability considerations are important (as in an FET amplifier[22]). Due to the optical property of the FET, the reactive FET can also be controlled by illumination[23].

The significant point to design the planar active antenna is to incorporate the antenna input impedance into the model of the entire circuit.

In the case of the active antenna using a microstrip line, the input impedance is denoted as a series impedance which depends on the frequency[24]. Meanwhile, the quasi-optical power combining array generally consists of multi-oscillators and multi-radiators which belong to a single oscillator. In order for the powers radiated from each radiator to be effectively combined, impedance matching at a branching point of multi-feed network system and the in-phase radiation signal on the radiators should be satisfied, when the array is designed[14].

In addition, consideration for a signal phase from multi-sources in the power combining array should be carried out. In the case of the array with strong coupling, the coupling line becomes an open or short stub, depending on the in-phase mode or the anti-phase mode between the adjacent oscillators. This means that the mode problem can be replaced into the stub condition problem. As a result, using the transmission line model, the modeling is involved in the circuit design[25].

In order to determine the configuration of the FET oscillator, a negative resistance value is set using small signal S-parameters. However, to evaluate the steady state oscillation frequency or other parameters under the entire circuit configuration including the slot antenna input impedance, a large signal analysis should be carried out. For this purpose, there are two methods; the harmonic balance analysis[26] and the time domain analysis. Both methods are available in the commercial-use microwave CAD. To obtain the information of the steady state oscillation, one of them is necessary.

In this study, several planar active antennas and quasi-optical planar arrays are demonstrated which use a method of strong coupling in the uniplanar and layered fashion. As a transmission line, the microstrip line and the CPW are chosen. A slot antenna as the radiating element and an FET as the active device are selected, respectively. In addition, quasi-optical arrays making use of harmonic generations from the FET oscillator are discussed. Also, the electronically and optically controlled reactive FETs and optically controlled active integrated antennas are studied. When the circuit is simulated, the input impedance of the slot radiator is included in a circuit model to investigate the characteristics of the linear and 2-dimensional planar quasi-optical power combining arrays. This emphasizes the fact that the slot antenna and circuit behave as a single entity. Although the small signal S-parameters were used to build up initial oscillation, the harmonic balance for the large signal analysis was used to investigate the steady state oscillation frequency. Finally, the feasibility of the monolithic version of the quasi-optical array is discussed.

This dissertation consists of two parts. Part 1 describes the single active antennas and the linear and 2-dimensional quasi-optical power combining arrays. Part 2 deals with the topic of variation of the quasi-optical technique. In the last chapter, conclusions and suggestions for future research are discussed.

Part 1 : Active Antennas and Power Combining Arrays

Chapter II Planar Active Antenna

2.1 Oscillator Design

2.1.1 1-port Oscillator

Generally, there are two categories of solid state oscillators; a feedback type and a negative resistance type. In the former, when the loop gain of the feedback equals one, the net gain of the feedback oscillator becomes infinite. Hence, the circuit operates in steady state oscillation. The negative resistance approach, however, is generally applied to a one-port negative resistance oscillator as shown in Fig. 2.1. For the steady state oscillation, the voltage around the loop must be zero[22]. Using the parameters shown in Fig. 2.1,

$$-R_d(I, \omega) + jX_d(I, \omega) + R_l(\omega) + jX_l(\omega) = 0 \quad (2.1)$$

$$R_d(I, \omega) = R_l(\omega) \quad (2.2)$$

$$X_d(I, \omega) = -X_l(\omega) \quad (2.3)$$

In this case, R_d and X_d have amplitude and frequency dependence. By using the reflection coefficient, the steady state oscillation condition is also expressed

$$\Gamma_l \cdot \Gamma_d = \frac{R_l + jX_l - Z_0}{R_l + jX_l + Z_0} \cdot \frac{-R_l + jX_l - Z_0}{-R_l + jX_l + Z_0}$$

$$= \frac{R_l + jX_l - Z_0}{R_l + jX_l + Z_0} \cdot \frac{-(R_l + jX_l + Z_l)}{-(R_l + jX_l - Z_l)} = 1 \quad (2.4)$$

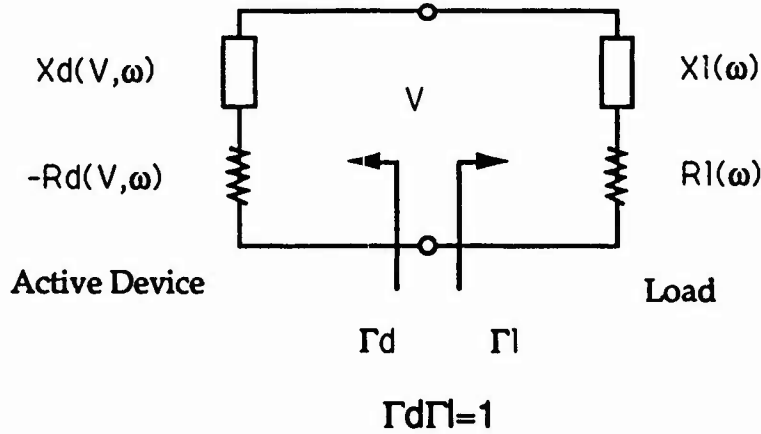


Fig. 2.1 1-port Negative Resistance Oscillator

Generally, $R_d(I, \omega)$ decreases when the amplitude I increases. Therefore, in order for the circuit to oscillate, R_l is required to be less than the initial $R_d(I_0, \omega_0)$ (as shown in Fig. 2.2). This means that the circuit is unstable, since the total resistance of the circuit is negative ($-R_d(I, \omega) + R_l(\omega) < 0$). On the other hand, in the case of the circuit denoted by parallel elements as shown in Fig. 2.3, $G_d(V, \omega)$ decreases as V increases.

Although we can obtain the steady state oscillation through the technique described above, this may not be necessary for a stable operation condition. For this stable operation, a device and load-line locus curve as shown in Fig. 2.4 is generally used[27]. According to Kurokawa[28], there are

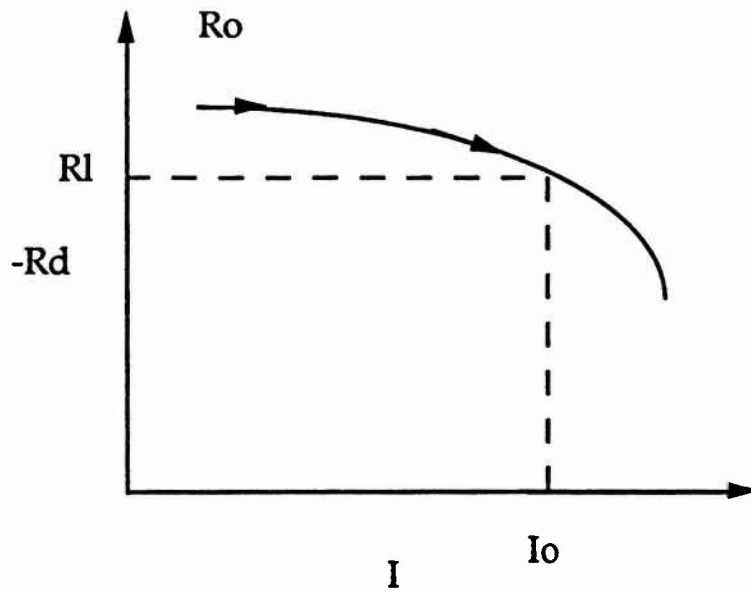


Fig. 2.2 Negative Resistance Variation of Active Device in Series Circuit Model

two stable points out of three steady state oscillation points in this case. This is because the angle ϕ , measured clockwise from $Z_d(A, \omega)$ to $Z_l(\omega)$ is required to be greater than 0° and less than 180° for a stable operating point at the intersection point. For low noise, the best angle is 90° . This stable oscillation condition is analytically denoted by Kurokawa

$$\frac{dR_d}{dA} \cdot \frac{dX_l}{d\omega} + \frac{dX_d}{dA} \cdot \frac{dR_l}{d\omega} < 0 \quad (2.5)$$

where partial derivatives are evaluated at A_0 and ω_0 .

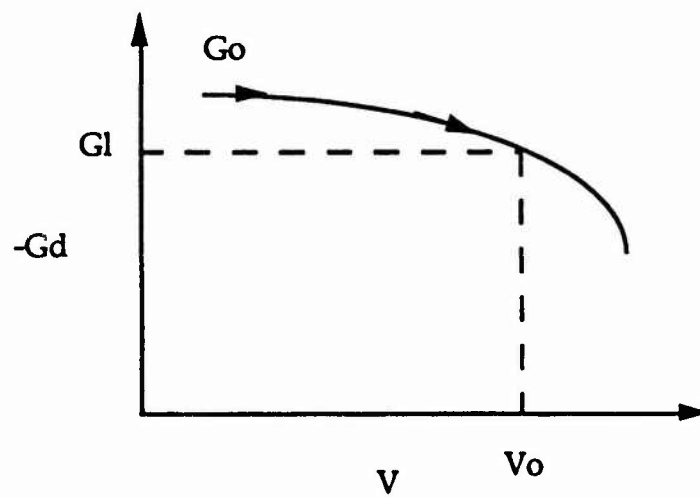
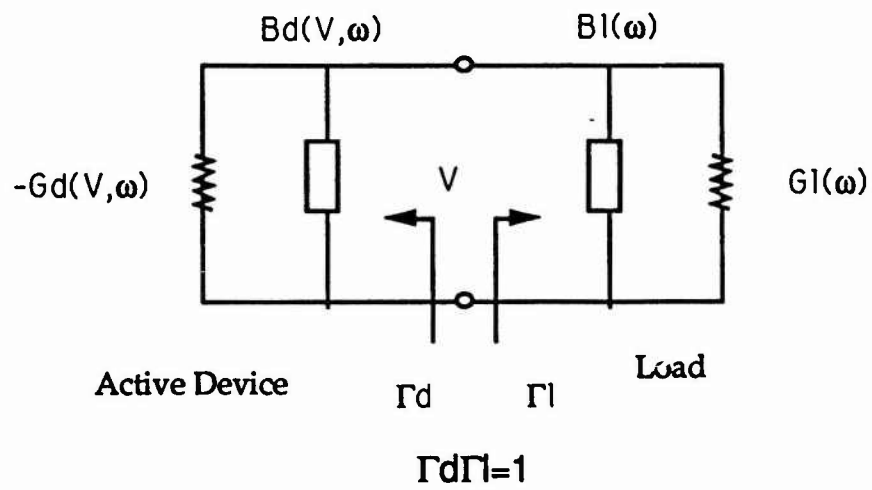


Fig. 2.3 Parallel Circuit Model of Active Device and Negative Conductance Variation

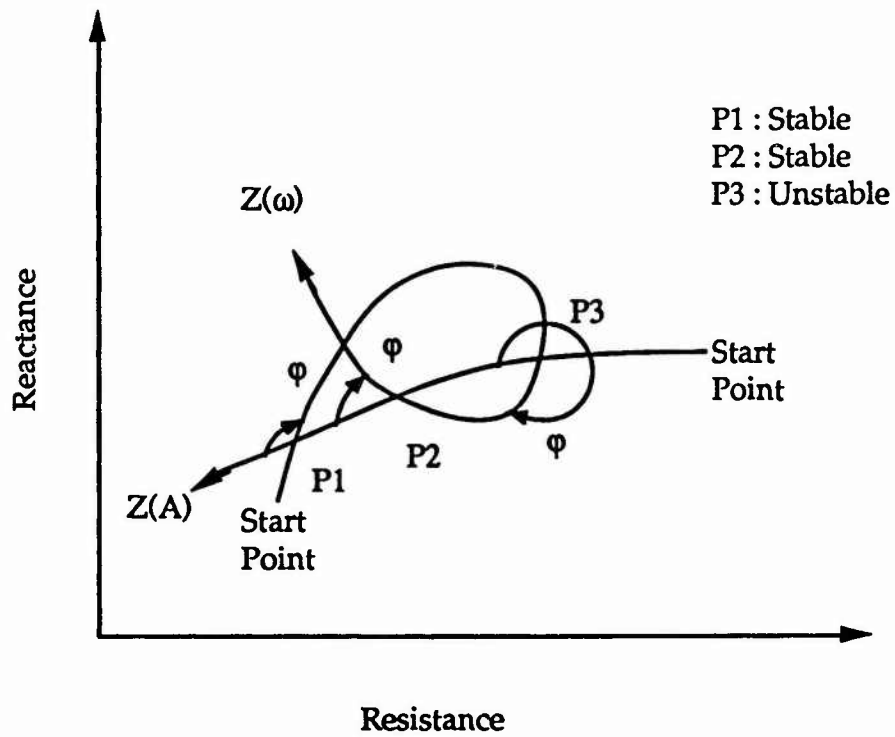


Fig. 2.4 Device and Load Line Locus

Using the series circuit model shown in Fig. 2.1, a frequency tuning range can be understood as the following. The change of the reactance is obtained by deviating X with respect to ω .

$$jX = j\omega L + \frac{1}{j\omega C} \quad (2.6)$$

$$\frac{dX}{d\omega} = L - \frac{1}{\omega^2 C} \quad (2.7)$$

where $X_d = 1/\omega C$ and $X_l = \omega L$. Using $\omega_0 = 1/\sqrt{LC}$ and $Q_l = \omega_0 L/R$,

$$\frac{dX}{d\omega} = \frac{2RQ_1}{\omega_0} \quad (2.8)$$

where $R=R_d + R_l$

From (2.8), the frequency deviation around resonance is directly related to the reactance deviation as

$$\Delta f = \frac{f_0}{2RQ_1} \Delta X \quad (2.9)$$

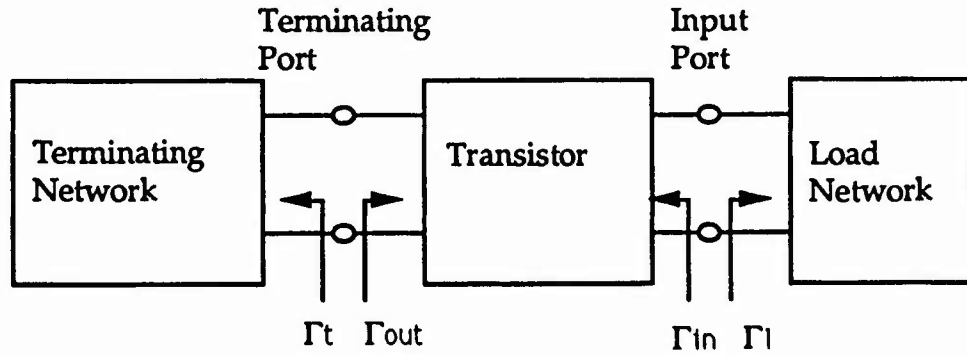
For the solid-state device, ΔX can be tuned by applied DC voltages. Therefore, from (2.9), the circuit must have a large ΔX or a low Q_1 to have the wide tuning range. Generally speaking, Q_1 is low for planar circuit using a low dielectric constant substrate. Hence, we can expect a wide tuning range when such a substrate is used.

2.1.2 2-port Negative Resistance Oscillator

A two-port network oscillator is shown in Fig. 2.5. It is possible to obtain the negative resistance oscillator using a two-port device such as an FET. If the terminating port is connected by an appropriate impedance and the two-port circuit is potentially unstable, the steady state oscillation condition, $\Gamma_1\Gamma_d=1$, described in the previous section can be applied. When the

input port is oscillating, the terminating port is also oscillating. Namely, at the input port, we have

$$\Gamma_{in} \times \Gamma_l = 1 \quad (2.10)$$



$$\Gamma \Gamma_{in} = 1, \quad \Gamma \Gamma_{out} = 1$$

Fig. 2.5 Two-port Oscillator

for the steady state oscillation. For the two-port network with the termination Z_t

$$\Gamma_{in} = S_{11} + \frac{S_{12}S_{21}\Gamma_t}{1 - S_{22}\Gamma_t} \quad (2.11)$$

$$\text{where } \Gamma_t = \frac{Z_t - Z_0}{Z_t + Z_0}$$

From (2.10),

$$\Gamma_1 = \frac{1}{\Gamma_{in}} = \frac{1 - S_{22}\Gamma_t}{S_{11} - \Delta\Gamma_t} \quad (2.12)$$

$$\text{where } \Delta = S_{11}S_{22} - S_{12}S_{21}$$

From (2.12),

$$\Gamma_t = \frac{1 - S_{11}\Gamma_1}{S_{22} - \Delta\Gamma_1} \quad (2.13)$$

Meanwhile,

$$\Gamma_{out} = \frac{S_{22} - \Delta\Gamma_1}{1 - S_{11}\Gamma_1} \quad (2.14)$$

Therefore, from (2.13) and (2.14),

$$\Gamma_t \times \Gamma_{out} = 1 \quad (2.15)$$

As described in the previous section, since R_d degrades from the initial value, the initial value should be designed to be larger than the steady state value which equals to the load resistance R_l . Using the small signal S-parameters

and the linear amplitude dependence of the negative conductance, the approximate relationship of

$$R_d(I_o, \omega_o) = 3R_l(\omega_o) \quad (2.16)$$

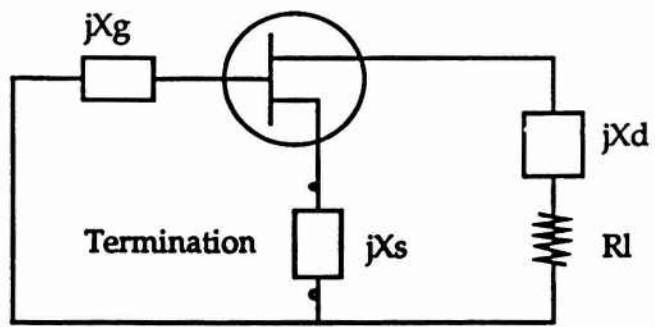
is usually used under the assumption of a large unloaded Q ($=\omega_o C/G(V_o, \omega_o)$). (2.16) is successfully used when R_l is constant. However, when R_l is not constant R_d can be given with a smaller value than $3R_l$ [29]. Of course, how small R_d is depends on the frequency characteristic of the negative resistance FET oscillator as well as the variation of the load. In the case of the active antenna with a 1λ slot, the empirical relation

$$R_d = a \times R_l \quad (a=1\sim 1.2) \quad (2.17)$$

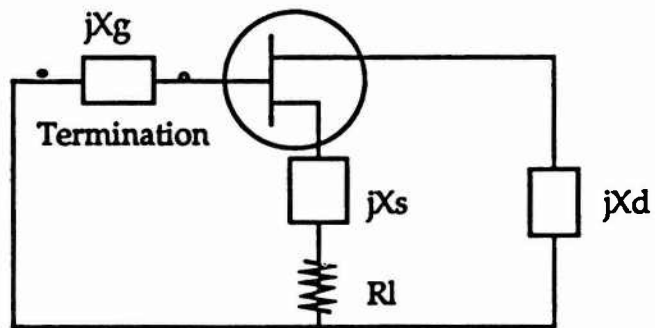
is used in this study to convey the maximum power to the slot as a load.

2.1.3 FET Oscillator

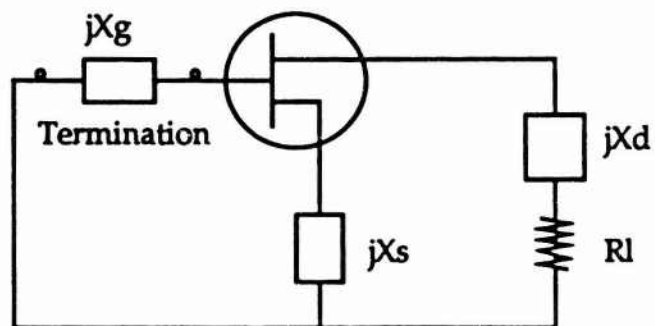
There are three types of negative resistance FET oscillators as shown in Fig. 2.6; a common-gate type, a common-drain type and a common-source type. The common-gate type and the common-source type generally require a reactance element at the common terminal to enhance instability. The common-drain type is used in a reverse channel configuration with the positive voltage applied to the source terminal. The most convenient



(a) Common-gate Type



(b) Common-drain Type



(c) Common-source Type

Fig. 2.6 Negative Resistance FET Oscillator

configuration is the common-source type because a commercially available data catalog that lists S-parameters can be used.

So far, when we design the oscillator, the small signal parameters was used to determine the circuit configuration. However, we can check the steady state stable oscillation frequency by using the large signal parameters. If this large signal frequency does not meet the desired frequency, we may design the oscillator again, using the small signal parameters. For the large signal analysis, there are mainly two methods[26]; the harmonic balance analysis such as Libra and the time domain analysis such as Microwave SPICE. In this study, the former was used. Fig. 2.7 shows a circuit model for

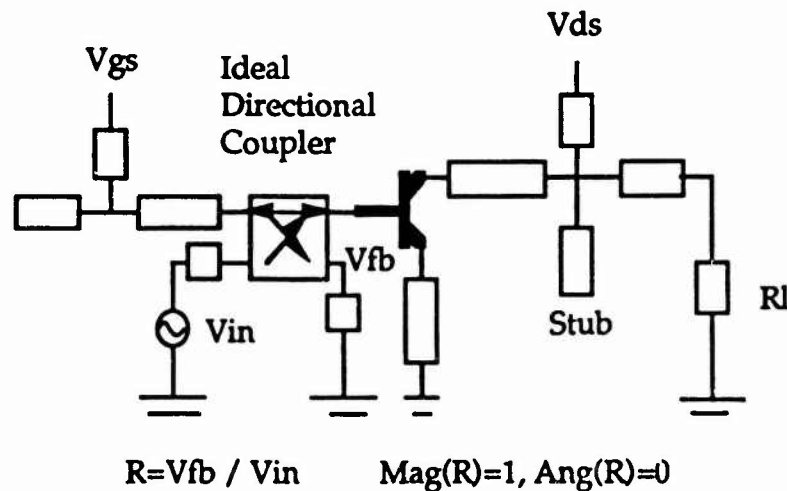


Fig. 2.7 Circuit Model with R_l for Large Signal Analysis

use with the large signal analysis[30]. The steady state oscillation was verified by confirming the equation of (2.15). This relationship can be

obtained from the input-to-output ratio of an ideal directional coupler which has no insertion loss. Namely, the ratio $R = V_{fb}/V_{in}$ at the gate terminal point is equal to $\Gamma_t \Gamma_{out}$

$$R = \frac{V_{fb}}{V_{in}} = \frac{V_{fb}}{V_t} \cdot \frac{V_t}{V_{in}} = \Gamma_t \Gamma_{out} \quad (2.18)$$

This R is usually a complex value. Therefore, $R=1$ (magnitude of $R = 1$ and argument of $R = 0$) was used to investigate the steady state oscillation. By observing the frequency characteristic of R , the steady state oscillation frequency can be evaluated.

2.2 Slot Radiator

2.2.1 Modified Booker's Formula

Since we chose a slot antenna as a radiator, let us consider the input impedance of the slot suitable for the design of the active antenna. In the case of a slot antenna, we may find the ratio of a voltage resulting from the field on the slot to a current source. On the other hand, the input impedance of a complementary dipole antenna is determined as the ratio of an input source voltage to a current at the feed point. In a homogeneous space, since these two input impedances are complementary, we can use Booker's formula to relate the input impedance of the slot antenna to that of the complementary dipole antenna. However, in the case of the printed antenna on a dielectric

substrate, we must use Booker's formula with a mean dielectric constant, which is approximately valid since the space is not homogeneous[31].

$$Z_s \bullet Z_{dpl} = \frac{\eta_m^2}{4} \quad (2.19)$$

$$\text{where } \eta_m = \sqrt{(\mu / \epsilon_m)}$$

$$\epsilon_m = (\epsilon_{air} + \epsilon_{diel}) / 2 \quad (2.20)$$

Using this formula, we can convert the problem of the input impedance of the slot antenna into that of the dipole antenna.

2.2.2 Dipole Antenna

For the analysis of the dipole antenna, we can use the two types of integral equations; the Pocklington type and the Hallen type[32]. As an equation for a thin wire antenna, the Pocklington integral equation can be derived from Maxwell's equations. From the definition of the vector potential, A,

$$H = \nabla \times A \quad (2.21)$$

Using this potential,

$$\nabla \times E = -j\omega\mu H = -j\omega\mu (\nabla \times A) \quad (2.22)$$

$$\nabla \times (E + j\omega\mu A) = 0 \quad (2.23)$$

(

Therefore,

$$\mathbf{E} + j\omega\mu\mathbf{A} = -\nabla\phi \quad (2.24)$$

where ϕ is a scalar potential

From (2.21) and (2.24),

$$\begin{aligned} \nabla \times \mathbf{H} &= \mathbf{J} + j\omega\epsilon\mathbf{E} \\ \nabla \times (\nabla \times \mathbf{A}) &= \mathbf{J} + j\omega\epsilon(-j\omega\mu\mathbf{A} - \nabla\phi) \\ (\nabla^2 + k^2)\mathbf{A} &= -\mathbf{J} + \nabla(\nabla\mathbf{A}) + \nabla(j\omega\epsilon\phi) \end{aligned} \quad (2.25)$$

(

Using the Lorentz Gauge

$$\nabla \cdot \mathbf{A} + j\omega\epsilon\phi = 0 \quad (2.26)$$

(2.25) becomes

$$(\nabla^2 + k^2)\mathbf{A} = -\mathbf{J} \quad (2.27)$$

From the Stratton-Chu solution,

$$\mathbf{A} = \int \mathbf{J} \frac{e^{-jkr}}{4\pi r} dV' \quad (2.28)$$

Combining (2.26) and (2.28) with (2.24), the scattered field is

$$\mathbf{E}_{\text{scat}} = -j\omega\mu\mathbf{A} + \frac{\nabla(\nabla' \cdot \mathbf{A})}{j\omega\epsilon}$$

$$j\omega\epsilon\mathbf{E}_{\text{scat}} = (k^2 + \nabla\nabla') \int \mathbf{J} \frac{e^{-jkr}}{4\pi r} dV' \quad (2.29)$$

On the metal surface,

$$\mathbf{E}_{\text{tot}} \times \mathbf{n} = [\mathbf{E}_{\text{scat}} + \mathbf{E}_{\text{in}}] \times \mathbf{n} = 0 \quad (2.30)$$

Therefore,

$$-j\omega\epsilon\mathbf{E}_{\text{in}} = (k^2 + \nabla\nabla') \int \mathbf{J} \frac{e^{-jkr}}{4\pi r} dV' \quad (2.31)$$

Due to the thin wire approximation, \mathbf{J} has the z -component only. Hence, (2.31) becomes

$$-j\omega\epsilon E_{\text{zin}} = \left(k^2 + \frac{d^2}{dz^2}\right) \int J_z(z') \frac{e^{-jkr}}{4\pi r} dz' \quad (2.32)$$

This equation is called the Pocklington type integral equation.

Further, this equation can be solved as follows. From (2.32) and $E_{zin}=V_0 \cdot \delta(z)$ (a voltage source at origin),

$$-j\omega\epsilon V_0 \cdot \delta(z) = (k^2 + \frac{d^2}{dz^2}) \int J_z(z') \frac{e^{-jkr}}{4\pi r} dz' \quad (2.33)$$

A solution of (2.33) is

$$\int J_z(z') \frac{e^{-jkr}}{4\pi r} dz' = K_1 \cos kz + j K_2 \sin k |z| \quad (2.34)$$

Let us integrate (2.34) between the gap for the voltage source, then make it infinitesimally small. Finally, we obtain

$$K_2 = -V_0 / 2\eta_0$$

where $\eta = \sqrt{\mu / \epsilon_0}$

Eventually,

$$\int J_z(z') \frac{e^{-jkr}}{4\pi r} dz' = K_1 \cos kz - \frac{jV_0}{2\eta_0} \sin k |z| \quad (2.35)$$

This is called the Hallen type integral equation. Here, K_1 is determined by the boundary condition.

These integral equations are solved numerically by the Method of Moment (MoM)[33]. This MoM is a technique to translate the integral equation into the matrix equation for the computational calculation. To solve the original equation, a weight function to minimize the residual error and an expansion function to expand the unknown function using known functions should be introduced. Due to use of special functions for the expansion function, there are two techniques for MoM; the entire domain method and the subdomain method. In this study, the point matching method was used in which the subdomain expansion function is the pulse function and the weight function is the δ -function. A detailed explanation appears in Reference [32] and [34]. In the calculation, 0.25 of the slot width is used as the equivalent radius of the dipole. From these two types of integral equation, the Pocklington type integral equation is generally used[32]. However, when the slot width increases, the agreement between the experimental resonant slot length and the theoretical one deteriorates. For instance, the theoretical second resonant slot length, L_{sr} , becomes $0.68\lambda_{MoM}$ from the Pocklington type integral equation, while the experimental resonant slot length, L_{ex} , is almost $1\lambda_s$, when the slot width is $0.081\lambda_s$. Therefore, we used the modified input impedance from the Pocklington type integral equation.

2.2.3 Slot Radiator in Planar Active Antenna

Through the calculation of the input impedance of the dipole described above and in (2.19), the slot input impedance can be found. This input impedance has a real part and an imaginary part which depend on the

frequency. The antenna is designed under the resonant condition so that its reactive part is equal to zero. In this case, the design frequency of the active antenna should be identical with the resonant frequency of the antenna. As described in the previous section, the agreement between the experimental resonant slot length and the theoretical one is not good due to experimental conditions. This means that the antenna input impedance should be modified for our simulation. Here, let us assume for the circuit analysis that the two resonant slot lengths (L_{sr} from the Pocklington type integral equation and L_{ex}) are identical and the theoretical calculation can explain the experimental status around the second resonant slot length[25]. Under this assumption, the theoretical resonant frequency can be identified with the design frequency of the circuit. In this case, the wavelength at the second resonant frequency was used as the wavelength at the design frequency. As a result, since the antenna input impedance of the active antenna is incorporated into the entire circuit as a single entity, circuit parameters of the passive part of the active antenna can be simulated, including the antenna characteristics. The dependence of the input resistance and reactance of the slot antenna on the normalized wavelength are shown in Fig. 2.8. Applying curve fitting in a range of 0.7 to 1.3 of the normalized slot length, we obtained the following relationship,

$$Z_s = R + jX \quad (2.36)$$

$$R = 10^4 \cdot (0.226L_n^4 - 1.027L_n^3 + 1.757L_n^2 - 1.351L_n + 0.401) \quad (2.37)$$

$$X = 10^2 \cdot (-0.982L_n^2 + 3.679L_n - 2.706) \quad (2.38)$$

where $L_n (= \lambda_{sr}/\lambda)$ is the normalized slot length with respect to the second resonant slot length. In both expressions, the correlation coefficients are 1.0 within this range.

The next consideration is how this impedance is incorporated into the active antenna circuit. Generally speaking, an aperture in a transmission line creates scattered waves due to the discontinuity. In a waveguide, a longitudinal slot in a broad wall is equivalent to a shunt impedance on a transmission line, while a transverse slot is described as a series impedance[35]. Similarly, in the case of a microstrip line, a crossing slot in the ground plane is represented as a series impedance as shown in Fig. 2.9[24].

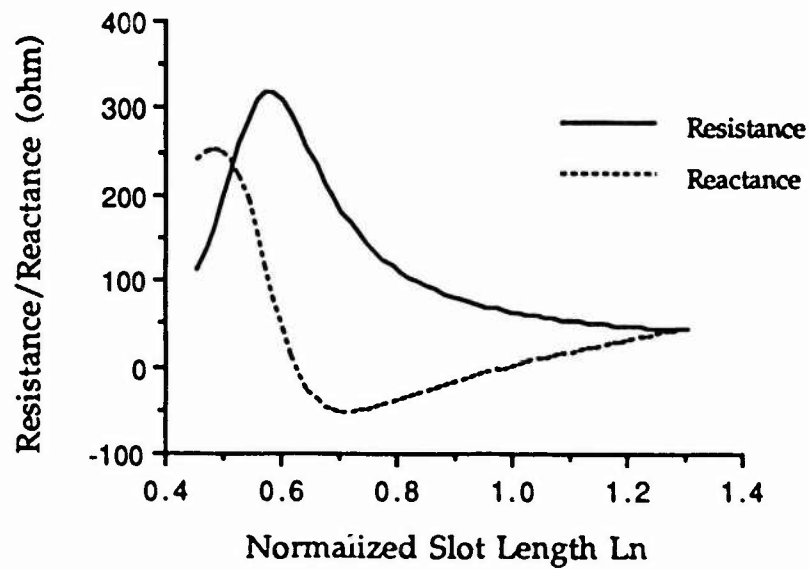


Fig. 2.8 Input Impedance of Slot Antenna with Normalized Wavelength

Therefore, this series impedance is replaced by the input impedance of the slot antenna as calculated above in our circuit case. Using this argument, the slot is expressed as one of the lumped circuit elements in the circuit model.

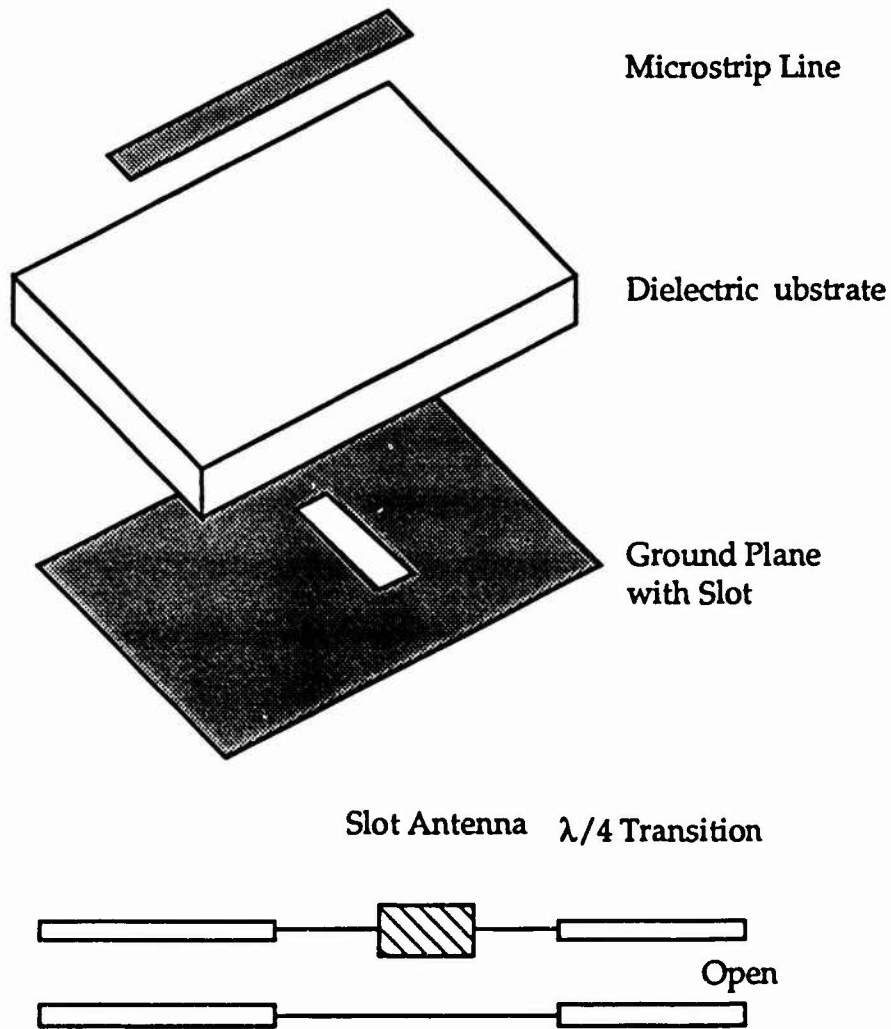


Fig. 2.9 Crossing Slot in Ground Plane of Microstrip Line Circuit

2.3 Measured Characteristics

2.3.1 Isotropic Conversion Gain and ERP

In order to appreciate the quasi-optical circuit performance, conventional measures of performance for oscillators cannot be applied, since there is no well-defined RF output port. Since the isotropic gain for the antenna is defined, an alternative definition of isotropic DC-RF conversion gain, G_{iso}^T , is used for a quasi-optical oscillator as a figure of merit[36]. This setup is shown in Fig. 2.10. This quantity is determined by measuring the received power from quasi-optical oscillator at a given bias condition and then comparing the result with the received power due to a standard gain horn driven with an RF power equal to the DC bias power. Namely, the isotropic conversion gain is a measure of how well the circuit converts the input DC power and delivers it to a receiver. From G_{iso}^T , we can define the Effective Radiated Power (ERP) as the product of G_{iso}^T and the DC power.

$$ERP = G_{iso}^T \times P_{DC}$$

2.3.2 Antenna Pattern and Tuning Range

Due to the ERP, the radiated power distribution of the circuit can be appreciated. In addition, by measuring an antenna pattern, information concerning the field distribution on the slot, the amplitude and the phase of the array can be obtained. Therefore, the antenna pattern is a very important measurement factor.

From the view-point of applications, such as wide-band communication and a radar hopping technique, it is also important to know how wide the oscillation frequency can be changed. This is commonly referred to as the tuning range. By changing bias voltages or illuminating with optical sources, the tuning range was measured.

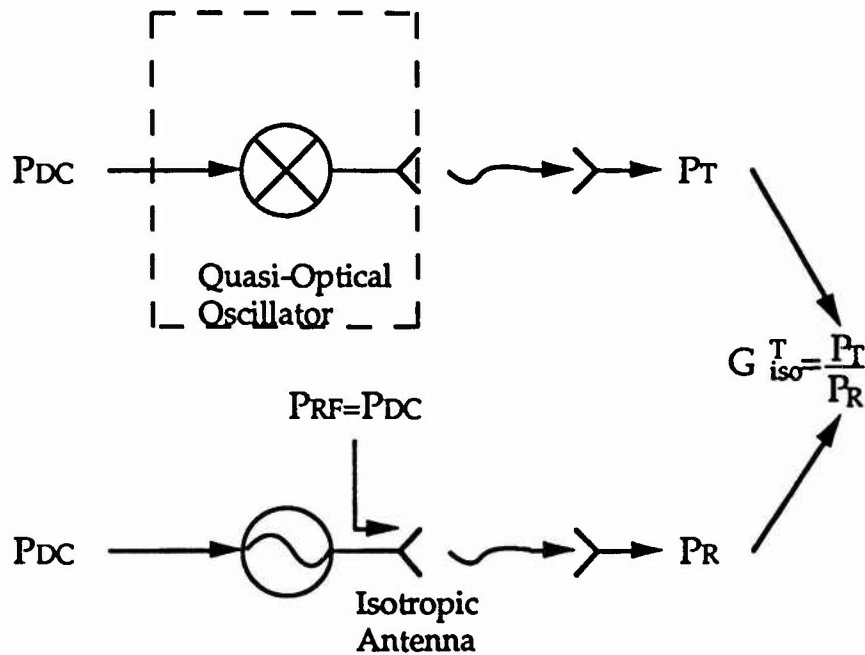


Fig. 2.10 Definition of Isotropic Conversion Gain

2.4 Layered and Uniplanar Active Antenna

2.4.1 Design of Layered Active Antenna

The simplest way to realize the single active antenna is to design the oscillator circuit with one or more radiation elements. A single oscillator with

a single radiator is considered as the unit cell of a quasi-optical power combining array. Fig. 2.11 shows a configuration of the single active antenna with a slot radiator in the ground plane.

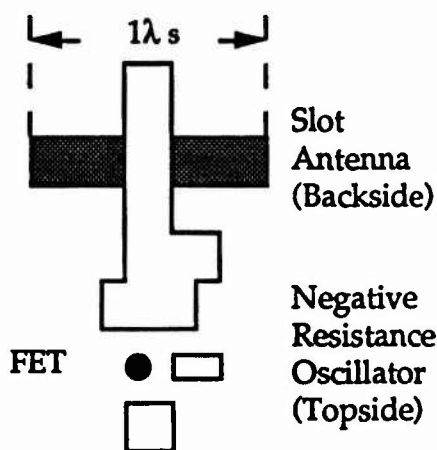


Fig. 2.11 Configuration of Single Active Antenna

The design was carried out as follows. After the target (expected) frequency is decided, we can design the negative resistance oscillator with the input impedance of -50Ω at the buildup frequency (the initial oscillation frequency) using the small signal S-parameters. When the small signal S-parameters are used, we must take a "margin" due to the change of the negative resistance in the steady state oscillation as described in Fig. 2.2. The buildup frequency is usually 5 to 10 % higher than the target frequency. At this time, the geometrical length and width of the 1λ slot antenna are also decided.

Once the circuit configuration is determined, the steady state oscillation frequency of the entire circuit configuration including the slot antenna input impedance is checked using large signal analysis. In this study, the commercially available CAD (Libra by EEsof) was used, which is based on the harmonic balance analysis. Fig. 2.12 shows a circuit model used for the large signal analysis of the active antenna shown in Fig. 2.11. Since the input impedance of the slot depends on frequency, the $50\ \Omega$ load shown in Fig. 2.7 is replaced by the frequency-dependent load. To obtain the steady state oscillation frequency, we may investigate the ratio $R=V_{fb}/V_{in}$ at the gate terminal point as described in 2.1.3. The simulation result is indicated in Fig. 2.13. According to this result, the steady state oscillation frequency is 24.3 GHz for the active antenna circuit designed at 25 GHz.

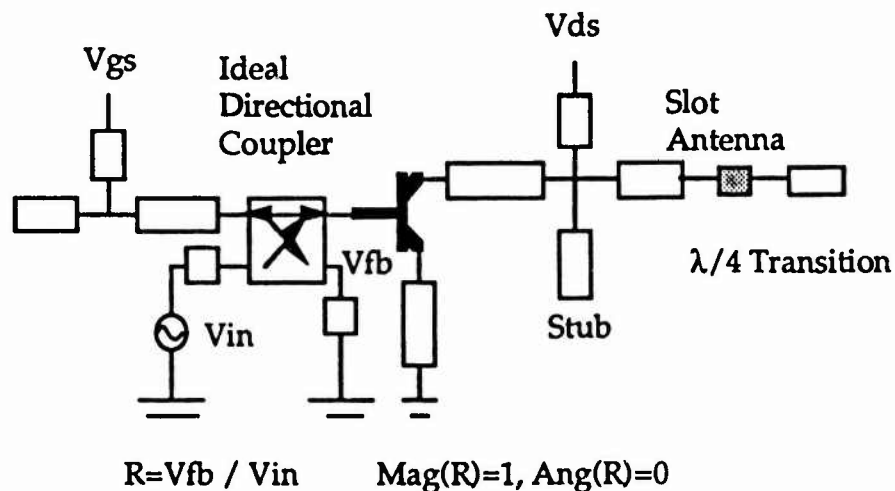


Fig. 2.12 Large Signal Model for Single Active Antenna

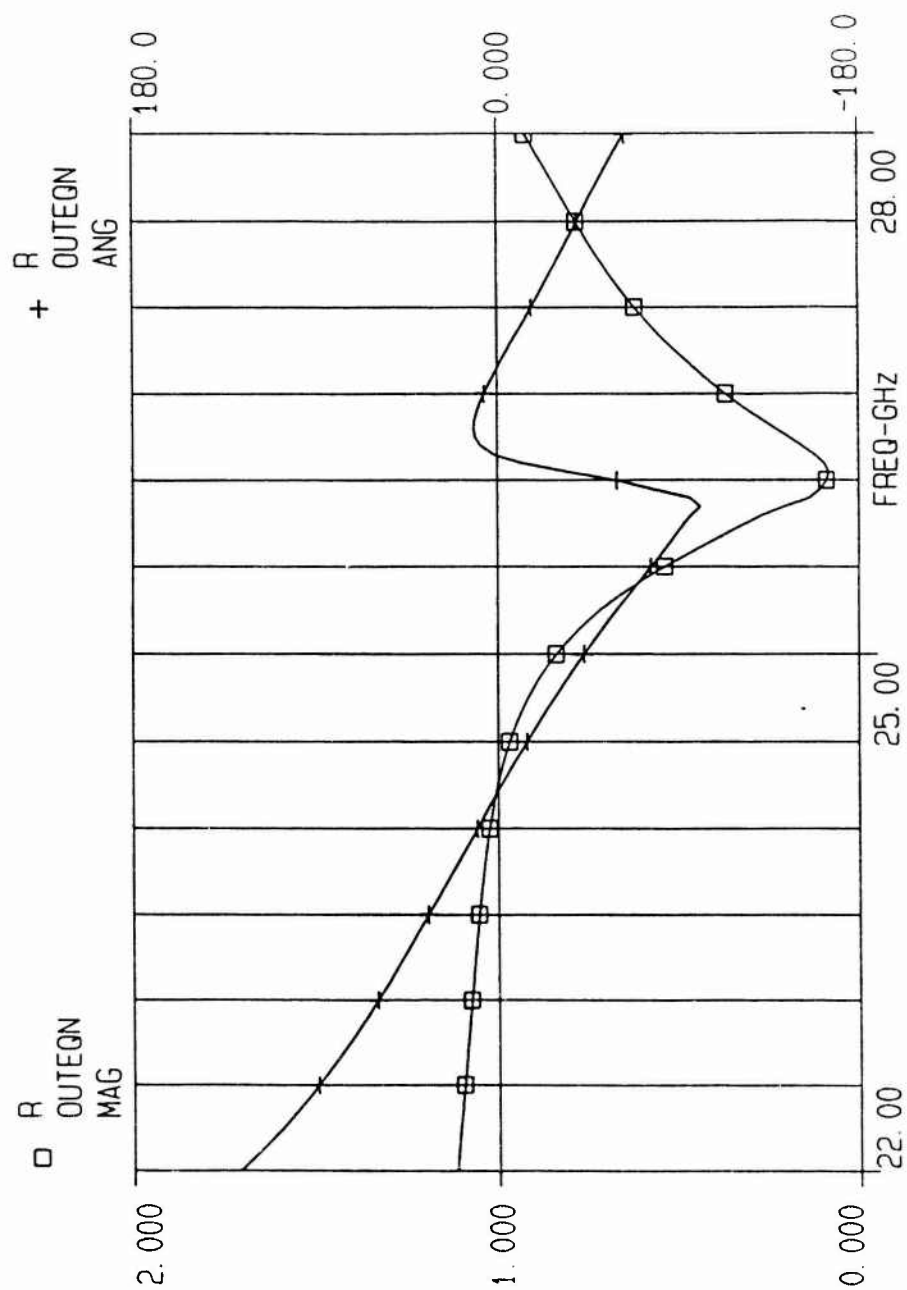


Fig. 2.13 Variation of $R=V_{fb}/V_{in}$ of Single Active Antenna

The slot length is $1\lambda_s$ and the slot width is $0.081\lambda_s$. This slot dimension will be used in all circuits using microstrip lines in this study. In order to construct the layered structure, a $\lambda/4$ microstrip open-end circuit with a characteristic impedance, Z_0 , of $50\ \Omega$ is adopted as a microstrip-to-slot line transition. Through this transition, the slot antenna, which is electromagnetically coupled with the microstrip line provides an appropriate load to the active device. By altering the length of this open-end circuit, the oscillation frequency can be tuned. In this case, the open-end circuit works as a tuning stub which cancels the reactance of both the antenna input impedance and the drain output impedance of the FET.

2.4.2 CPW Active Antenna Configuration

As a unit cell of the uni-planar quasi-optical power combining array, an active antenna using a negative resistance FET oscillator and a CPW-fed slot was also designed[8],[37]. A circuit configuration of a single uniplanar active antenna is shown in Fig. 2.14. The oscillator was simulated at 10 GHz using CPW and small signal S-parameters, as described in the previous section for the layered active antenna. A CPW cross junction was used for a matching stub. The matching stub, the gate termination and the feed line to the slot are short-circuited CPW lines with a DC cut. Air bridges are provided to suppress unwanted modes in a CPW circuit.

In order to investigate the effect of the tuning stub to operating frequencies, a CPW active antenna with a CPW-slot cross junction at the top

appropriate reactance with the active antenna, an oscillation frequency is tuned by adjusting the length of the tuning stub. Other parts of the circuit are the same as those of Fig. 2.14.

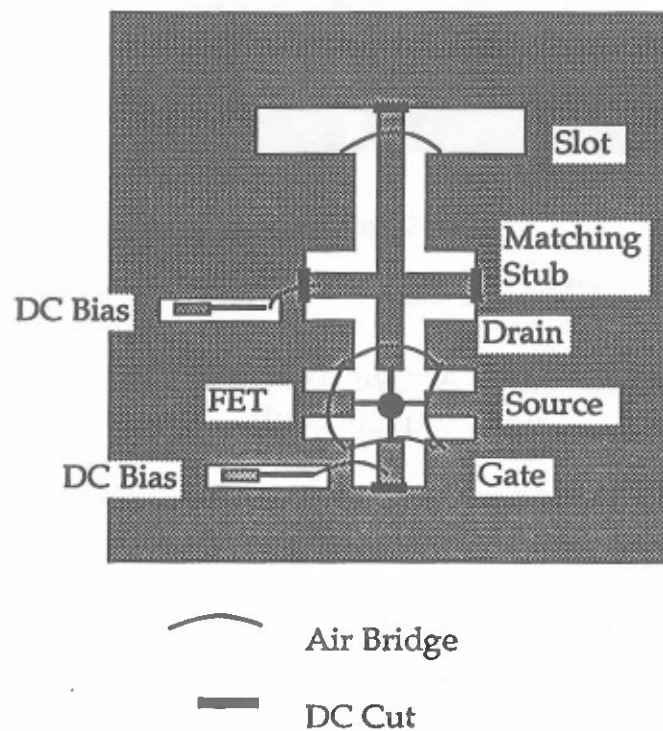


Fig. 2.14 Configuration of Single Uniplanar Active Antenna

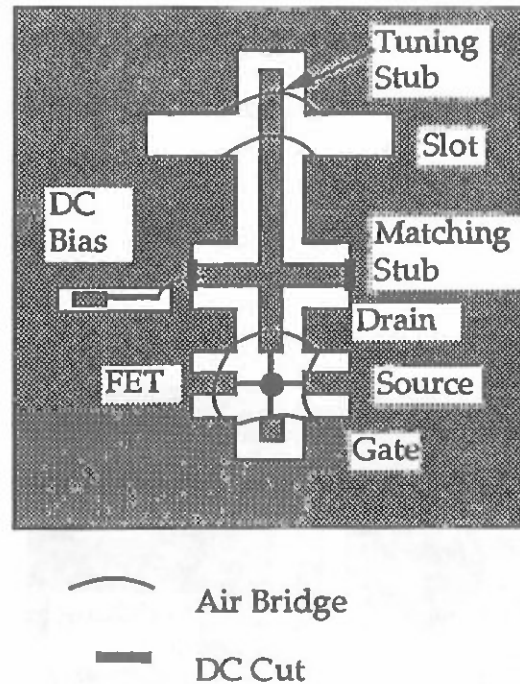


Fig. 2.15 CPW Active Antenna with Tuning Stub

2.4.3 Experimental Results

In each circuit, package type FET's were used as active sources. In the case of the circuits using microstrip lines, the DC bias voltage is supplied to the FET through a thin wire. High impedance microstrip lines with a quarter wavelength radial stub and a bonding pad were used as bias lines for the FET drain and gate. A 0.79 mm (31 mil) thick PTFE dielectric substrate (Rogers Duroid 5870 ; $\epsilon_r=2.33$, 1 oz Cu sheet) was used. Two active antennas using microstrip lines were fabricated which were designed to operate at frequencies of 10 GHz and 25 GHz[7],[38]. The FET's used were ATF 26884 by Avantek for the 10 GHz circuit and NE 32484A by NEC for the 25 GHz

circuit. Oscillation frequencies of 9.3 GHz with $V_{ds}=3.5$ V and $V_{gs}=-0.7$ V, and 24.0 GHz with $V_{ds}=3.3$ V and $V_{gs}=-0.5$ V, and the ERPs of 13.2 dBm and 13.7 dBm were obtained, respectively. Also, the tuning ranges due to the change of DC voltages were 170 MHz and 100 MHz, respectively. Antenna patterns measured for these circuits are shown in Fig. 2.16. In addition, a theoretical antenna pattern which was calculated using MoM and the Pocklington type integral equation is shown in Fig. 2.16. Agreement with these three antenna patterns is very good.

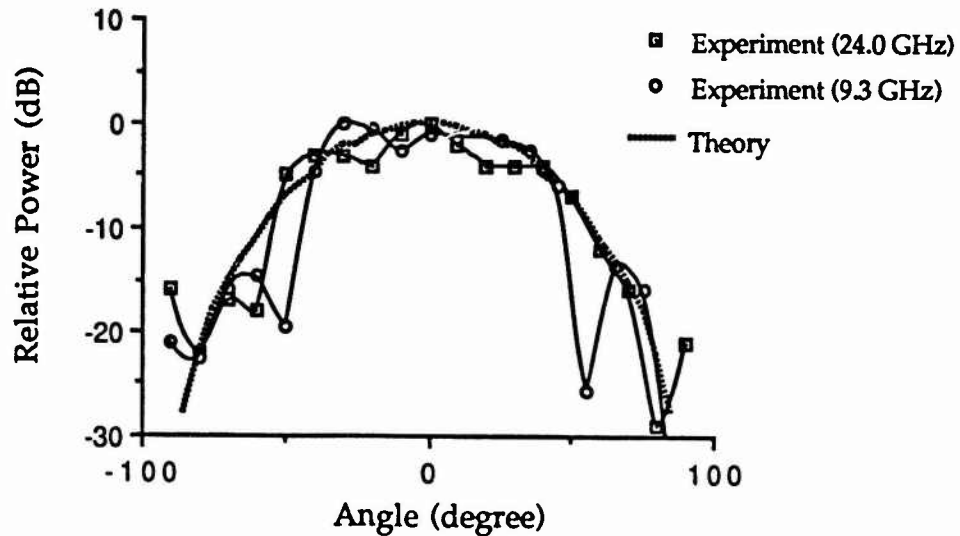


Fig. 2.16 Antenna Pattern Comparison of Microstrip Active Antenna

(For the CPW active antenna, the FET used here is the package-type Avantek ATF13284. Although the circuit was made by hybrid MIC technology, to demonstrate a topology useful for uniplanar monolithic integrated circuits, a high dielectric constant substrate was used (Rogers Duroid 6010 ; $\epsilon_r=10.5$, thickness=25 mil, 1 oz Cu sheet). The DC bias was supplied for only V_{ds} through a bonding pad connected to a high impedance CPW which is then connected with the CPW feed line through an air bridge. In this case, there is no bias line at the gate, i.e., the floating gate. The slot length of $0.75\lambda_g$ and the slot width of $0.05\lambda_g$ were determined for the CPW-fed slot through a preliminary experiment. The single uni-planar active antenna oscillated at 8.6 GHz with $V_{ds}=4.1$ V and $V_{gs}=-0.5$ V. The tuning range of this circuit was 25 MHz. The oscillation was very stable due to the high dielectric substrate. A difference between the oscillation frequency and the design frequency has resulted from the discontinuity created at the CPW crossing of the matching stub and the long inductive bias gold wire.

Next example is the CPW active antenna with the CPW-slot cross junction. Fig. 2.17 shows the variation of the oscillation frequencies with $V_{ds}=4.0$ V (constant) with respect to a normalized length. This normalized length is defined the ratio of physical length to wavelength at the design frequency of 8 GHz. The adjustment of the length of the tuning stub was carried out by cutting the stub with a knife. As expected, the oscillation frequency increased as the length of the tuning stub decreased. Further, the tuning range at each stub length was measured. An increase of the tuning

range due to the reduction of the stub length means a lower Q status as described in 2.1.1.

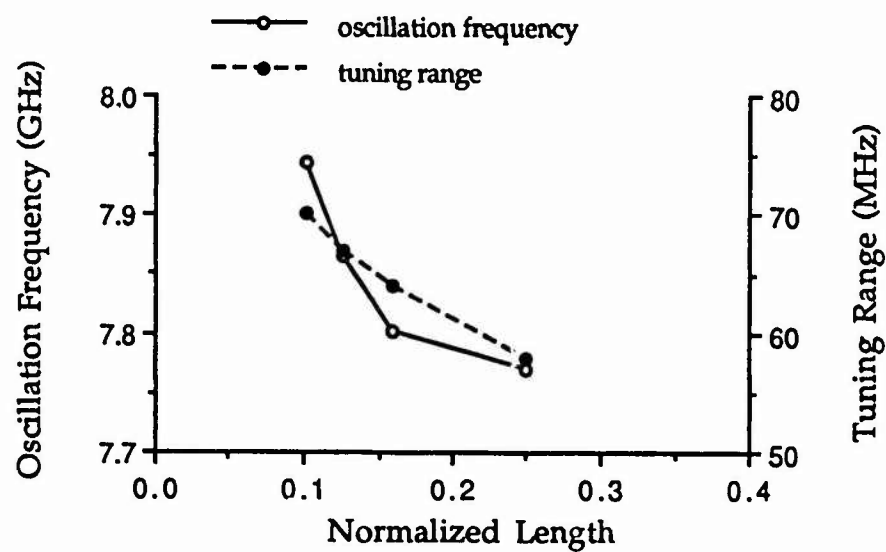


Fig. 2.17 Stub Length Dependence of Oscillation Frequency and Tuning Range

Chapter III

Linear Quasi-Optical Power Combining Array

3.1 Power Combining Array Design

3.1.1 Array

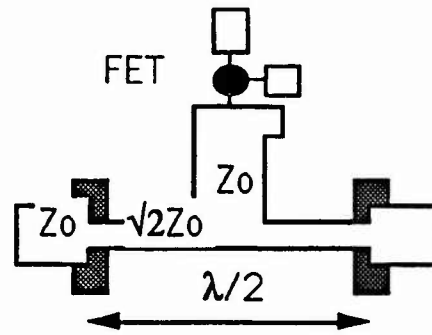
Based on the method described in Chapter II, a quasi-optical power combining array is designed. Since we selected a slot radiator, the alignment of the slot radiators is determined by the desired radiation pattern. If the receiving power is desired to radiate in a particular direction, usually the broadside direction using one source, we can use the multi-slot structure fed by the source[14]. This is based on the following reason. In the case of an M -element slot array with one oscillator, the RF power divided by M is delivered to each slot and radiated. Ideally, a radiated field is proportional to $1/\sqrt{M}$. When the radiation power from each radiator is combined in the broadside direction, the total field at the front of the receiving antenna is proportional to \sqrt{M} [= (the number of radiators, M) \times (each field intensity, $1/\sqrt{M}$)]. Then, the receiving power in the broadside direction has a factor of M compared with that in a single radiator case. Meanwhile, in the case of an N -unit-cell spatial power combiner in which one unit-cell consists of one oscillator and one radiator, the receiving power increases with the factor of N^2 , since the number of sources as well as the number of slots increases simultaneously. Generally speaking, in an N -unit-cell quasi-optical power combining array with M -feed network system such as one oscillator with M slots, the multiplication factor of the receiving power intensity at the broadside

direction is MN^2 . This is one of special features of the multi-feed spatial power combining array.

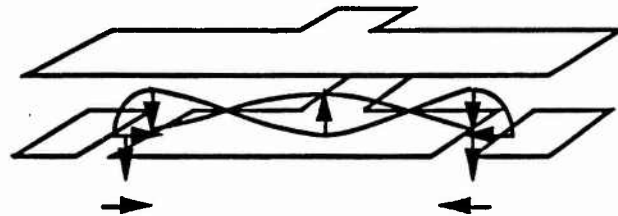
When the unit cell has M slots, i.e., an M -feed network, the generated power from one oscillator is divided into M channels at a branching point. To convey the maximum power to each slot as a load, an impedance matching network is necessary. To make the circuit configuration as simple as possible, one-stage quarter wavelength impedance transformers are used. In addition, we have to take into account the phase of the radiation signal on the slot radiators. To understand this, let us consider a feed network for two slots as shown in Fig. 3.1. Since two divided signals at the branching point have the same phase under this situation, a difference antenna pattern is measured. In order to obtain a sum pattern, an additional $\lambda/2$ microstrip line should be inserted in only one feed line to invert the signal phase. This technique enables us to obtain in-phase signals from a pair of slots in the array with such a configuration. Therefore, the impedance matching and the signal phase adjustment on the slots are important for the multi-feed quasi-optical power combining array.

3.1.2 Power Combiner

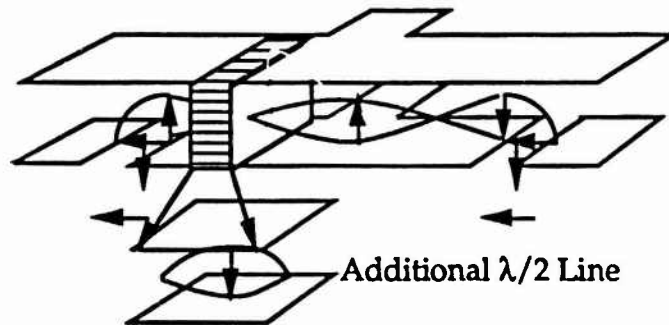
As introduced in Chapter I, transmission lines are used to connect not only the oscillators with the antennas but also the adjacent oscillators together for strong coupling[13]. Therefore, the dominant coupling of the quasi-optical power combining array is through the transmission line. In addition to the two factors described above, there is another important factor for the



(a) Configuration



(b) Field Distribution (Anti-phase Radiation)



(c) Field Distribution (In-phase Radiation)

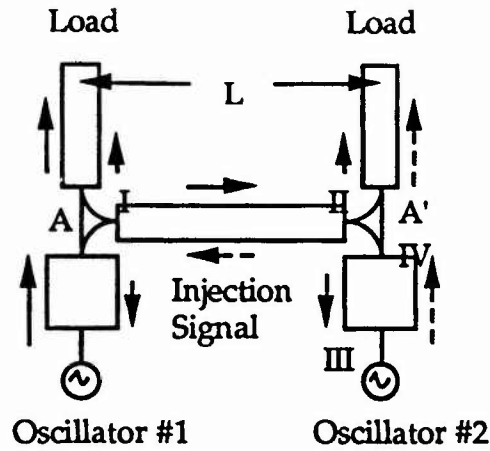
Fig. 3.1 Feed Network for Two Slots

design of the quasi-optical power combining array with strong coupling. Since the array dealt with here is made by a combination of many active sources, it is possible that the array has many modes[39]. Of these modes, the in-phase mode and the anti-phase mode are very important for the antenna pattern as well as combining efficiency. In particular, the in-phase mode is chosen for high combining efficiency in the broadside direction. Therefore, it is essential to investigate the phase of the signal generated from each oscillator. For this purpose, a consideration of signal flow is useful to understand how the argument of the reflection coefficient, Γ_{in} , of each FET oscillator is relevant to the in-phase mode and how the length of the coupling line is determined.

Fig. 3.2 shows the signal flow in an array with two unit-cells. In this case, the unit cell consists of one oscillator and one slot. The signal flow due to Oscillator #1 is shown by solid arrows and that due to Oscillator #2 is indicated by dashed arrows. The length of these arrows indicates the magnitude of signal. When the electrical length of the coupling line between A and A' is $(2n-1)\lambda/2$ (n : integer), the phase progress of the signal from A is π at A'. Further, if the argument of the reflection coefficient of each oscillator is π at the designed frequency, the phase progress of the injected (II-III) and reflected (III-IV) signal to Oscillator #2 becomes π . As a result, the total phase progress of the signal starting from A toward the load is 2π at A'. This implies that the signal at A and the signal at A' toward each load are in-phase. A part of the injection energy at A' (indicated by a solid small arrow) can flow toward the load with the anti-phase to the amplified signal from Oscillator #2

(indicated by a long dashed arrow). Due to the relationship of the ratio of the three characteristic impedances at A or A', two thirds of the energy coming from Oscillator #1 along the coupling line AA' can enter Oscillator #2. However, since the injected energy is amplified with a large gain, the anti-phase signal indicated by the smaller solid arrow toward the load is negligible in comparison to the larger dashed arrow on the same transmission line. As a consequence, if the argument of the reflection coefficient of each oscillator is π and the electrical length for connection between two oscillators is $(2n-1)\lambda/2$, the output signals from the two oscillators are in-phase. Similarly, if the argument of the reflection coefficient of each oscillator is 0, the length of the coupling line between the two oscillators should be $n\lambda$ for the in-phase signals from each oscillator. From this consideration, it is obvious that the argument of the reflection coefficient of the oscillator is important for confirmation of the appropriate length of the coupling line.

(In a summary, these three factors (impedance matching at a branching point, the phase of the radiation signal on the slot and the signal phase from the oscillator) are important to obtain in-phase radiation signals from all slots[14]. On the other hand, the anti-phase mode is still useful for a second harmonic spatial power combining array which will be discussed in detail later. Therefore, it is essential to control these two modes when the quasi-optical power combining array is designed.



Path	Electrical Length	
	$L=\lambda/2, \angle\Gamma=\pi$	$L=\lambda, \angle\Gamma=2\pi$
I - II	π	2π
II - III - IV	π	2π
I - IV	2π	4π

Fig. 3.2 Signal Flow for Two Unit Cells

3.2 Circuit Modeling

3.2.1 Periodic Boundary

When we simulate the quasi-optical power combining array with strong coupling, by replacing the coupling line with an appropriate stub, the mode analysis of the periodic array such as the in-phase mode and the anti-phase

mode can be simplified[25]. A configuration of an infinite array with the periodic structure is shown in Fig. 3.3. In this structure, a maximum field point (open status) is at the middle point of the coupling line connecting the two adjacent oscillators in the in-phase mode case, while a zero field point (short status) is at the same point in the anti-phase mode case. This means that the coupling line is regarded as an open stub in the former and as a short stub in the latter. Therefore, the FET sees a different impedance for each mode from the passive part of the array. Due to this consideration, the infinite array is represented by one unit-cell with the appropriate stub as shown in Fig. 3.4. Here, the middle point of the coupling line is called the plane of the periodic boundary. Which mode can survive depends on the input impedance of the FET oscillator in the steady state oscillation.

3.2.2 Passive Part

So far, we have learned how to incorporate the antenna input impedance and the two operation modes (the in-phase mode and the anti-phase mode) into the circuit model. Of course, the loading seen by the active devices depends on these modes. Using the concept explained in 2.1.1, let us investigate the input impedance of the passive part of the array. As described above, in the periodic structure, a field maximum point (open status) is at the periodic boundary for the in-phase mode, while a zero field point (short status) is there for the anti-phase mode. Once again, let us use the example of the infinite periodic array shown in Fig. 3.4. Characteristic impedances and transmission line lengths required for analysis are given in Fig. 3.4. Using the

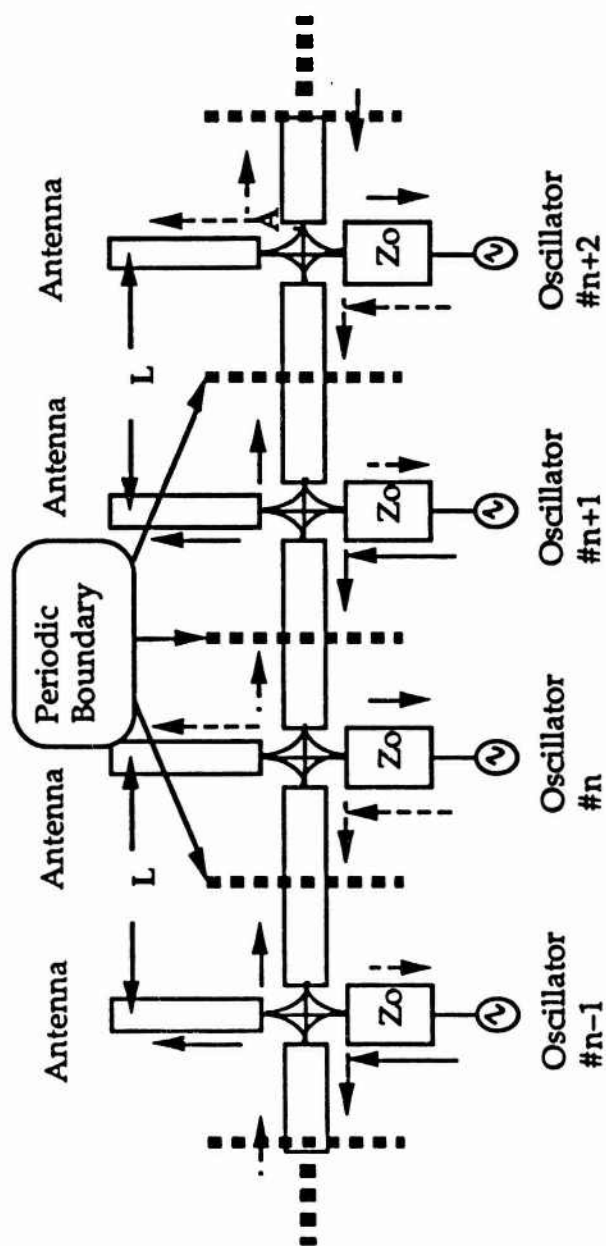


Fig. 3.3 Configuration of Infinite Array with Periodic Structure

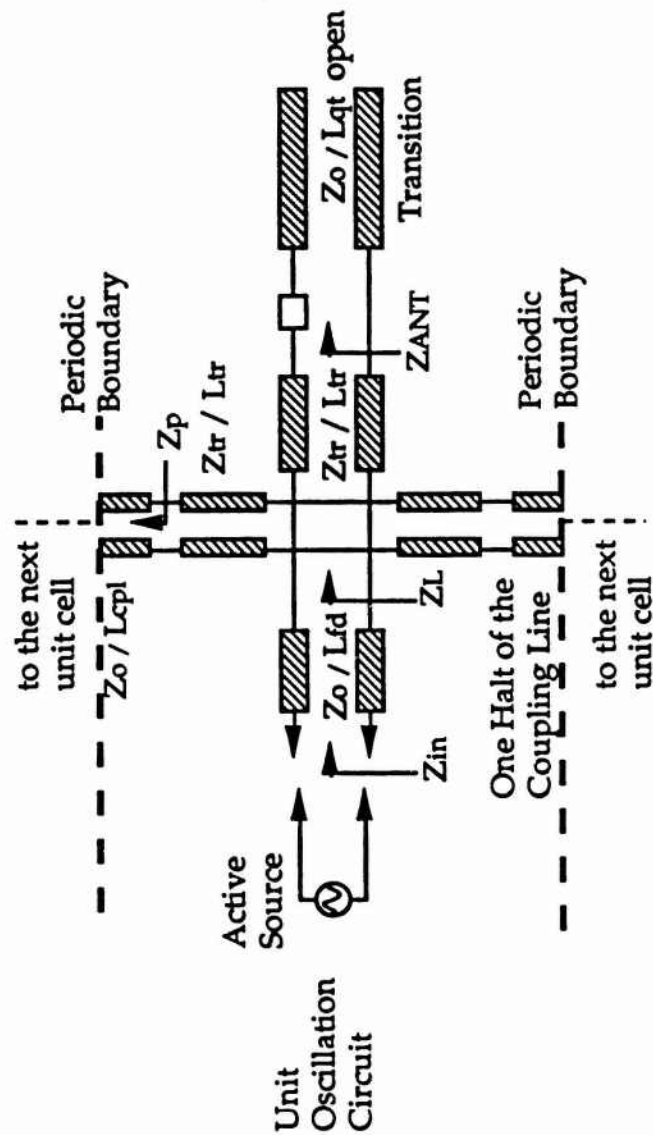


Fig. 3.4 Transmission Line Model for Reduced Infinite Array

ABCD matrix, the input impedance of this circuit at the branching point seen the passive part of the unit cell of the array is

$$Z_{in} = Z_0 \frac{1 + j y_L \tan \beta L_{fd}}{y_L + j \tan \beta L_{fd}} \quad (3.1)$$

where

$$y_L = \frac{Z_0}{Z_L} = \frac{Z_0}{Z_{tr}} \left(\frac{Z_{ANT} j \tan \beta L_{tr} + Z_{tr}}{Z_{ANT} + j Z_{tr} \tan \beta L_{tr}} + \frac{Z_{tr} + j Z_p \tan \beta L_{tr}}{y_L + j Z_{tr} \tan \beta L_{tr}} \right) \quad (3.2)$$

$$Z_p \left\{ \begin{array}{ll} = \frac{Z_{cpl}}{j \tan \beta L_{cpl}} & \text{(In-phase)} \\ = j Z_{cpl} \tan \beta L_{tr} & \text{(Anti-phase)} \end{array} \right\} \quad (3.3)$$

Here, an antenna network consists of an open-circuit microstrip line and a slot. As described before, the slot works as a series impedance as shown in Fig. 2.4. Using this model, the input impedance of this antenna network is calculated as

$$Z_{ANT} = \frac{Z_0}{j \tan \beta L_{qt}} + Z_s \quad (3.4)$$

Here, Z_0 is the characteristic impedance of the $\lambda/4$ microstrip-to-slot line transition and L_{qt} is a physical length of the transition. Z_s is the input impedance of the slot antenna.

For instance, let us consider the following conditions; $f_d=16$ GHz, $Z_0=Z_{cpl}=50 \Omega$, $Z_{tr}=86.6 \Omega$, L_{fd} (the length of the feed line from the active source) $=0.1 \lambda_{om}$. Frequency characteristics of the input impedance of the passive part, Z_{in} , are shown in Fig. 3.5. Each parameter is indicated in Table I. If an equivalent circuit of the FET oscillator is denoted by a series resistance and a reactance, the resistance degrades in steady state oscillation as explained in 2.1.1. Since the active source is designed at -50Ω , the circuit resistance must be less than 50Ω for steady state oscillation. Therefore, the circuit can have the in-phase mode at 17.2 GHz because it satisfies the resonant condition. On the other hand, the anti-phase mode is suppressed since it sees a high resistance which is shown in Table I.

Table I: Input Impedance of Passive Part
at Resonant Frequency for Two Modes

	In-Phase (open)	Anti-Phase (short)
f_0 (resonant frequency)	17.2 GHz	16.7 GHz
Re (Z_{in})	12.4 Ω	251 Ω
Im (Z_{in})	1.0 Ω	-3.9 Ω

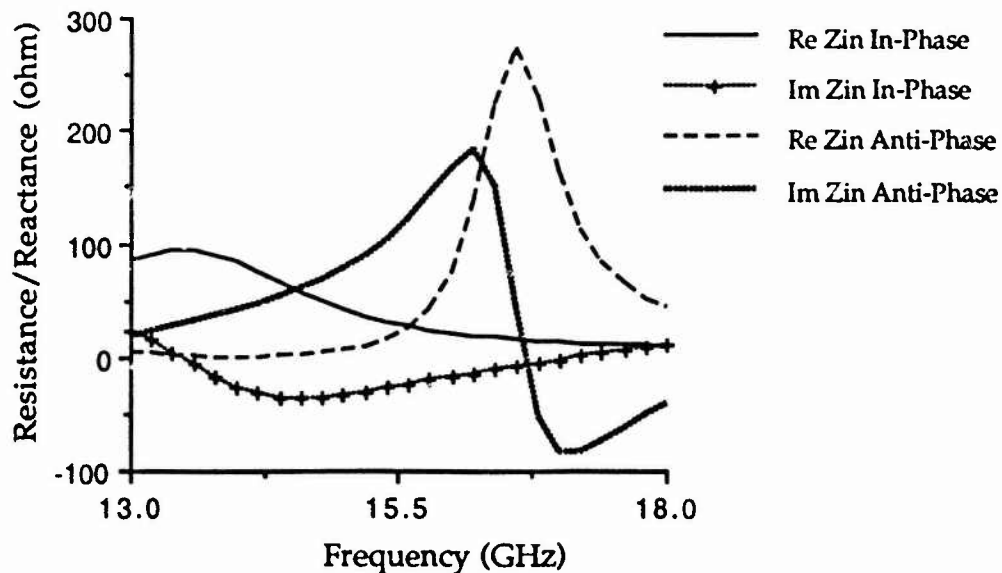


Fig. 3.5 Input Impedance of Passive Part of Reduced Infinite Periodic Array

3.2.3 Large Signal Analysis

In order to check the steady state oscillation frequency, a large signal analysis should be carried out on the entire circuit configuration, including the slot antenna input impedance. For this purpose, the commercially available harmonic balance analysis Libra, by EEsof, was used. The circuit model of the infinite periodic array for large signal analysis is shown in Fig. 3.6. To obtain the steady state oscillation frequency, the ideal directional coupler was used. A simulation result is shown in Fig. 3.7. From this result, the operation frequency 16.3 GHz was obtained for the in-phase mode, while there is no point that satisfies the requirement for the steady state oscillation condition with the anti-phase mode. A comparison of this result with the result of the analysis of the passive part described above shows that the

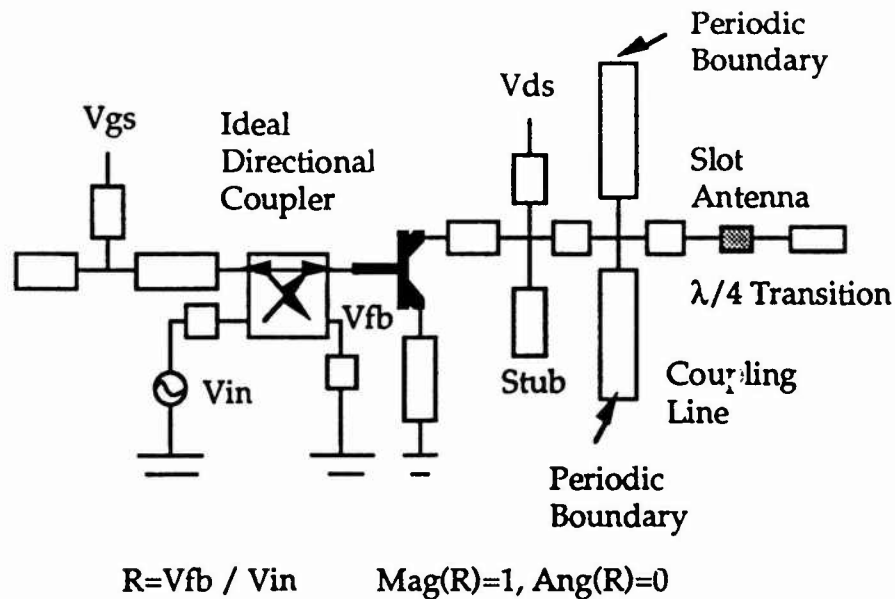
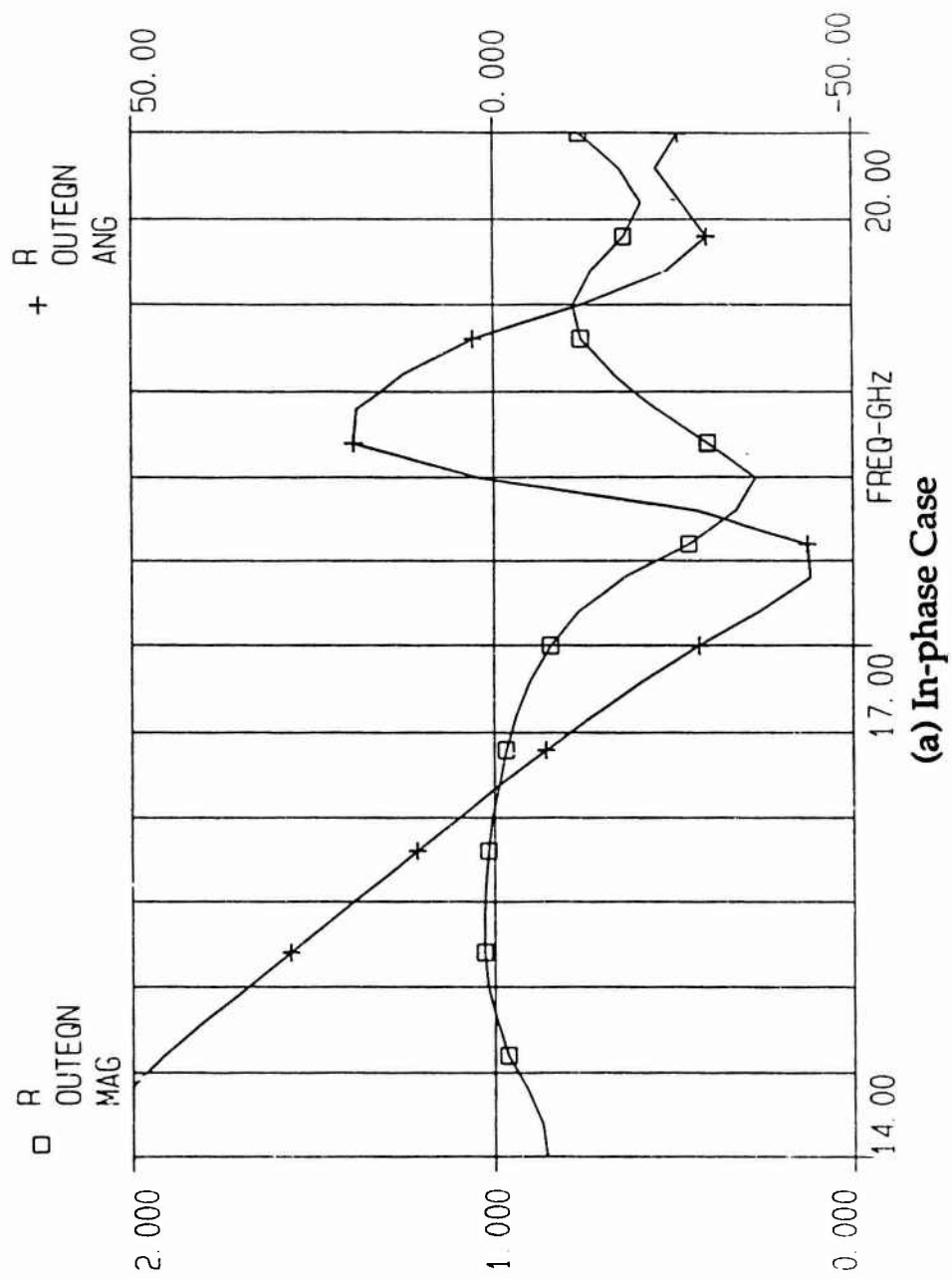


Fig. 3.6 Circuit Model of
Reduced Infinite Periodic Array

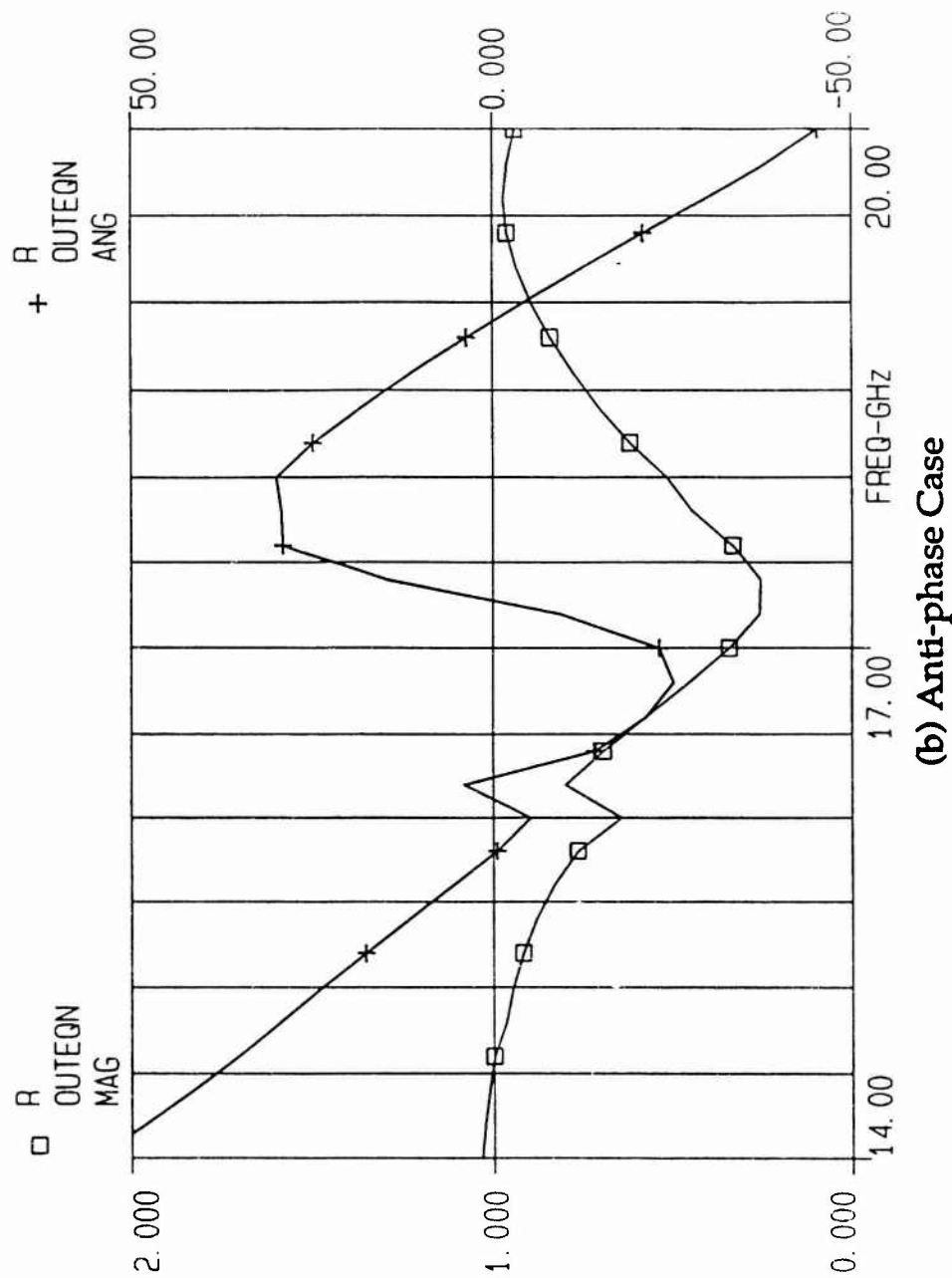
agreement is good. However, the convergence problem sometimes occurred, when the harmonic balance analysis was used. To obtain convergence, accuracy of the analysis was sometime sacrificed.

Thus far, two methods to analyze the quasi-optical power combining array have been demonstrated. One is the analysis of the passive part of the quasi-optical circuit including the input impedance of the slot. The other is the analysis of the entire array using the large signal analysis. Of course, it is better to analyze the circuit using large signal parameters. However, since the good agreement was obtained between the two methods described above, an operating frequency close to the design frequency can be expected by means of the passive part analysis explained above without knowing large signal parameters.



(a) In-phase Case

Fig. 3.7 Variation of R for Reduced Infinite Array



(b) Anti-phase Case

Fig. 3.7 Variation of R for Reduced Infinite Array

3.3 2-element Array

3.3.1 Configuration

In order to invoke the array concept, a 2-element quasi-optical power combining array using microstrip lines was designed. The circuit configuration is shown in Fig. 3.8. Two unit cells are connected with a single microstrip line of length $\lambda_{om}/2$ for strong coupling. The oscillator was designed at 20 GHz using small signal S-parameters to determine the oscillator configuration. Two slots were aligned in the E-plane and separated

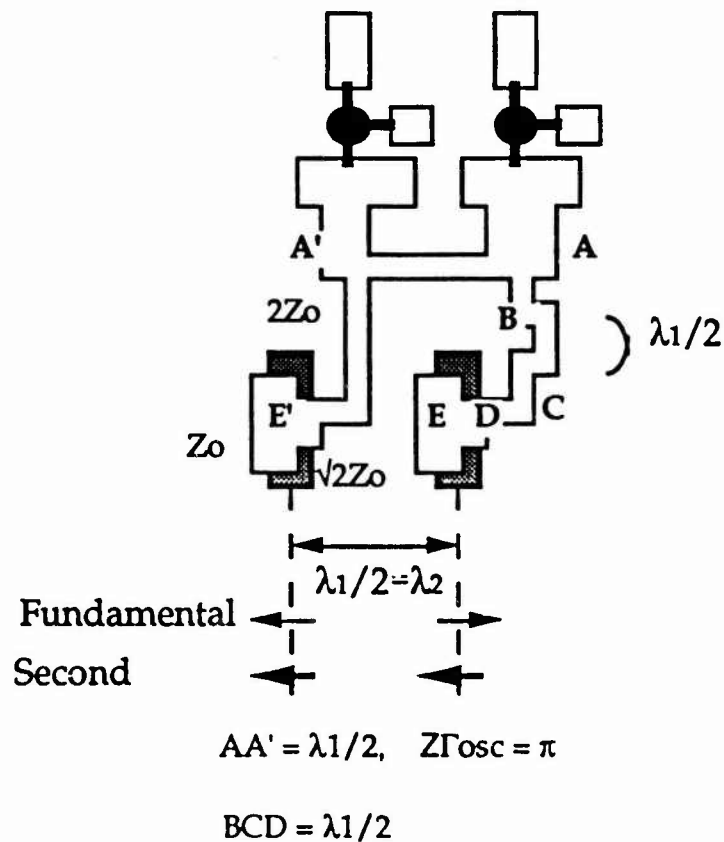


Fig. 3.8 2-element E-plane Microstrip Array

by $0.36\lambda_{of}$. One of the feed lines has an additional $\lambda_{om}/2$ length in order to invert the phase on the slot. This technique is useful for the second harmonic spatial power combiner, which is detailed later.

The next example is a 2-element array using a CPW-fed slot. The oscillator was designed at 10 GHz, and included the open or short stub obtained from the mode analysis described in 3.2.1. The circuit configuration is shown in Fig. 3.9. In this circuit, CPW cross junctions were used for strong coupling. The length of the coupling line is $1\lambda_c$ and the position of the branching point for the coupling is almost $\lambda_c/2$ far from the input of the slot

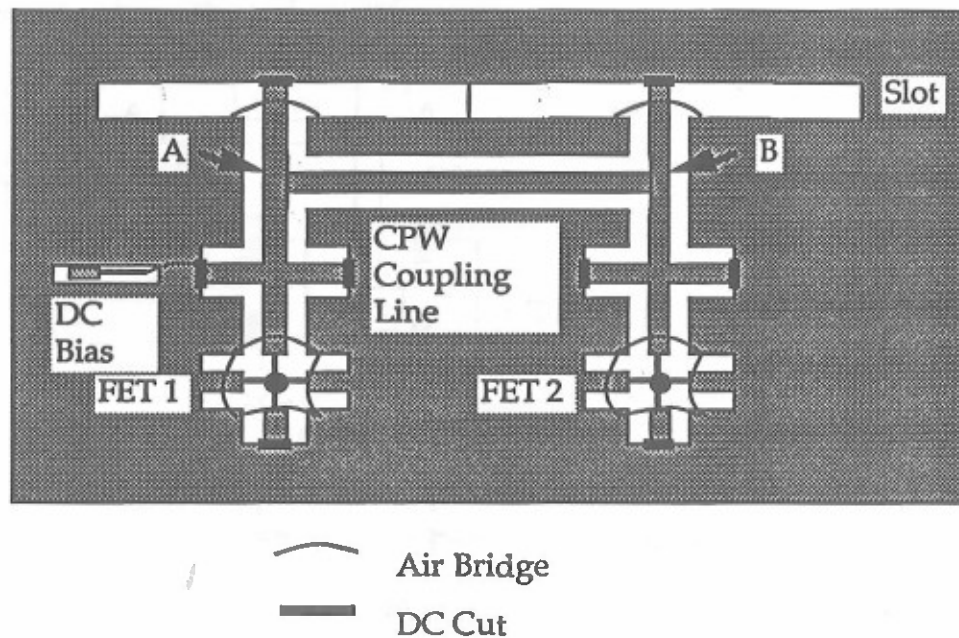


Fig. 3.9 2-element H-plane CPW Array

using the characteristic impedance of $50\ \Omega$ and the length of $1\lambda_c$. The two slots were aligned in the H-plane.

3.3.2 Experimental Results

The package-type FET used in the circuit is NE32484A by NEC and the substrate used is Duroid 5870 by Rogers. The microstrip power combining array operated at 18.7 GHz with $V_{ds}=4.0\text{ V}$ and $V_{gs}=-0.9\text{ V}$ under stable operation. Since we can make use of the coupling line, only one bias network was necessary for V_{ds} . The tuning range was 61 MHz. The radiation pattern of the 2-element array using microstrip lines is shown in Fig. 3.10 which indicates a difference pattern. From this, we can conclude that the argument of Γ_{in} of each oscillator is 0 since the coupling line length is $\lambda/2$. According to the experimental data from the slot antenna operating at 10 GHz, its average gain is 3 dBi. From these data, the ERP of this 2-element microstrip array is estimated as 35.7 dBm.

In the 2-element uniplanar quasi-optical power combining array using CPW's, the package-type FET used is Avantek ATF13284. The circuit substrate is Rogers Duroid 6010. This circuit operated at 7.51 GHz with $V_{ds}=4.0\text{ V}$. Since the gate was floating, only one DC power supply was needed. The lower operation frequency is believed to be due to the interaction between the two oscillators such as load pulling. A difference-pattern was obtained as shown in Fig. 3.11. Since the electrical length of the coupling line is $1\lambda_c$, the argument of Γ_{in} of each oscillator in this case is π .

Therefore, it is possible to fabricate a second harmonic power combining array utilizing this configuration. More detail is discussed in 3.5.

In these two cases, the difference antenna patterns were obtained. To control the antenna patterns, the argument of Γ_{in} at a certain reference plane must be checked, and then the coupling line length be regulated. Otherwise, the appropriate stub should be used to invoke the desired mode in the design. In fact, we sometimes failed to obtain the in-phase mode due to unknown parasitic reactances such as a soldering connection and a bonding wire. However, in a monolithic circuit, it is believed that the modes can be controlled by using the design method described here, because most parameters are predictable.

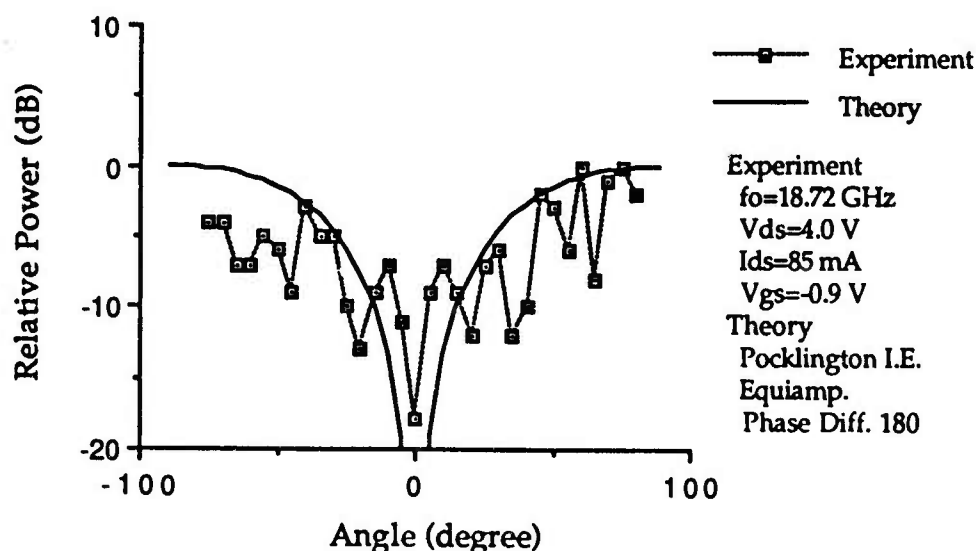


Fig. 3.10 Radiation Pattern of 2-element Microstrip Array

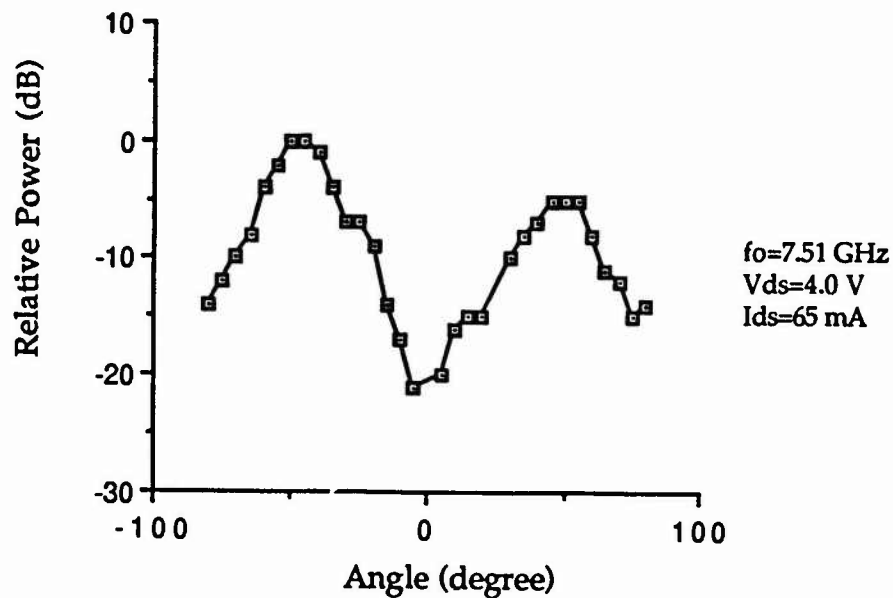


Fig. 3.11 Radiation Pattern of 2-element CPW Array

3.4 6-element Linear Array

3.4.1 Configuration

Using the single FET-single slot oscillator described in Chapter II as a unit cell, a periodic linear quasi-optical power combining array with six unit cells was designed[40]. The circuit made by connecting all oscillator outputs with a single microstrip line is shown in Fig. 3.12. The oscillator was designed at 17 GHz. Six slot radiators are periodically aligned in the H-plane. In order to increase the packing density, the distance between the centers of the two adjacent slots is $0.77\lambda_{of}$. As described before, the mutual coupling of the antennas can be neglected due to the strong coupling by direct connection

(with a transmission line. Since the circuit has periodicity, the analysis and design can be simplified by replacing the coupling line with an appropriate stub.

A non-periodic power combining array was made with symmetric structure. Fig. 3.13 shows the configuration of a nonperiodic linear quasi-optical power combining array in the H-plane with six unit cells. Each oscillator was designed at the same frequency of 17 GHz as that of the periodic array. The outer slot length increased by 2 % and the center of the outer slot was placed with 2 % increased shift (the chirped-off feed). This 2 % shift was chosen not to change the antenna pattern significantly but to widen the tuning range, which is a result of the low-Q structure of the nonperiodicity.

3.4.2 Experimental Results

The FET and the substrate used here were ATF 26884 and Duroid 5870, respectively. The operating frequencies of 15.60 GHz with $V_{ds}=4.3$ V and $V_{gs}=-2.7$ V and 15.64 GHz with $V_{ds}=4.1$ V and $V_{gs}=-2.4$ V were obtained from the periodic and nonperiodic arrays. By making use of the coupling line, only one bias network was necessary for V_{ds} . According to 3.2, the predicted operating frequencies were 17.2 GHz from the passive part analysis and 16.3 GHz from the large signal analysis for the infinite periodic array. The agreement between the experimental data and the theoretical calculations is good even though we did not take into consideration the finite extent of the array. It is understood that the effect of the edge (boundary) oscillators

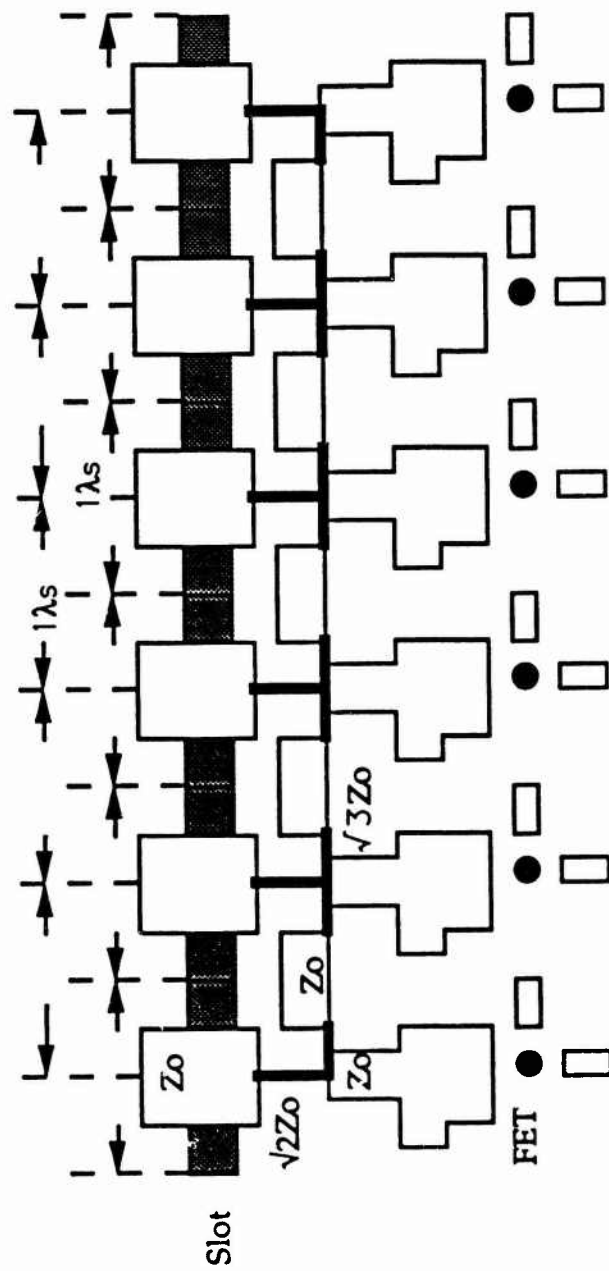


Fig. 3.12 6-element Periodic Linear Quasi-Optical Power Combining Array
Using Microstrip Lines

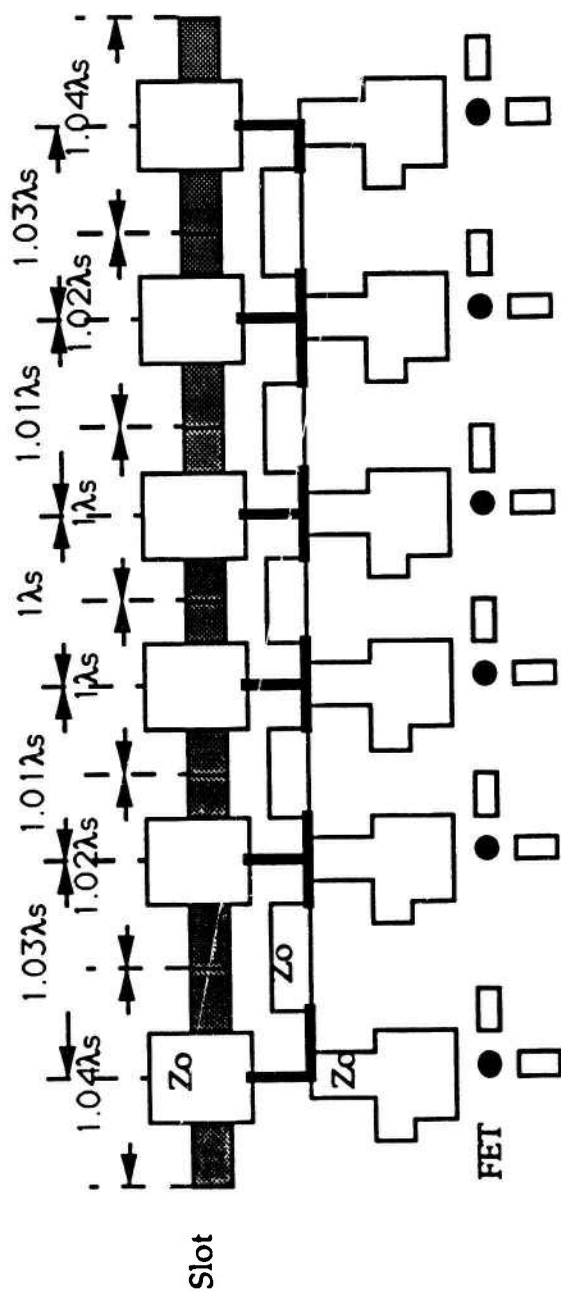


Fig. 3.13 6-element Nonperiodic Linear Quasi-Optical Power Combining Array Using Microstrip Lines

becomes weak as the number of the oscillator increases. The tuning range of the periodic array was compared with that of the non-periodic array. The 58 MHz for the former and the 100 MHz for the latter were obtained, respectively. As expected, the tuning range increased by 72 %.

The antenna patterns of the periodic and nonperiodic arrays and the theoretical pattern assuming equi-amplitude and equi-phase excitations of the periodic structure are shown in Fig. 3.14. Sharp main lobes are obvious and agreement between the theory and the experiment is very good. There is no significant difference between the periodic array antenna pattern and that of

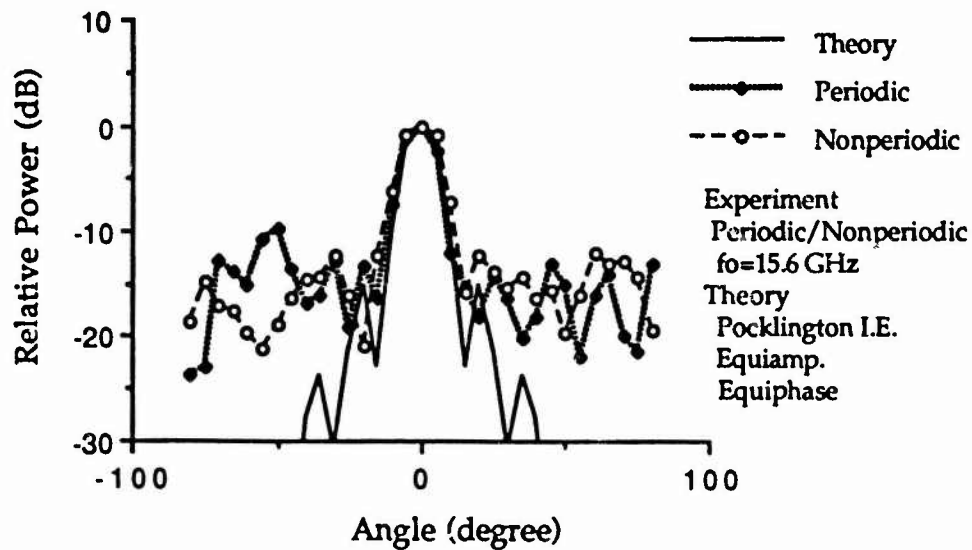


Fig. 3.14 Antenna Pattern Comparison for 6-element Linear Arrays

(the nonperiodic one. Increasing sidelobes were resulted from a defect of measurement (receiver noise). Compared with a single element or a few elements in an array, the oscillation spectrum was sharp and stable in the periodic array. Perhaps, it is due to a relatively higher Q structure, which may suppress undesired modes. Or the relatively larger power in the main lobe may hide defects in the circuit structure and/or from the experimental set-up. In any cases, the antenna pattern improves as the number of oscillators increases, provided that the circuit can maintain a stable operating condition.

3.4.3 Empty Oscillator Array

(In a practical solid-state array radar, the field distribution on the antenna is adjusted to obtain low sidelobes by the tapered distribution and the decreasing intensity distribution. The former is accomplished by reducing an output of the oscillator, while the latter is carried out by increasing the number of empty oscillators (no oscillation source) from the center toward the edge. To obtain the fundamental data for the decreasing intensity distribution, some oscillator FET's in the periodic array were taken away, and then the tuning range and the antenna pattern were measured. This is also important from the view-point of a nonperiodic power combiner. In the case of the array with 4 FET's, the operation frequency was 16.7 GHz with $V_{ds}=4.4$ V and $V_{gs}=-2.3$ V and the array with 5 FET's operated at 16.3 GHz with $V_{ds}=4.2$ V and $V_{gs}=-1.6$ V. Fig. 3.15 shows the antenna pattern in the case of the 4-FET array and the 5-FET array. In spite of the nonperiodicity

to the FET alignment, the array worked well and indicated the in-phase-like antenna patterns with slightly wider mainlobes. For comparison, a theoretical antenna pattern with different amplitude and equi-phase was also indicated. The amplitude ratio of the source exciting the slot is 1 : 0.5 : 0. Due to the good agreement, it can be concluded that the distribution of the sources is a tapered distribution. The maximum tuning range of the 4 FET array and the 5 FET array were 55 MHz and 145 MHz, respectively. Of course, this tuning range depends on the position of the empty oscillators.

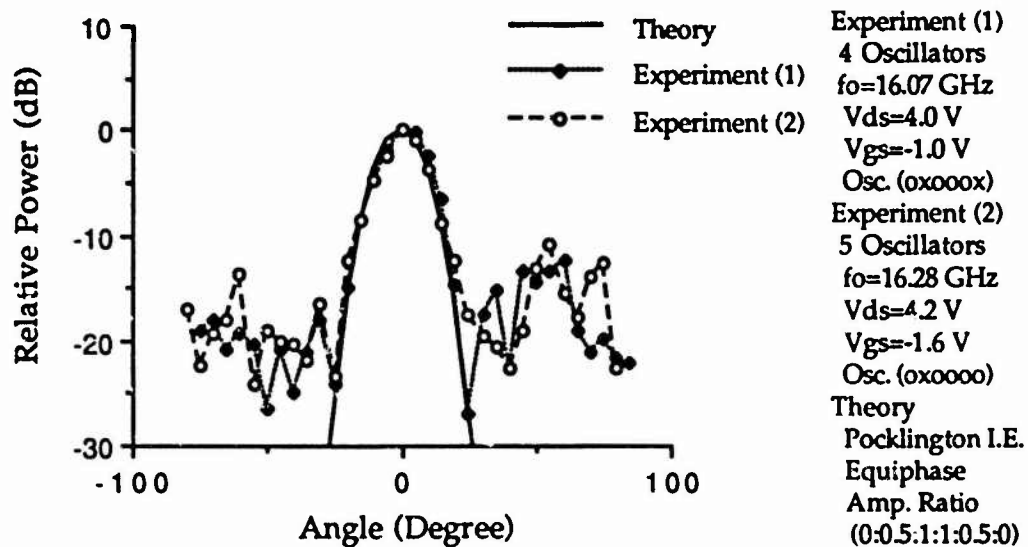


Fig. 3.15 Antenna Pattern Comparison
for 6-element Empty Oscillator Array

3.5 Second Harmonic Spatial Power Combining Arrays

3.5.1 Concept

To confirm the capability of the FET for use in active antennas at millimeter-wave frequencies, a second harmonic spatial power combining array[41] was made by using the nonlinear effect of the FET[13]. When we make use of the second harmonic signal, the antenna patterns of the second harmonic power combining array should be designed to spatially separate the desired signal from the fundamental power. For instance, the second harmonic power should be effectively added up (sum pattern), while the fundamental power is cancelled (difference pattern) in a certain (typically, the broadside) direction as shown in Fig. 3.16. Design of such an array

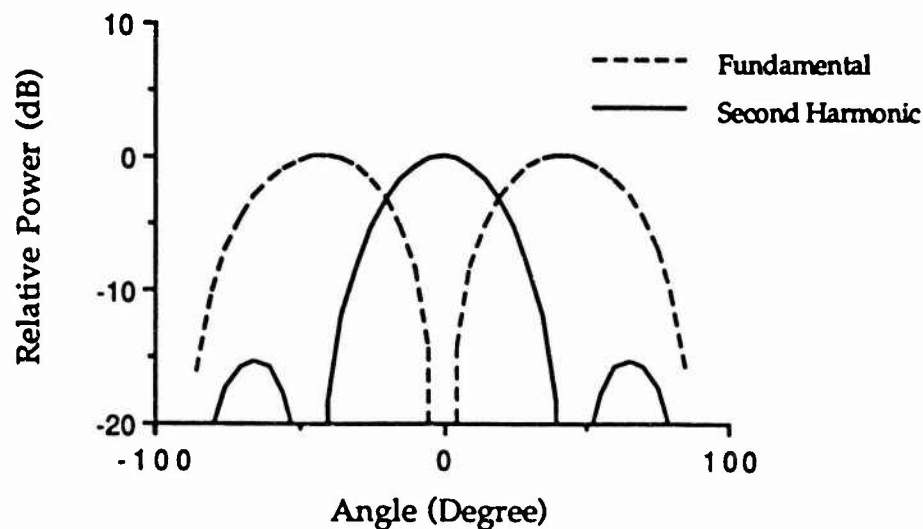


Fig. 3.16 Ideal Antenna Pattern of Second Harmonic Spatial Power Combining Array

requires appropriate phase relationships in the direction of interest, such as the broadside direction, for both the fundamental and the second harmonic.

3.5.2 Configuration

In the case of the second harmonic power combining array, the design of the oscillators, the characteristic impedance and the lengths of the coupling lines for the fundamental frequency should be distinguished from the design of the slot and the lengths of the $\lambda/4$ transition for the second harmonic. Making use of the results of 3.3, let us consider the circuit of two oscillators with two slots in the E-plane as shown in Fig. 3.8. According to 3.1, since the number of the oscillators is equal to that of the slots, i.e., a single-feed network, we need not consider the impedance matching at a branching point. In regard to the signal phase from the two oscillator outputs, an argument of Γ_{in} , π , was obtained for the oscillator from the preliminary experimental result. Therefore, the length of the coupling line must be $(2n-1)\lambda/2$ to obtain the in-phase fundamental signals. However, since we want to pick up only the second harmonic signal in the broadside direction, it is necessary to add an extra $\lambda_{m1}/2$ to one of the microstrip feed lines. This is because only one of the phases of the fundamental frequency signal on the two slots is required to be inverted. These phases of the radiation signal on the slots are also shown in Fig. 3.8. Each slot has the length of $1\lambda_{s2}$ and the width of $0.081\lambda_{s2}$. Each oscillator has -50Ω input impedance and the slots are separated by $\lambda_{m1}/2(=\lambda_{m2})$. The oscillator circuit and the slot are electromagnetically coupled through the $\lambda/4$ microstrip-to-slot line transition.

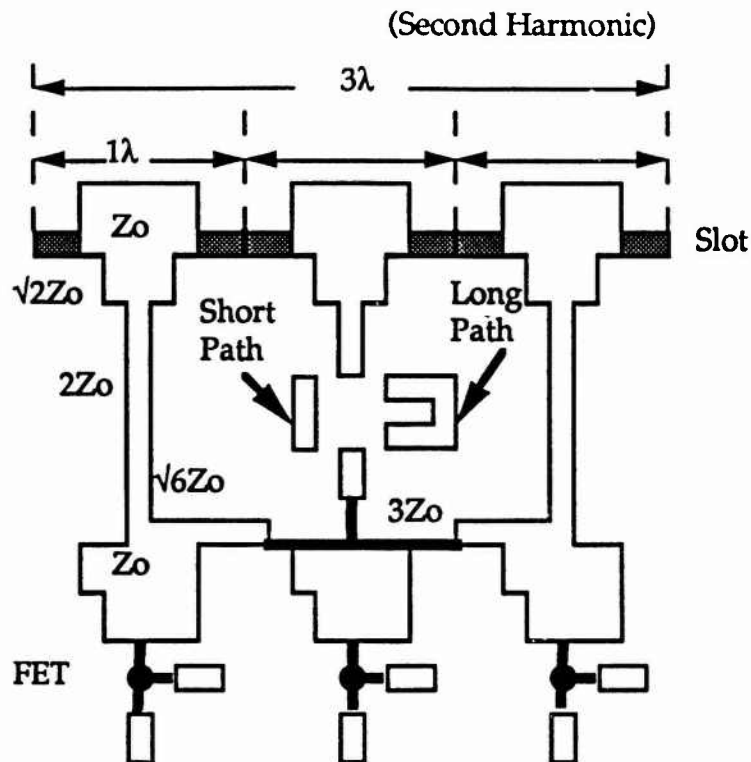


Fig. 3.17 3-element Second Harmonic Spatial Power Combining Array

The next example is a 3-element array in the H-plane[42]. Fig. 3.17 shows the configuration of a 3-element spatial power combiner array designed at 20 GHz for the second harmonic frequency. The input impedance of each oscillator is -50Ω for the fundamental frequency of 10 GHz by using small signal S-parameters. In order to electromagnetically couple a feed line with a slot radiator, a $\lambda/4$ microstrip-to-slotline transition is also used. From the preliminary experiment, the argument of Γ_{in} was found to be π . Therefore, if the length of the coupling line is $\lambda_{m1}/2$, the radiation

signals of the second harmonic as well as those of the fundamental frequency from the slots are in-phase when all three feed lines from each branching point (shown as A,B,C in Fig. 3.17) to the slot are the same. This corresponds to the short path on the center feed line shown in Fig. 3.17. However, for the in-phase for the second harmonic and the anti-phase for the fundamental on the slot, an additional $\lambda_{m1}/2$ is required to invert the phase on the center slot (shown as a long path on the center feed line in Fig. 3.17). By means of control of path length between an oscillator and a slot as well as the coupling line length of the adjacent oscillators, the in-phase radiation for the second harmonic and the anti-phase condition for the fundamental frequency are obtained from the slots aligned in the H-plane.

To realize the uniplanar second harmonic linear quasi-optical power combining array using the results of 3.3, the 4 unit cells using CPW's were combined. The circuit structure of the H-plane linear array is shown in Fig. 3.18. From the results of the circuit shown in Fig. 3.9, the argument of Γ_{in} of π was found for the fundamental frequency. When the second harmonic signal generated from the FET oscillator travels along the coupling line, the second harmonic outputs are considered to be in-phase. As a result, the second harmonic frequency signal can be added up effectively and the fundamental signal be reduced in the broadside direction by adjusting the length of the coupling line.

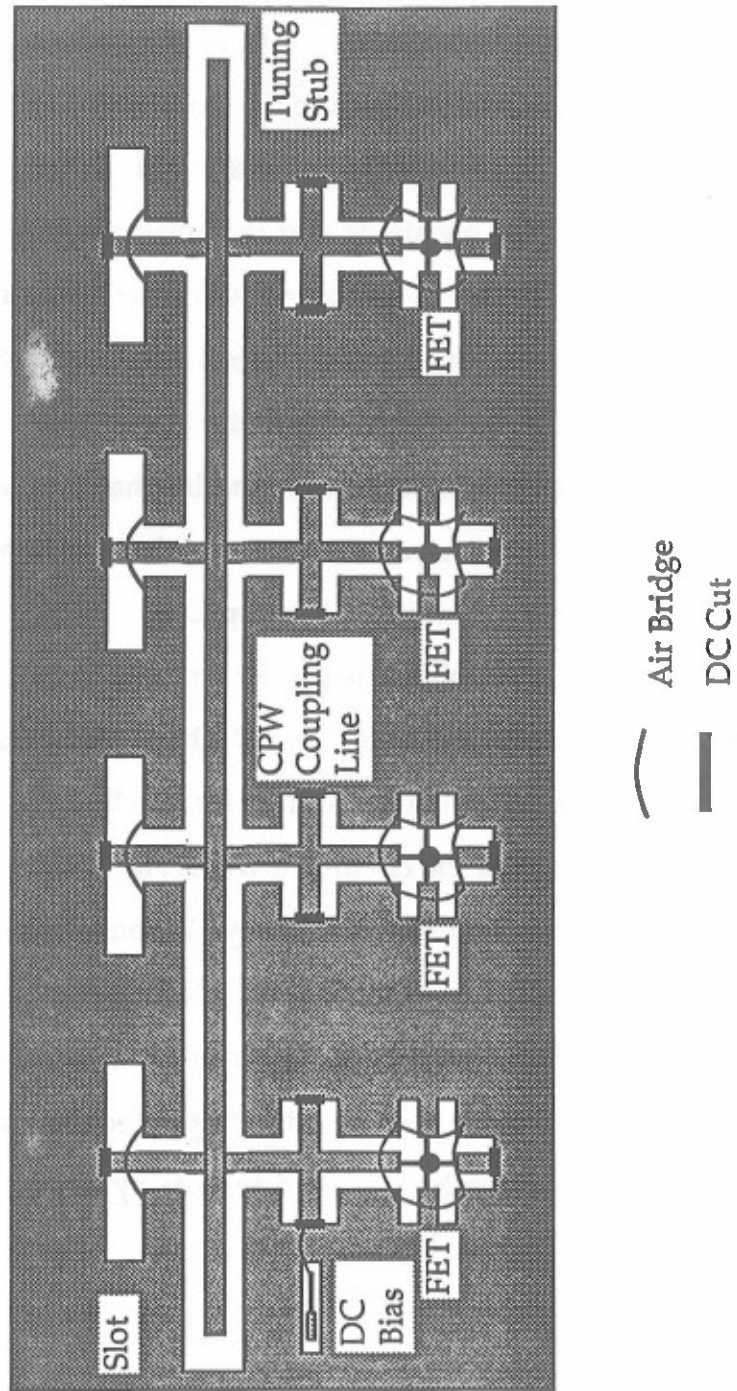


Fig. 3.18 4-element CPW Second Harmonic Spatial Power Combining Array

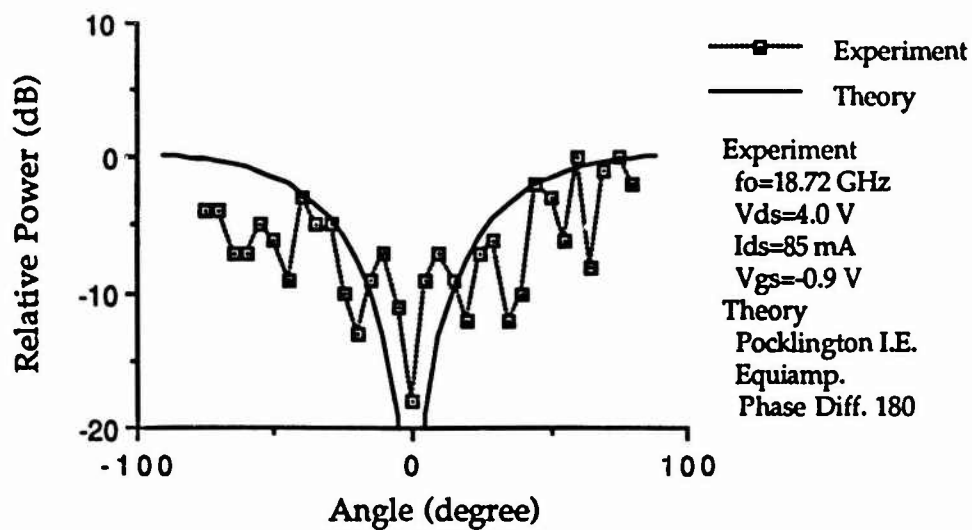
3.5.3 Experimental Results

For the 2-element E-plane millimeter-wave array shown in Fig. 3.8, the fundamental and second harmonic operating frequencies with $V_{ds}=4.0$ V and $V_{gs}=-0.9$ V were 18.7 GHz and 39.3 GHz, respectively. The substrate used is Duroid 5870 and the FET used is NE32484A. The tuning range of this circuit is controlled by changing V_{ds} and V_{gs} and was 377 MHz near the second harmonic frequency. The observed patterns and the theoretical patterns for the fundamental and the second harmonic frequencies are shown in Fig. 3.19 with good agreement. In the broadside direction, it is found that the second harmonic power is effectively added up, while the fundamental frequency power is cancelled.

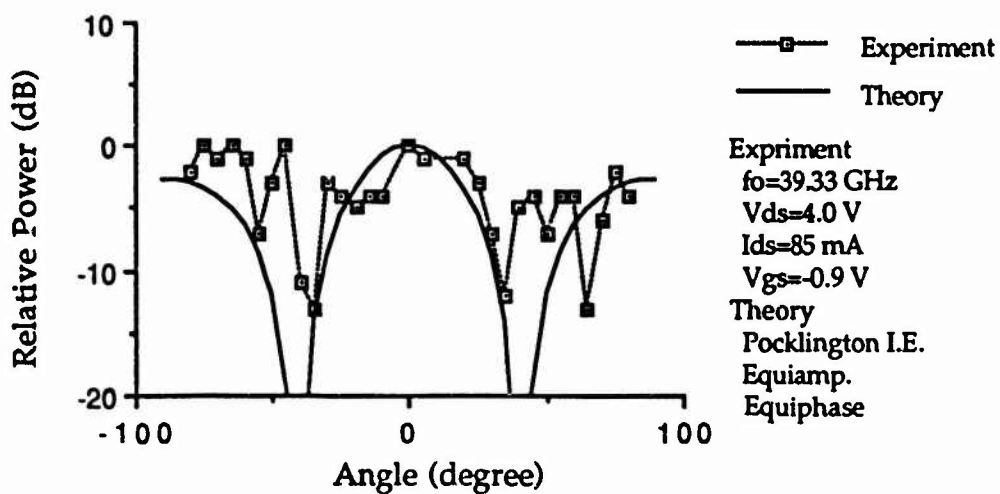
The 3-element H-plane array shown in Fig. 3.17 operated at 9.9 GHz for the fundamental and at 19.8 GHz for the second harmonic with a stable locking status ($V_{ds}=4.3$ V and $V_{gs}=-2.2$ V). The FET used is the model ATF26884 by Avantek. The tuning range obtained by changing the applied DC voltages was 25 MHz. In order to confirm effect due to the different path lengths, antenna patterns for each case were measured. Fig. 3.20 shows the observed radiation pattern of the array with the short path on the center feed shown in Fig. 3.17. As expected, the sum patterns were observed. Theoretical patterns are also shown in Fig. 3.20. At the main beam, the agreement is good. Fig. 3.21 indicates the fundamental anti-phase radiation pattern and the second harmonic in-phase radiation pattern observed from the array with the long path, respectively. The theoretical patterns are also shown for both cases. Note that, in Fig. 3.21, since the phase of the radiation wave from three

(odd number) slots is progressed by 180 degrees due to the anti-phase signal from each oscillator, the radiation power is not completely canceled out in the broadside direction.

A 4-element uniplanar array shown in Fig. 3.18 was fabricated using CPW's. The package-type FET used here is Avantek ATF13284. The circuit substrate is Rogers Duroid 6010. The width of the center strip of the CPW is 25 mil. The slot length of $0.75\lambda_{s2}$ and the slot width of $0.05\lambda_{s2}$ were determined through a preliminary experiment for the CPW-fed slot antenna. Since the gate was floating, only one DC power supply was needed. The operating frequencies of 7.5 GHz for the fundamental frequency and of 15 GHz for the second harmonic were obtained with $V_{ds}=4.0$ V. The large receiving power indicates a good matching condition between the feed CPW and the slot. The operation was very stable without any external cavity and source. The tuning range was 261 MHz around 15 GHz. Note that this tuning range was obtained by changing only V_{ds} from 2.6 V to 4.5 V. Fig. 3.22 shows the antenna patterns for the fundamental and second harmonic frequencies as well as the theoretical pattern for the second harmonic frequency. The fundamental pattern of the anti-phase mode and the second harmonic pattern of the in-phase mode were observed. The agreement between the experiment and the theory at the main-beam is very good. The increased sidelobes may result from the radiation due to a surface wave from the substrate edge. Note that a grating lobe problem was avoided since the separation of the slots is $0.8\lambda_0$ for the second harmonic frequency.



(a) Fundamental Frequency



(b) Second Harmonic

Fig. 3.19 Antenna Patterns of 2-element E-plane Second Harmonic Array

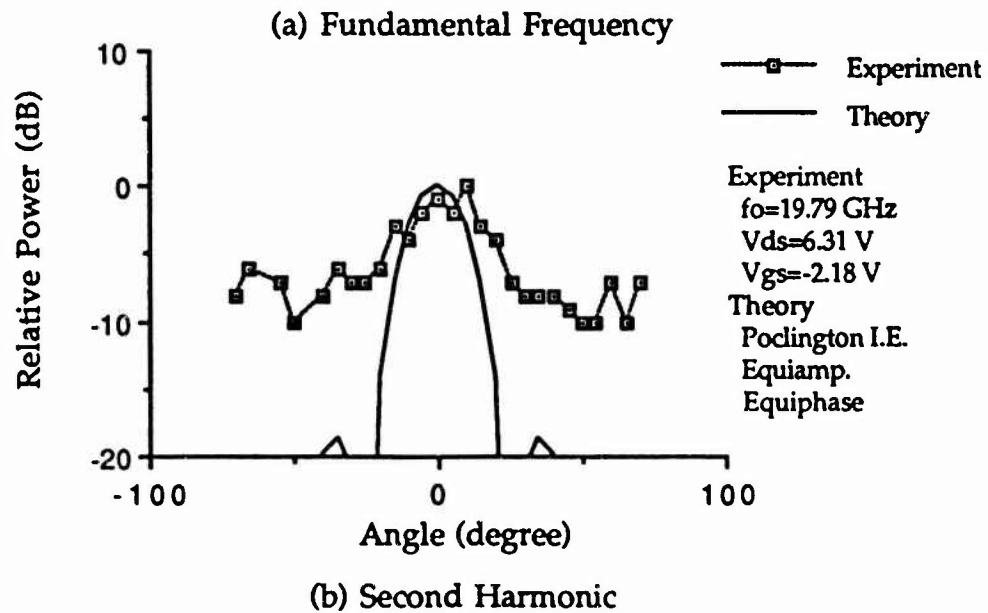
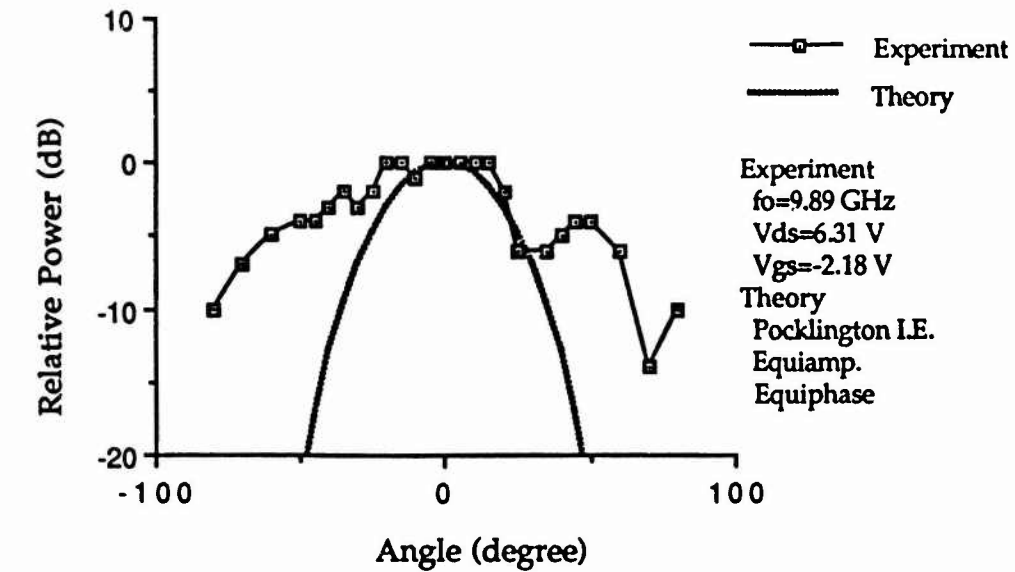
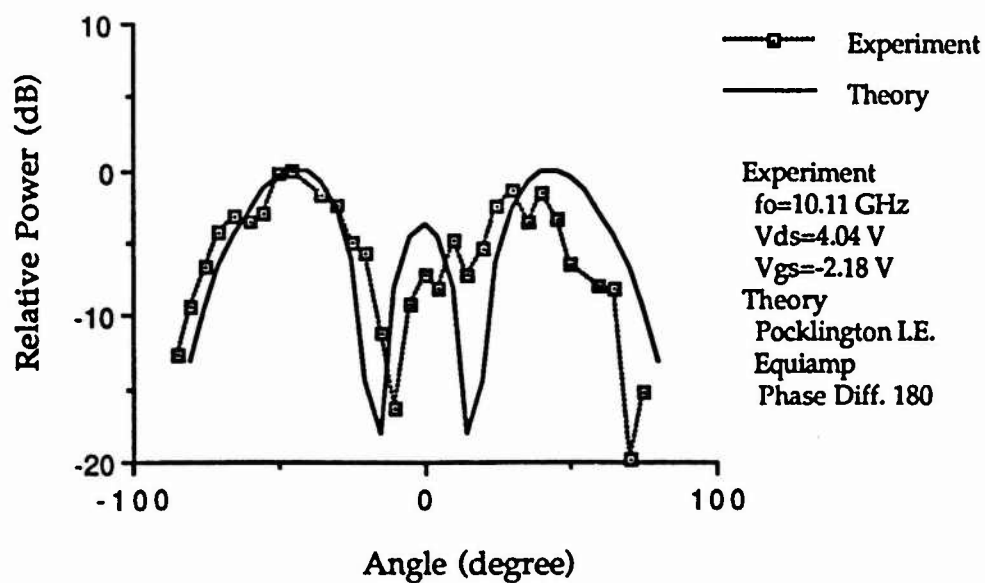
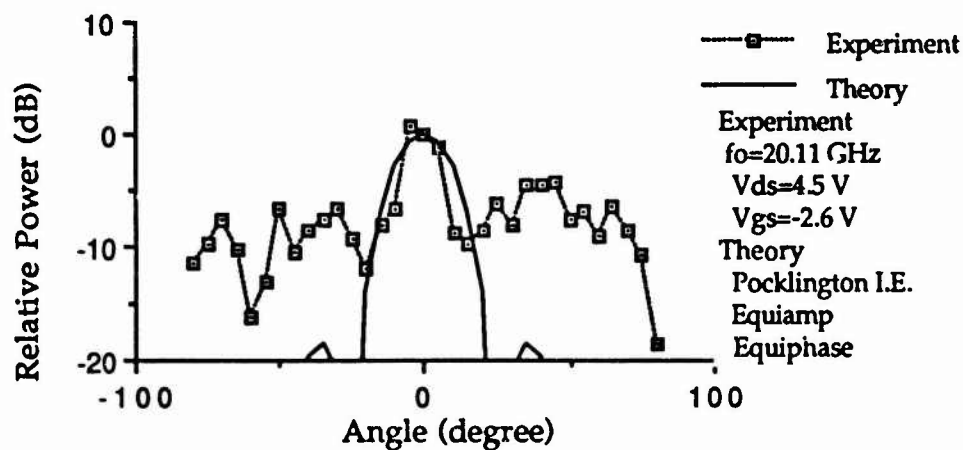


Fig. 3.20 Antenna Pattern of 3-element
Second Harmonic Array with Short Path



(a) Fundamental Frequency



(b) Second Harmonic

Fig. 3.21 Antenna Pattern of 3-element
Second Harmonic Array with Long Path

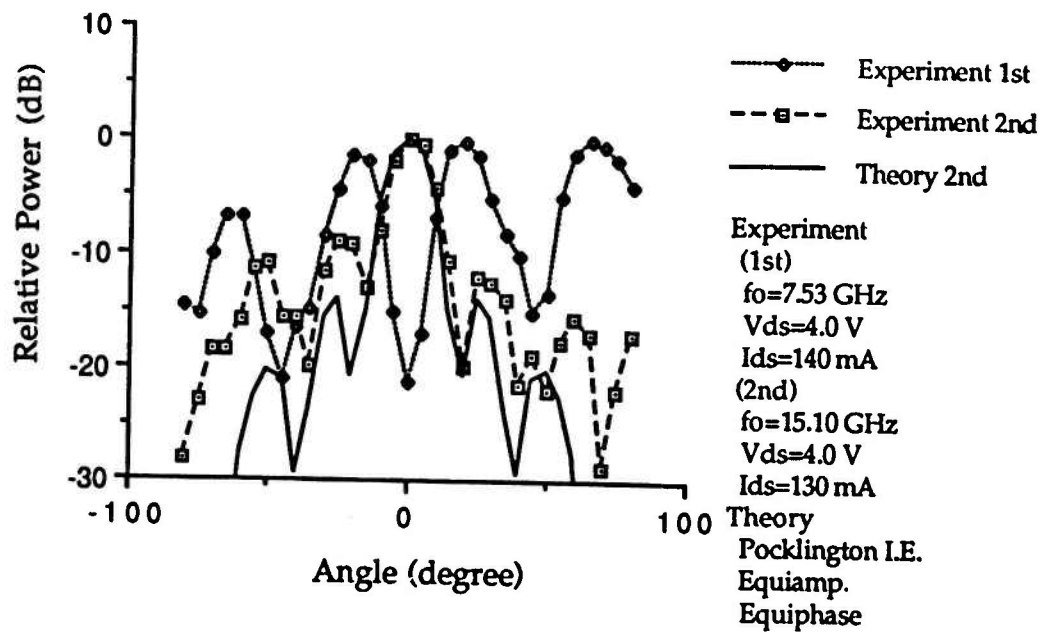


Fig. 3.22 Antenna Pattern of 4-element CPW Second Harmonic Array

Chapter IV

2-dimensional Quasi-Optical Power Combining Array

4.1 Array with 1 Oscillator and 4 Slots

4.1.1 Configuration

To demonstrate the dual polarized planar active antenna operating at 10 GHz, the circuit shown in Fig. 4.1 was designed[14]. At Branching point A, 4 branches are connected. One branch with a characteristic impedance Z_0 is connected to the oscillator. Three others are connected to the four antennas via a one stage quarter wavelength transformer used for impedance matching. The transformers were used to divide RF energy into the four slots equally. If all feed lines to the slots from the branching point A have the same electrical lengths, the phase difference of radiation signals between the two diagonal slots becomes 180° . This results in a difference antenna pattern. In order to create in-phase radiation, an extra $\lambda/2$ transmission line should be added to only one of the two microstrip feed lines which connect the two diagonal slots. In Fig. 4.1, the upper half lines which lead to Slot 2 and Slot 3 including Branching point B has the extra half wavelength transmission line to invert the phase to each diagonal slot (in this case, Slot 2 with respect to Slot 4 and Slot 3 with respect to Slot 1). As a result, the circuit is expected to indicate a sum antenna pattern in the E-plane. Here is one problem. A spacing between the two centers of the diagonal slots is $1.2 \lambda_{of}$. Therefore, the antenna pattern in the E-plane is expected to include a grating lobe. This

problem of a grating lobe could be resolved by the use of a substrate with a higher value of permittivity, since the physical length of the transmission line becomes much smaller.

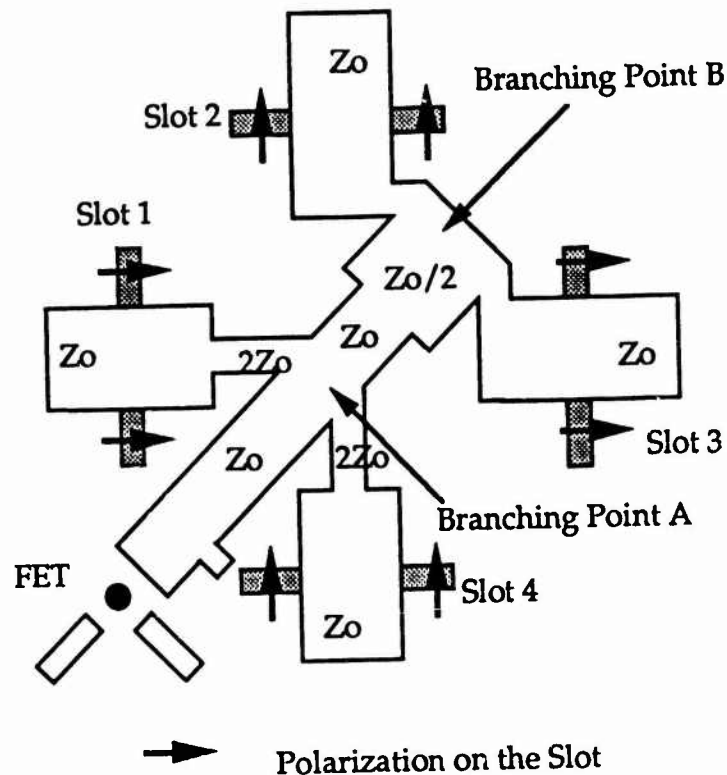
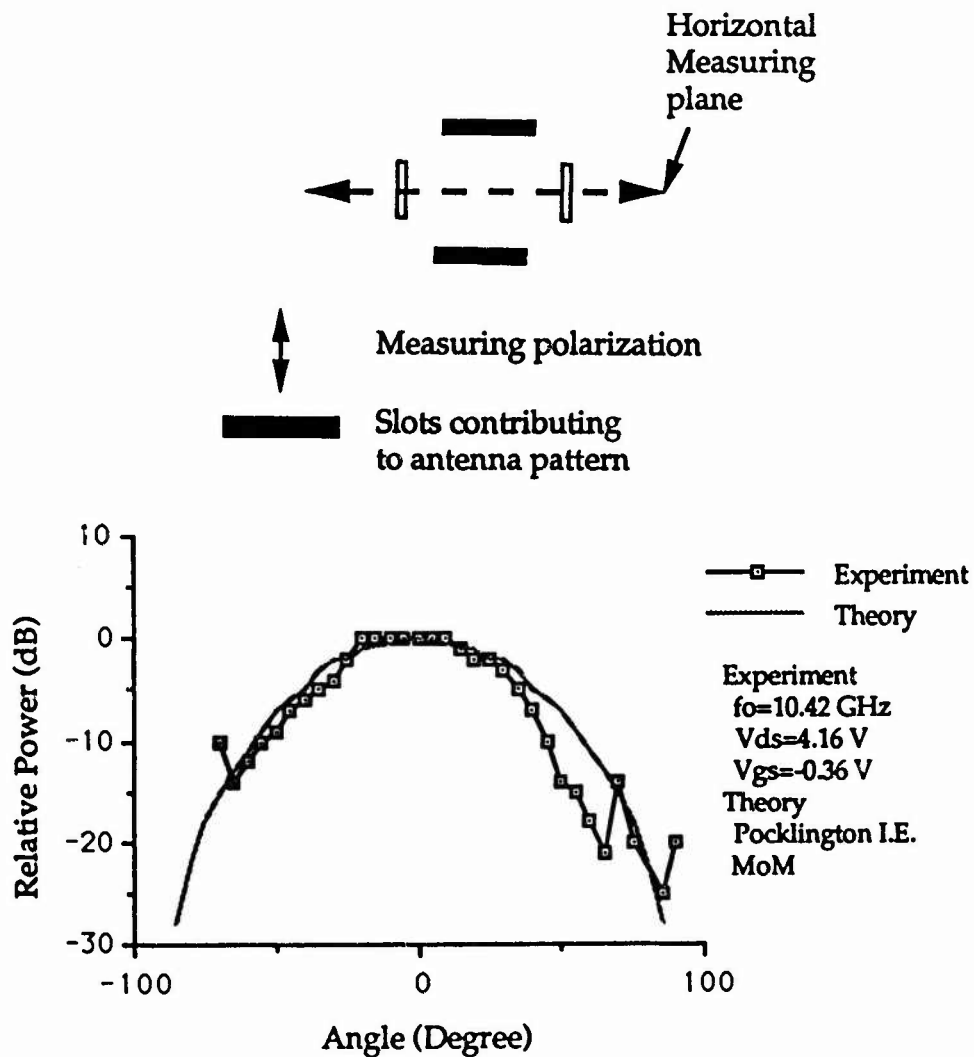


Fig. 4.1 Dual Polarized Array
with 1 Oscillator and 4 Slots

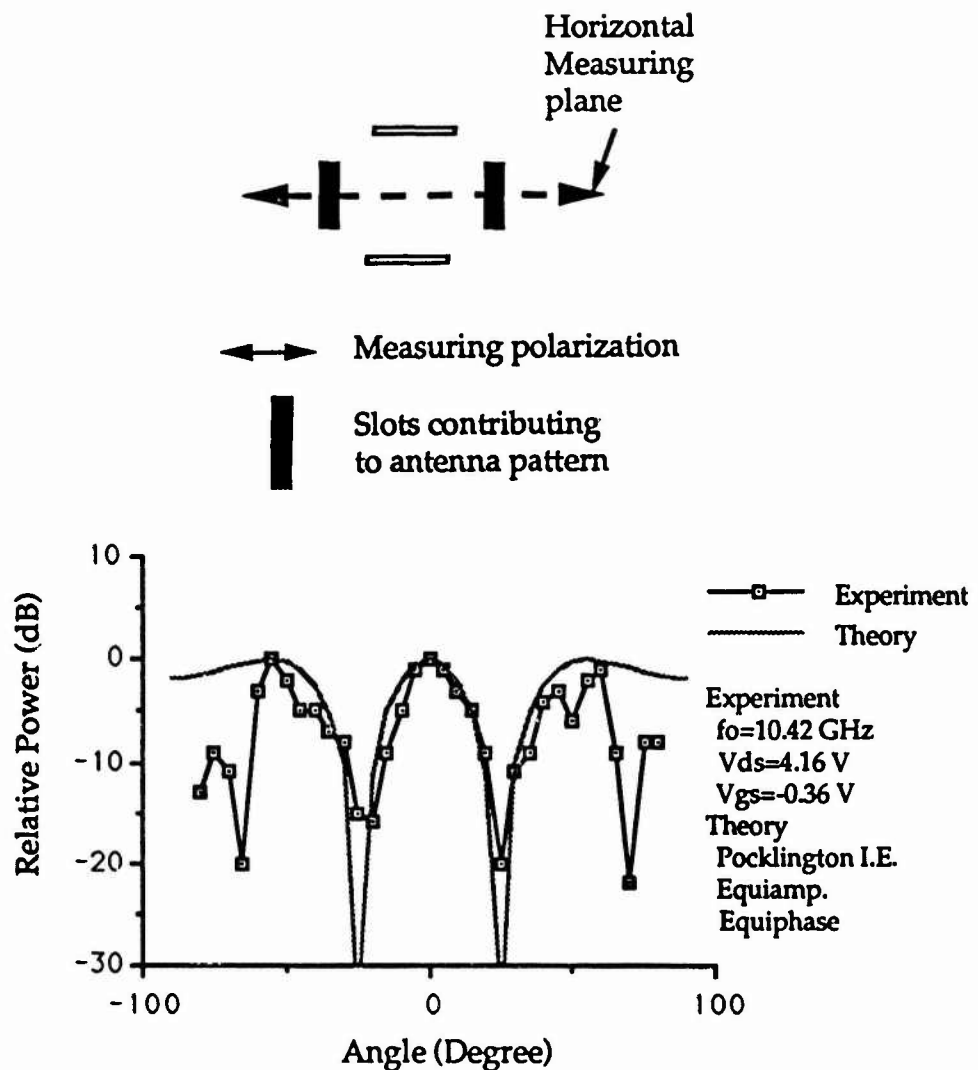
4.1.2 Experimental Results

The operating frequency of the circuit of a single FET oscillator with four slots was 10.4 GHz with $V_{ds}=4.2$ V and $V_{gs}=-0.4$ V. The FET used was



(a) Measurement Case of
One Wavelength Slot Antenna

Fig. 4.2 Antenna Pattern of Dual Polarized Array
with 1 Oscillator and 4 Slots



(b) Measurement Case of
E-Plane 2-Element Array

Fig. 4.2 Antenna Pattern of Dual Polarized Array
with 1 Oscillator and 4 Slots

ATF 26884 and the substrate used was Duroid 5870. From the measured results, the ERP was estimated as 19.23 dBm. Due to the dual polarizations, the antenna pattern for the perpendicular polarization in the horizontal measuring plane is different from that for the vertical polarization in the same measuring plane. As shown in Fig. 4.2, the former indicates a 2-element array in the E-plane, while the latter indicates double $1\lambda_s$ slot antennas aligned in a vertical direction. Therefore, an improved array antenna pattern, i.e., an array factor, is expected in the former case. This results from the narrow slot width. On the other hand, a simple $1\lambda_s$ slot antenna pattern will be observed in the latter case. Fig. 4.2 shows the measured antenna patterns resulting from this fact. Since the distance between the centers of the two diagonal slots is $1.2\lambda_{of}$ in the former case (the E-plane 2-element array), a grating lobe is found in the endfire direction.

4.2 2x2 Array

4.2.1 Configuration

A prototype of a 2-D array has been demonstrated here. Fig. 4.3 shows the configuration of the proposed 2x2 spatial power combining array designed at 20 GHz[43]. The circuit structure consists of two negative resistance oscillators, four slots and the microstrip lines. Each oscillator was designed with an input impedance of $-50\ \Omega$ using the small signal S-parameters. However, an additional microstrip line was added for an appropriate position of the oscillator to avoid disturbing the slot radiation. Further, a gap was created on the microstrip line for the drain DC bias shown

in Fig. 4.3. Therefore, the input impedance of the oscillator at the branching point A or A' was found to be -10Ω .

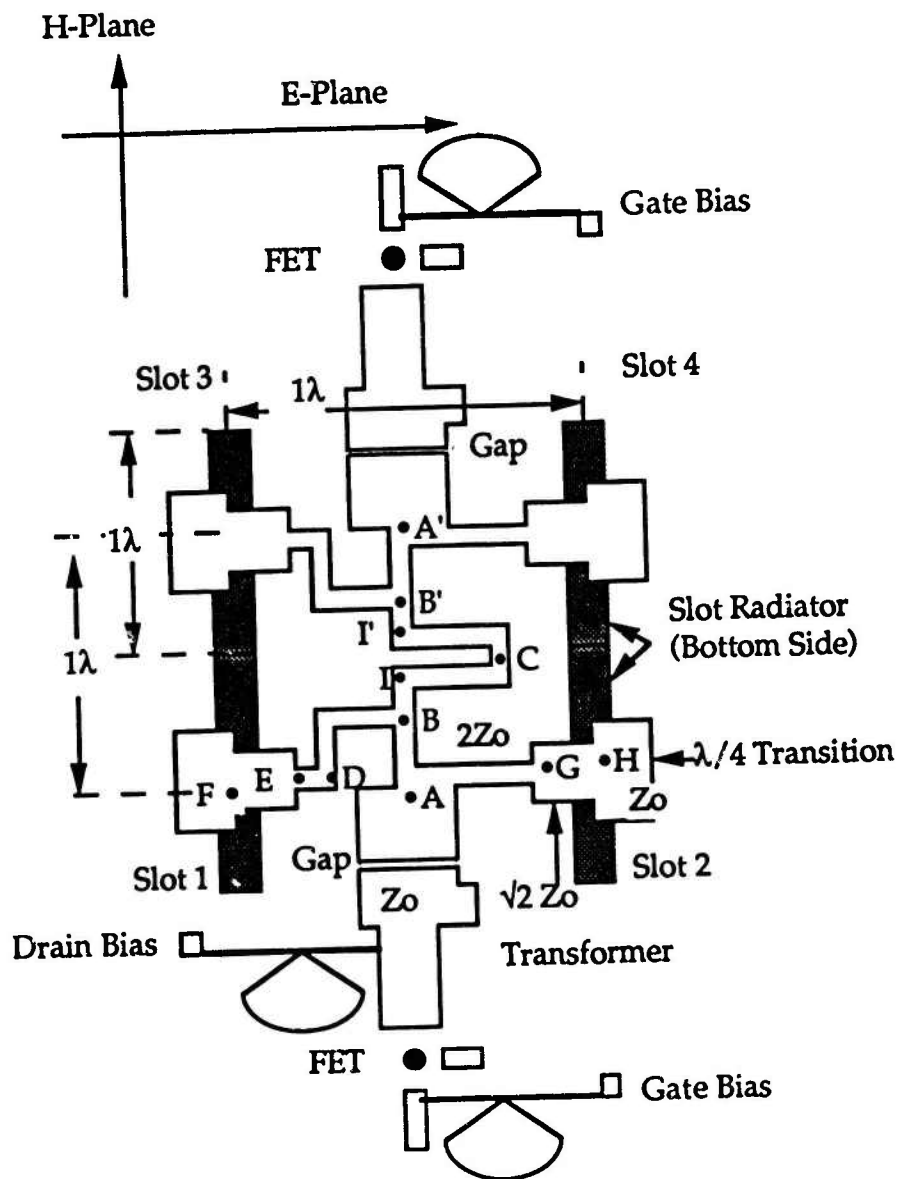


Fig. 4.3 2x2 Spatial Power Combining Array

RF energy generated from one FET oscillator is divided and delivered to a pair of slots (e.g. Slot 1 and 2) in the E-plane. A part of this RF energy flows to lock the other oscillator through a direct coupling (A-B-C-A') between the two oscillators. The locked and amplified signal transmits into the other pair of slots (Slot 3 and 4). To increase packing density, two slots in H-plane separated by a thin line are directly connected. Therefore, the centers of adjacent slots is separated by $1\lambda_{om}$ in the E-plane as well as in the H-plane as shown in Fig. 4.3.

For the design of the quasi-optical power combining array with strong coupling, the three factors are important as discussed in 3.1; the impedance matching at the branching point, the phase of the radiation signal on the slot, and the signal phase difference from the oscillator. First, let us consider the impedance matching at the branching point A in Fig. 4.3 (for convenience of description, points in the lower half in the circuit configuration of Fig. 4.3 are used). RF energy generated from one FET oscillator flows into Slot 1 and Slot 2 through the point A. For simplification, the line B-I-C-I'-B' is neglected for a moment. Since there are two branches at A, the characteristic impedance of the line AB and AG must be $2Z_0$, which is to match the impedance looked into Slot 1 and Slot 2 (Z_0 is the characteristic impedance of the microstrip feed line from the oscillator output). The microstrip line with Z_0 was used as the $\lambda/4$ transition at F and H. Therefore, a one-stage $\lambda/4$ transformer was inserted in the feed line to the slot (EF and GH) for impedance matching between the $2Z_0$ line and the slot input impedance.

In the oscillator with the multi-feed network, we must consider the phase of the radiation signal on the diagonal slots. As shown in Fig. 3.1, if the branching feed lines to the two slots are of the same length, a difference antenna pattern is obtained. In order to obtain the in-phase radiation, an additional half wavelength line is required. In Fig. 4.3, the line A-B-D indicates this additional half wavelength line.

The last is the signal phase from the oscillator. The in-phase mode between the oscillators is accomplished by regulating the length of the microstrip feed lines corresponding to the appropriate argument of Γ_{in} . From the preliminary results, the argument of Γ_{in} equal to π was obtained. In this circuit case, since the straight distance A-A' is $1\lambda_{om}$, the additional $\lambda/2$ line should be inserted in the coupling line A-A' as I-C-I' to obtain the in-phase output signals from these two oscillators. Under this condition, there is no discrepancy with the assumption of neglecting the line B-I-C-I'-B' mentioned above. This is because the length of the line B-I-C is a half wavelength. Therefore, since the field maximum point is at C, there is also the field maximum point at B where the circuit is open.

4.2.2 Analysis

As described in 3.2.2, there are two methods to analyze the quasi-optical power combining array. Here, let us analyze the passive part of the circuit again[25]. The transmission line model of the 2x2 array with the strong coupling is shown in Fig. 4.4. In this case, we can define the symmetric plane at the point C on the coupling line. At this plane, the guided signal has

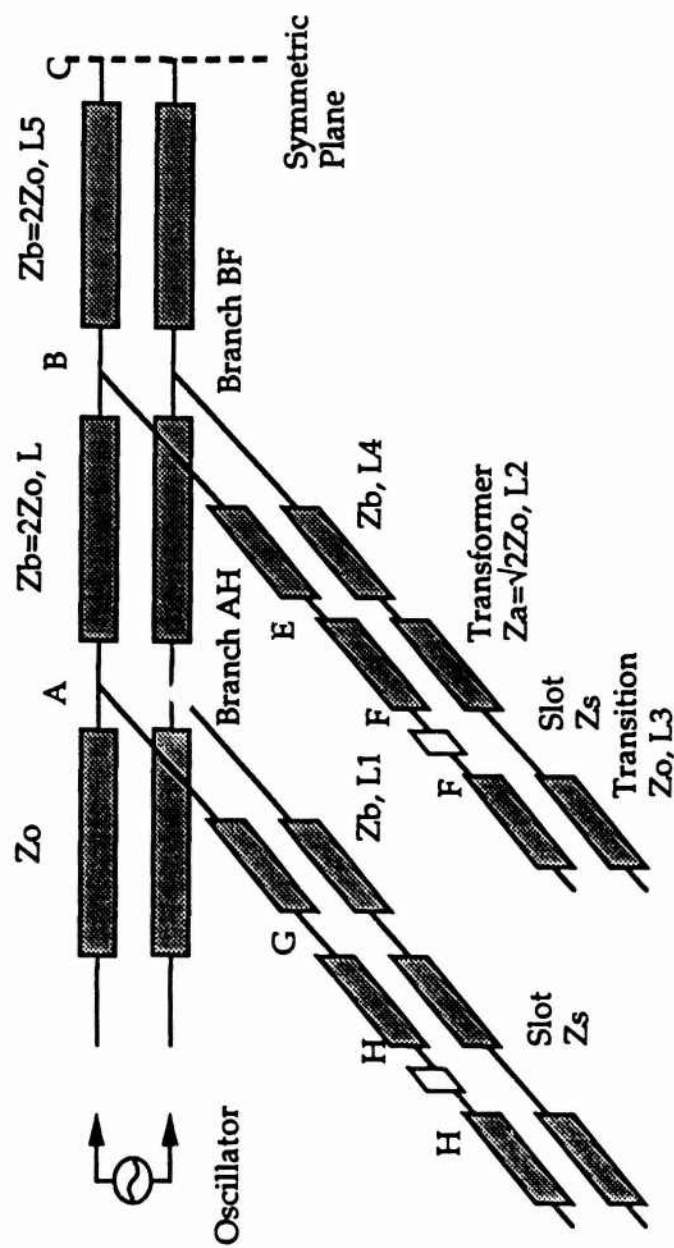


Fig. 4.4 Transmission Line Model of Passive Part of Reduced 2x2 Array

the maximum field (open circuit) and the minimum field (short circuit), when two adjacent oscillator outputs are in-phase and anti-phase, respectively. We can calculate the input impedance at A looking into the passive circuit from an FET. In each branch AH or BF shown in Fig. 4.4, the slot radiator provides a series impedance Z_s to the circuit. Thus, we can obtain the following ABCD matrix equation for the branch AH,

$$\begin{pmatrix} v_A \\ i_A \end{pmatrix} = \begin{bmatrix} A & B \\ C & D \end{bmatrix} \begin{pmatrix} v_F \\ -i_F \end{pmatrix} \quad (4.1)$$

where

$$v_i = \frac{V_i}{\sqrt{Z_0}}, \quad i_i = \sqrt{Z_0} I_i \quad i=A \text{ or } F$$

$$A = \cos \beta L_1 \cos \beta L_2 - \frac{1}{Z_a} \sin \beta L_1 \sin \beta L_2$$

$$B = Z_s^n \left(\cos \beta L_1 \cos \beta L_2 - \frac{1}{Z_a} \sin \beta L_1 \sin \beta L_2 \right) + j \left(Z_a \cos \beta L_1 \sin \beta L_2 + Z_b \sin \beta L_1 \cos \beta L_2 \right)$$

$$C = j \left(\frac{1}{Z_a} \cos \beta L_1 \sin \beta L_2 + \frac{1}{Z_b} \sin \beta L_1 \cos \beta L_2 \right)$$

$$D = Z_s^n j \left(\frac{1}{Z_a} \cos \beta L_1 \sin \beta L_2 + \frac{1}{Z_b} \sin \beta L_1 \cos \beta L_2 \right) + \cos \beta L_1 \cos \beta L_2 - \frac{1}{Z_a} \sin \beta L_1 \sin \beta L_2$$

$$z_a = \frac{Z_a}{Z_0}, \quad z_b = \frac{Z_b}{Z_0}, \quad z_s = \frac{Z_s}{Z_0}$$

$$\frac{v_F}{-iF} = \frac{1}{j \tan \beta L_3}$$

Here, $\beta = 2\pi/\lambda$ and $L_n = \lambda_0/\lambda$. The λ_0 is the wavelength at the design frequency of 20 GHz. The v_A and i_A are defined as the normalized terminal voltage and current on the branch AH at the branching point A. Similarly, we can obtain the similar matrix equation for the branch BF by replacing L_1 with L_4 . Note that v_B and i_B are defined as the normalized terminal voltage and current on the branch BF at the branching point B. From them, we can obtain the input impedance Z_A at point A as follows,

$$\frac{1}{Z_A} = Y_A = \frac{i_A}{V_A} + \frac{1}{Z_b} \cdot \frac{Y_{mB}Z_b + j \tan \beta L}{1 + j Y_{mB}Z_b \tan \beta L} \quad (4.2)$$

$$Y_{mB} = \frac{i_B}{V_B} + Y_c$$

$$Y_c \left\{ \begin{array}{ll} = \frac{j \tan \beta L_5}{Z_b} & \text{(In-phase)} \\ = j Z_b \tan \beta L_5 & \text{(Anti-phase)} \end{array} \right\}$$

where $L_1 = L_2 = L_3 = \lambda_0/4$, $L_4 = L_5 = 3\lambda_0/4 - L$, $L = 0.32\lambda_0$

Fig. 4.5 shows the input impedance characteristic for the passive part of this quasi-optical array. From Fig. 4.5, it is found that both the in-phase and anti-phase resistances are very close, when L_n is larger than 0.95. However, the in-phase reactance is very close to zero when L_n is smaller than 1.0, while the anti-phase reactance is relatively high. Therefore, if the active part of the array can be described as the series resistance and reactance, only the in-phase mode can grow once the oscillation starts. Meanwhile, the anti-phase mode is suppressed because the oscillator sees a high reactance.

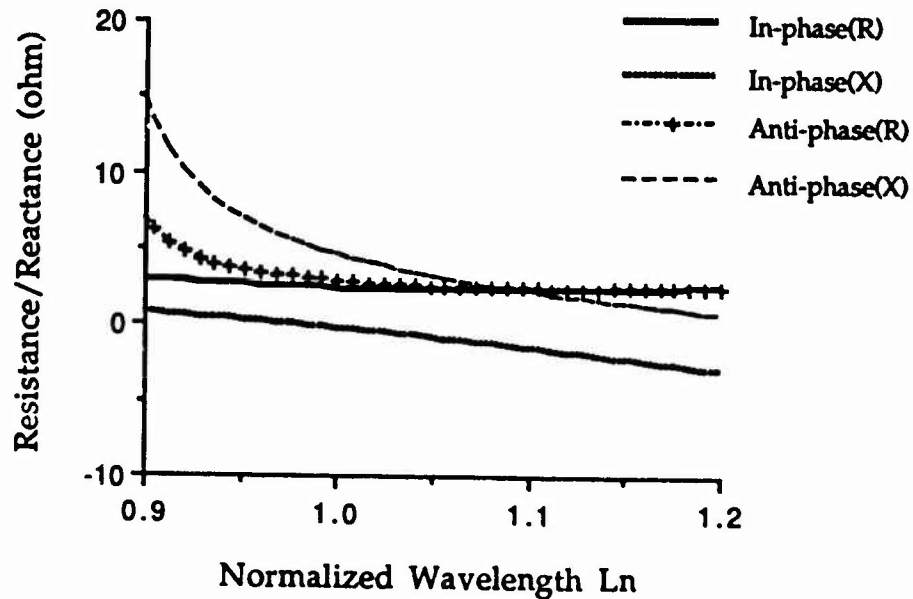
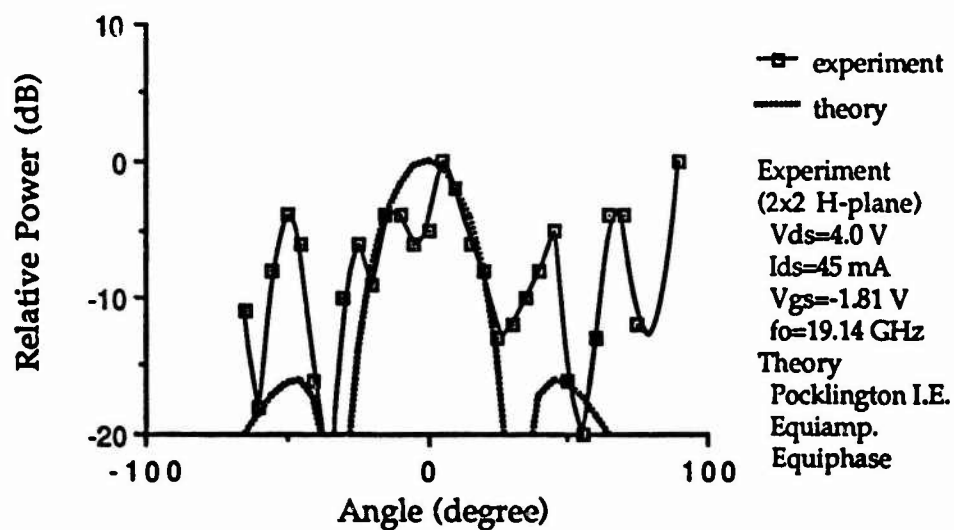


Fig. 4.5 Input Impedance of Passive Part of Reduced 2x2 Array

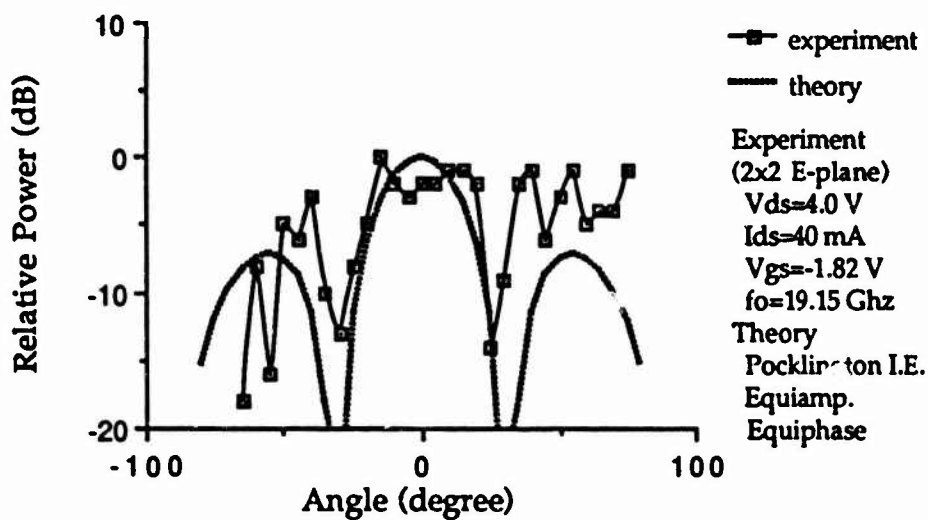
4.2.3 Experimental Results

The circuit was fabricated on the Duroid 5870 using the NE32484 packaged pseudomorphic HEMT. For V_{ds} , making use of the coupling line, only one bias network was required. The maximum operation frequency of 19.5 GHz was observed $V_{ds}=4.0$ V and $V_{gs}=-1.8$ V and the tuning range obtained by changing the applied DC voltages was 121 MHz. The ERP was estimated 25 dBm. The difference between the design frequency and the operating frequency may be due to the interaction of the two oscillators, such as load pulling.

Radiation patterns in the H-plane and the E-plane are shown in Fig. 4.6. In both cases, it is easily seen that the radiation patterns are sum patterns with null points around $\pm 40^\circ$. The null location can be found from an array factor with the array distance $0.7\lambda_0$. The theoretical patterns were compared with the experimental results in Fig. 4.6. In the calculation, the equi-amplitude and equi-phase source is assumed to excite the slots. Agreement is good around the main beams. A grating lobe in the E-plane was observed in Fig. 4.6. This is because the array factor is dominant in the E-plane. In the endfire direction, the agreement between the theory and the experiment is not good. This may result from undesired modes. Due to the two oscillator structure with a relatively low Q , these undesired modes were not suppressed effectively. Another possibility of the high lobe is due to defects of the experimental set-up at higher frequencies.



(a) Comparison of Radiation Pattern in H-Plane



(b) Comparison of Radiation Pattern in E plane

Fig. 4.6 Radiation Patterns of 2x2 Array

4.3 16-element Array

4.3.1 Configuration

Based on the single FET oscillator with four slots shown in Fig. 4.1, it is possible to design a 2 dimensional array with many FET oscillators. To demonstrate the 2-dimensional array, a circuit consisting of 4 FET oscillators with 16 slots for dual polarizations is shown in Fig. 4.7[14]. In the design of this circuit, the three design factors have also been considered; the impedance matching, the phase of the radiation signal on the slot and the signal phase of the oscillator. The impedance matching and the phase condition on the slots have already been explained in 4.1.1. Here, let us consider the third factor.

The distance between the two centers of the slots has already been described in 4.1.1. Since this length becomes the criteria for the physical separation, the physical length between two centers of the oscillators has also been fixed. Therefore, the length of coupling lines should be determined to meet the requirement for the geometrical dimension as well as the electrical length. If the argument of Γ_{in} of the oscillator is π , the length of the coupling lines between any two branching points should be $(2n-1)\lambda/2$ (where n is an integer). In addition, these coupling lines should be placed so as not to disturb radiation from the slots on the backside of the circuit substrate. For these purposes, the coupling lines connecting each unit oscillator such as A-B-C are not straight.

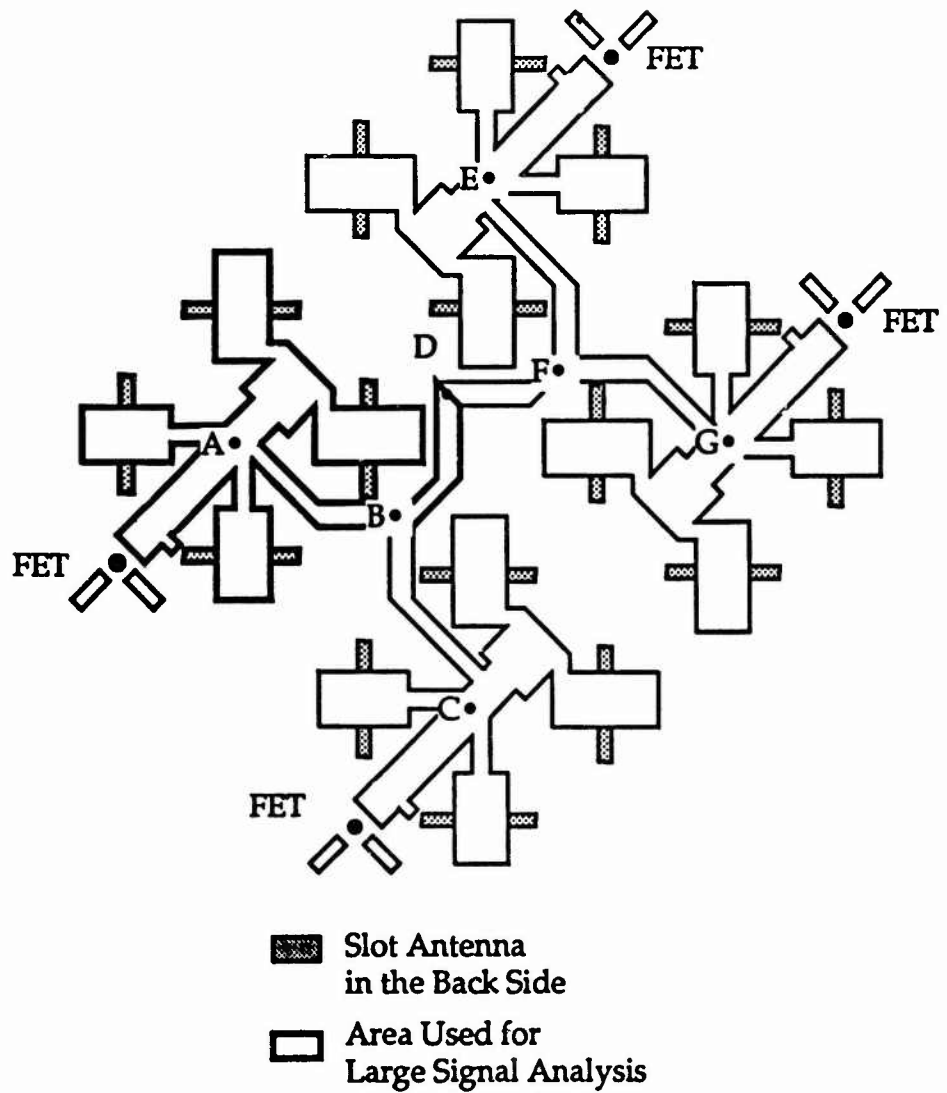


Fig. 4.7 Configuration of 16-element Dual Polarized Array with 4 Oscillators

4.3.2 Experimental Results

Fig. 4.8 shows the measured antenna patterns of the 16-element array. The operating frequency was 7.8 GHz with $V_{ds}=4.23$ V and $V_{gs}=-0.8$ V. For V_{ds} , only one DC power supply was required, making use of the strong coupling line. The FET and the substrate used here were ATF 13284 and Duroid 5870, respectively. The oscillation frequency is significantly different from the one for Fig. 4.1. Perhaps, this is due to impedance mismatch. This mismatch produced interaction of the oscillators such as load pulling. As a result, this interaction may cause a lower operating frequency. In this case, the distance of the centers of two slots became almost one wavelength of the operating frequency.

The antenna patterns were measured in two ways as described in Fig. 4.8. The measuring plane is fixed in the horizontal plane. In the case A, polarization is vertical. The 8 slots out of 16 slots aligned in the direction along the slot length can contribute to the antenna pattern. A pattern mainly resulting from the 3-element slot array in the H-plane was expected. This explains the obtained pattern for the case A in Fig. 4.8. In the case B, the measured polarization is horizontal. Since the 8 slots in the E-plane shown in Fig. 4.8 can contribute to the measurement, the antenna pattern due to an array factor determined mainly by the center 4 slots rather than an element factor, was expected. In the case B of Fig. 4.8, this tendency can be seen and a grating lobe was observed. As described in 4.1.1, this grating lobe problem can be solved by using a high dielectric constant substrate.

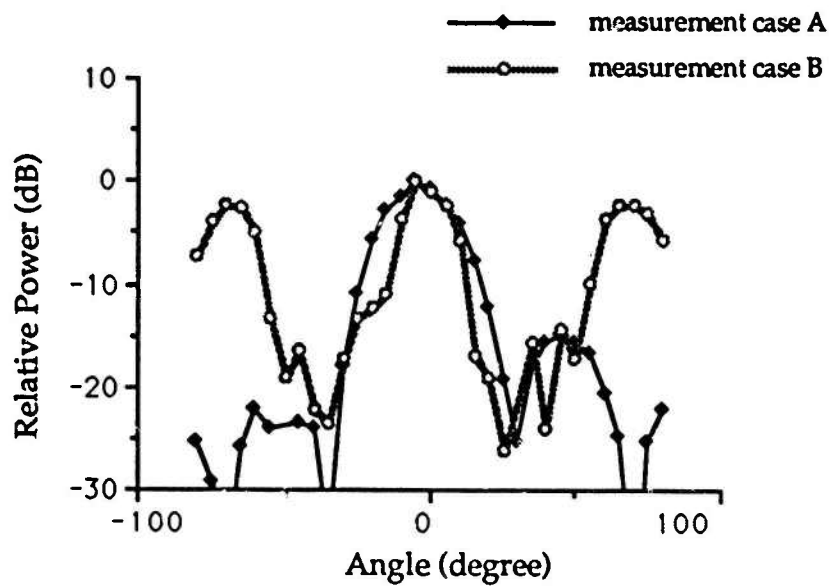
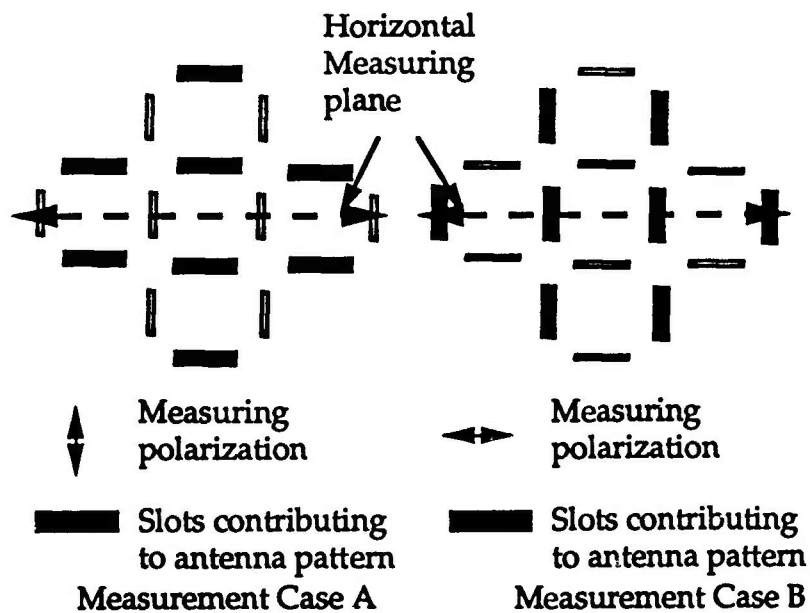


Fig. 4.8 Antenna Pattern of 16-element Array

4.3.3 Analysis of 16-element Array

In this section, let us analyze the 16-element array shown in Fig. 4.7 by using the large signal analysis. Since the experimental operating frequency was 7.8 GHz, the electrical length of A-B-C and E-F-G became 1.5λ . When the argument of Γ_{in} of each oscillator is π at 7.8 GHz, the field maximum points are at B and F. In addition, since B-D-F is 1λ , A-B-D-F-E becomes 2.5λ and then D is the field maximum point. Therefore, at 7.8 GHz, all radiation signal from the slots are in-phase. Due to the circuit configuration, the points of B, D and F are center points between the oscillators. According to the discussion in 3.2, by replacing the coupling line into the appropriate stub, the circuit is modeled into a single unit cell. In this circuit case, A-B-D is suited for the stub, since the point D is the center point for all oscillators. The model used for the large signal analysis is the same as shown in Fig. 3.6. Using this model, the array was analyzed. The result is shown in Fig. 4.9. In this case, only the in-phase mode was taken into account. From this analysis, a steady state operating frequency of 8.2 GHz for the in-phase mode can be evaluated. The agreement between this frequency and the experimental data is good. Therefore, using the technique described here, it is possible to realize a 2-dimensional quasi-optical power combining array with a large number of FETs.

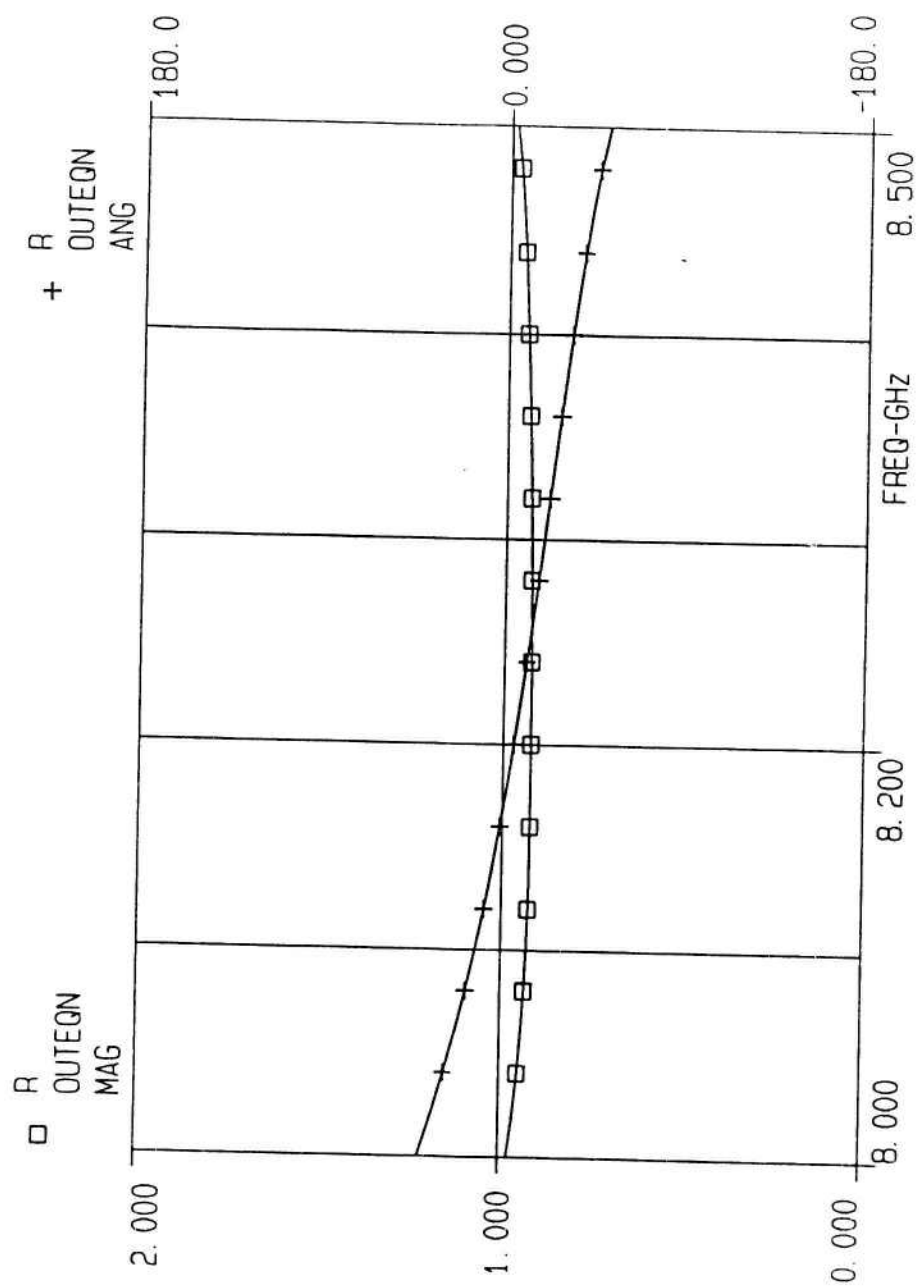


Fig. 4.9 Variation of R for Reduced 16-element Array

Part 2 : Variation of Quasi-Optical Technique

Chapter V

FET Passive Component

5.1 Reactive FET Design

5.1.1 Design Criteria

If we can make an FET have only a reactive output as a one-port circuit, we can make use of it as an additional reactance to the microstrip line (parallel insertion). Using a similar design procedure to the FET oscillator or amplifier, an electronically tunable stub can be obtained. The variation of the reactance is a result of the change in the Schottky barrier as the gate bias is changed. As described above, since the reactive FET has only one port, its input impedance should be adjusted so that an adaptable reactance value may be supplied at an appropriate place of the circuit and at the target frequency[21]. For instance, in an X-band circuit, the input impedance of the reactive FET can be designed to be $-25j \Omega$ near the design frequency of 10 GHz so that it can be placed at a low impedance place[44]. This reactance value corresponds to 0.6 pF at 10 GHz and to the typical gate-to-source capacitance of the MESFET at X-band. A structure suitable for the layered active integrated antenna is shown in Fig. 5.1. A $\lambda/4$ transition is added at the top of the circuit to electromagnetically couple with the slot radiator and to enhance the reactance. Since the FET is used, it is better to check the stability of this circuit. For this purpose, Z_{in} or Γ_{in} should be investigated. Fig. 5.2

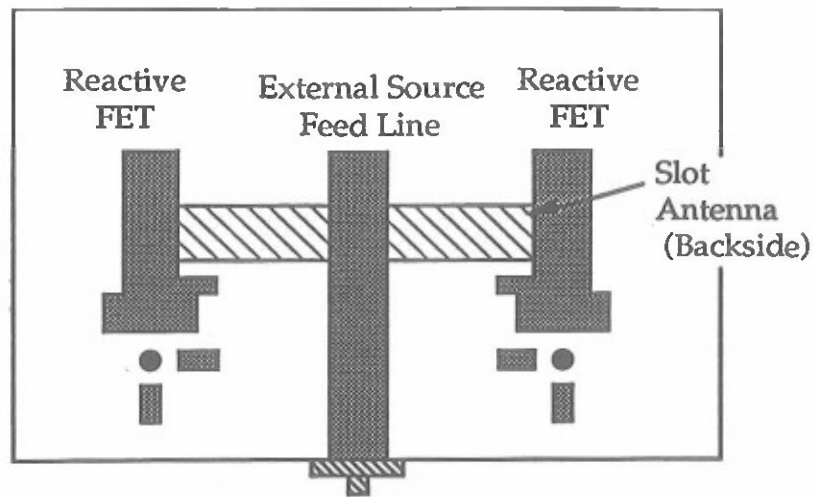


Fig. 5.1 Configuration of Reactive FET

shows simulation results of the magnitude of Γ_{in} . Under the condition of a non-zero reactance at the source terminal, there are areas where Γ_{in} is greater than one. This means the circuit is not unconditionally stable. However, a circuit with the zero reactance at the source terminal is relatively stable.

5.1.2 Experimental Results of Reactive FET

Based on the argument in the previous section, a reactive FET circuit designed at 10 GHz with $-25j \Omega$ was made and investigated. The circuit was very stable, since there is no reactive element at the source terminal. Fig. 5.3 shows the experimental data for the maximum tuning range of the argument of Γ_{in} at 6.8 GHz. The FET used is NE72084 and the substrate used is Duroid 5870. From these results, the change of the electrical length as a tuning stub by adjusting V_{gs} (0~1.76 V) was 12.6° . In this case, the change of the

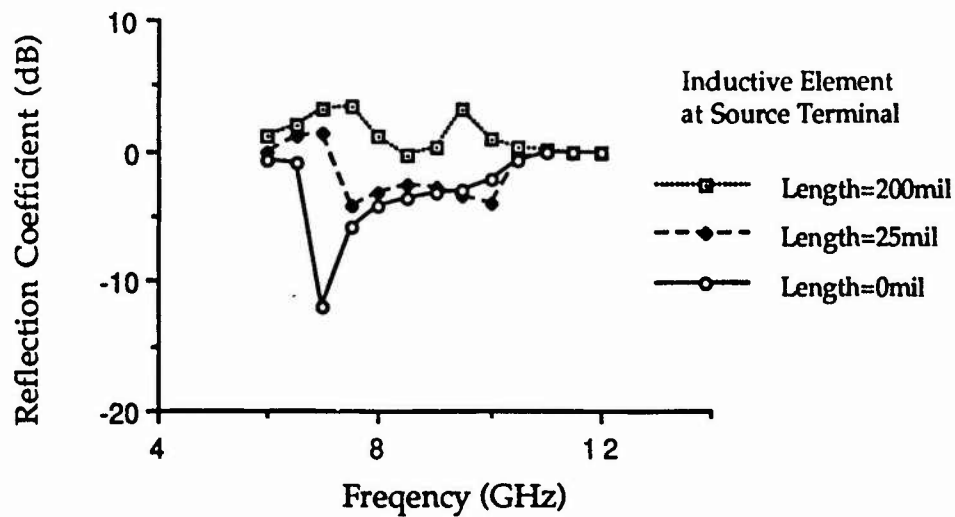


Fig. 5.2 Frequency Characteristics of Reflection Coefficient for Reactive FET with/without Inductive Element at Source Terminal

magnitude of Γ_{in} was 0.12 near 0.85. The zero bias for V_{ds} seems to result in the small tuning range. The experimental operating frequency is different from that of the design frequency. When the circuit was designed, the commercially available small signal S-parameters were used which were measured at $V_{ds}=3.0$ V and $I_{ds}=10$ mA. This means that the operating voltage is very different. Therefore, the intrinsic reactance (capacitance) values of the FET are also different. This results in the different operating frequency. To predict the operating frequency accurately, nonlinear analysis should be carried out.

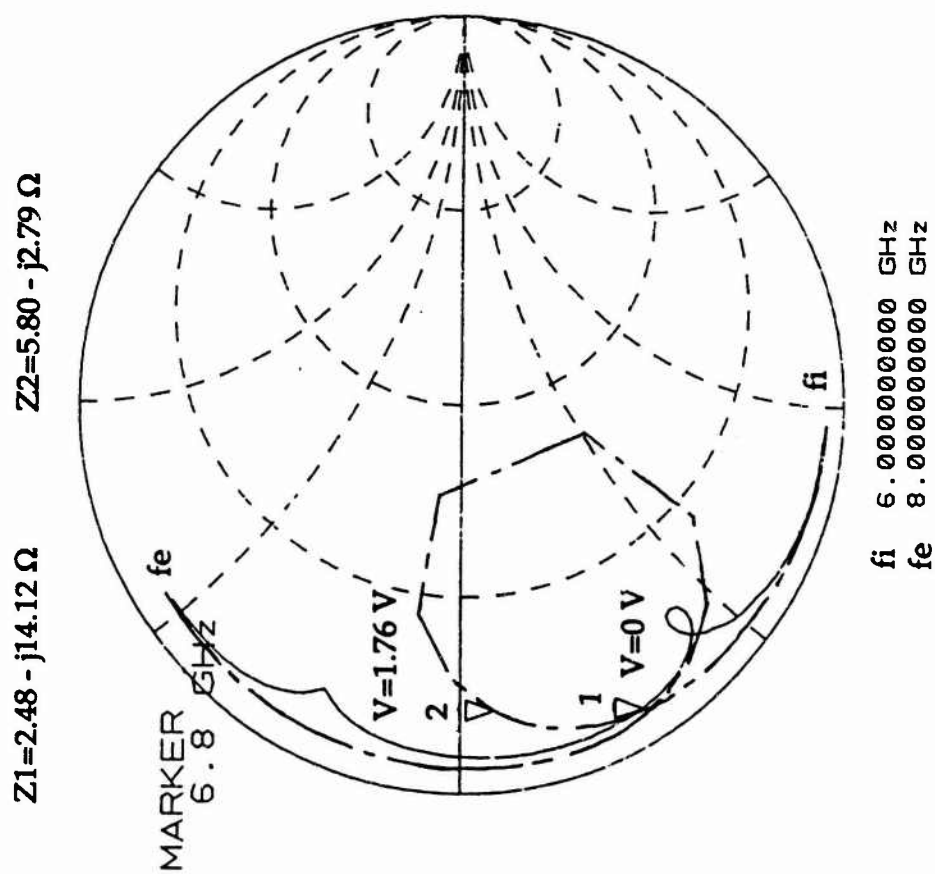


Fig. 5.3 Experimental Tuning Range of Reactive FET

5.2 Wide-band Slot Antenna and Active Integrated Antenna with Reactive FET

5.2.1 Operation Concept

Once the length of a slot antenna is determined, it is not easy to keep the electrical length constant when the operating frequency is changed. However, this can be achieved by adding electronically controlled reactive elements[21]. These reactive circuits made of MESFETs are placed near both ends of the slot where the impedance is very small. Their position is determined so as not to change the field distribution on the slot antenna significantly. This is because, if the field distribution on the slot is changed, the center feed line does not match to 50Ω . Fig.5.4 shows an expected field distribution of a 1λ slot antenna. According to Fig.5.4, the center and both

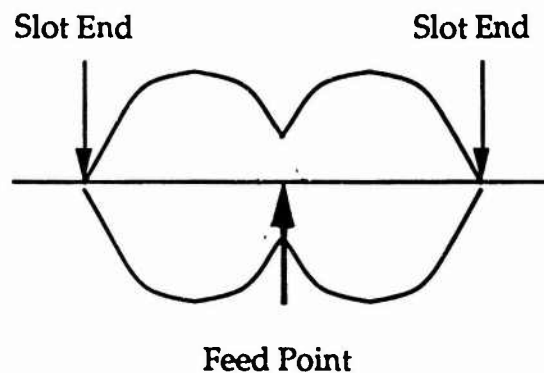


Fig. 5.4 Field Distribution on 1λ Slot Antenna

ends of the slot have low impedances. Since the reactive FET circuit has a small impedance value of $-25j\Omega$ at 10 GHz, we should place the device at the low impedance points. In this slot antenna case, the very end of the slot has 0

Ω. Therefore, the crossover point between the slot and the microstrip feed line of the reactive FET circuit is placed slightly inside the slot. In our circuit case, the distance between the end of the slot and the center of the feed line of the reactive FET circuit is about $0.02\lambda_s$. Fig. 5.5 shows the operation concept of the reactive FET to electronically control the electrical length of the slot radiator. Further, based on the operation concept described above, the external source feed line was replaced by a built-in negative resistance

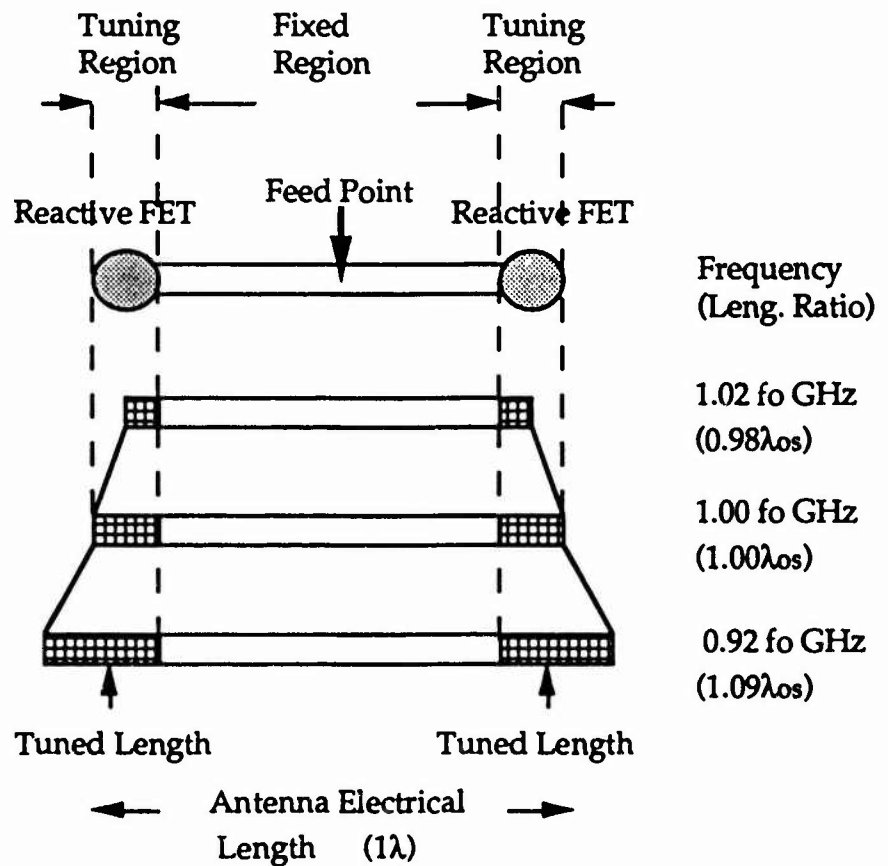


Fig. 5.5 Operation Concept of Reactive FET

oscillator to construct the active integrated antenna. A configuration of an active integrated antenna with the reactive FET's is shown in Fig. 5.6.

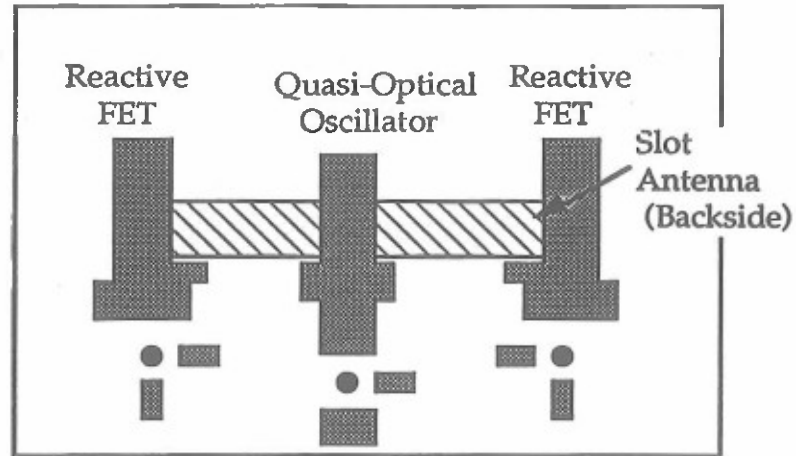


Fig. 5.6 Active Integrated Antenna with Reactive FET

5.2.2 Experimental Results

From the measurement of S_{11} , the matching status between the feed and the slot was investigated. The FET used is ATF26884 and the substrate used is Duroid 5870. Fig. 5.7 shows S_{11} measurement results of the wide-band slot antenna. The shift of the matching point was observed. Fig. 5.8 shows the measured antenna patterns of this circuit. This figure shows that there is no significant change on these measured antenna patterns. This electronically tunable slot exhibited a 10 % bandwidth at the center frequency of 9.7 GHz. For the active integrated antenna with the reactive FET's, the tuning range of 33 MHz was obtained. The small tuning range may result

from the narrow tuning capability of the FET oscillator. With respect to the antenna patterns of the active integrated antenna, no significant change in the antenna patterns was found because of the small tuning range. In these circuits, the reactive FET has the reactive element on the source terminal. As a result, the operation is not quite stable when V_{ds} increases. However, under the small V_{ds} , it was possible to obtain the wide tuning range. As described in 5.1.1, no reactance element is required at the source terminal to obtain more stable operation.

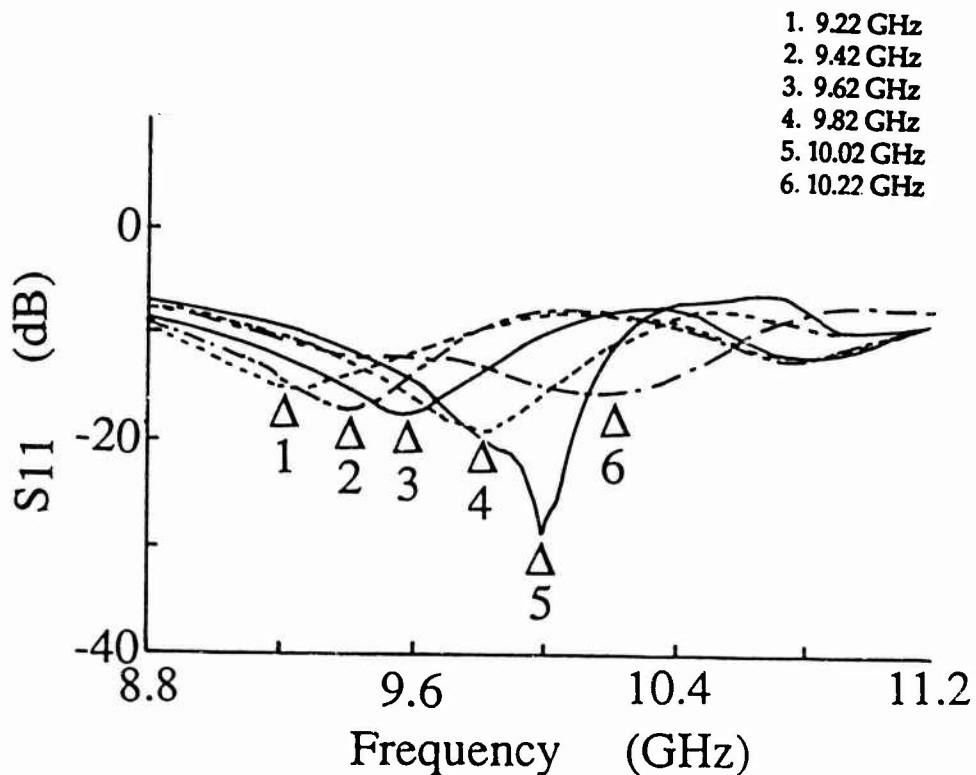


Fig. 5.7 S_{11} of Wide-band Slot Antenna

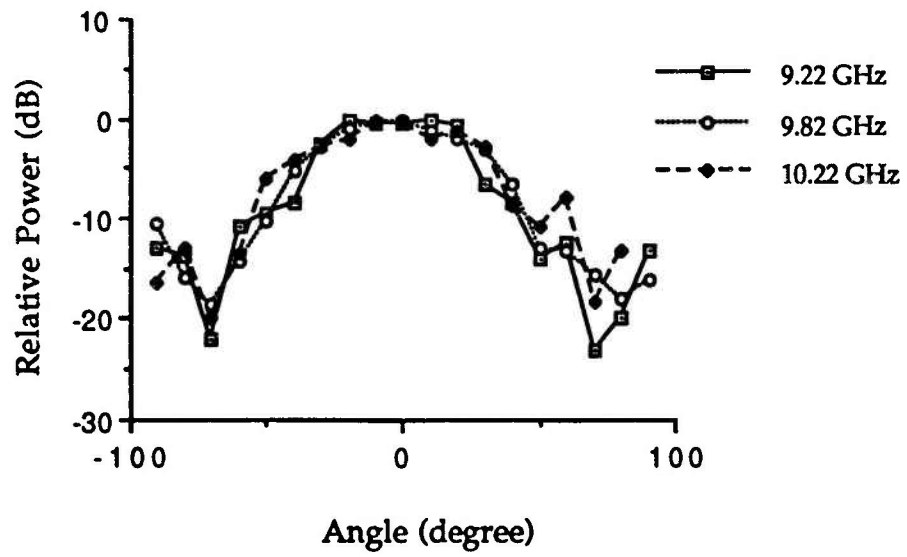


Fig. 5.8 Antenna Patterns of Wide-band Slot Antenna

Chapter VI

Optical Control of Active Integrated Antenna

6.1 Photo Detection

6.1.1 Photodetector

There are many mechanisms arising in optical illumination of FET's. They are based on the production of electron-hole pairs in the semiconductor material if the photon energy absorbed is equal or greater than the bandgap energy of the semiconductors. Among these mechanisms, the photovoltaic effect and the photoconductive effect are very important phenomena for the device application[16].

In order to understand the mechanism of the photovoltaic effect[45], let us consider a Schottky-barrier diode as shown in Fig. 6.1. In this case, the absorption of the photon energy take place in the depletion region to create electron-hole pairs. The photogenerated excess electrons diffuse toward the n^+ substrate region whose edge has an ohmic contact, while the excess holes were swept toward the Schottky-barrier contact. The presence of change of the carrier distribution results in lowering the Schottky-barrier potential. This mechanism is understood as being equivalent of the forward bias between the two contacts and is called the photovoltaic effect. In addition, this equivalent bias is often referred to as a photovoltage.

The photoconductive effect is a more straightforward phenomenon since it is a bulk type effect[46]. As shown in Fig. 6.2, let us consider a simple slab of semiconductor with ohmic contacts affixed to opposite ends. When

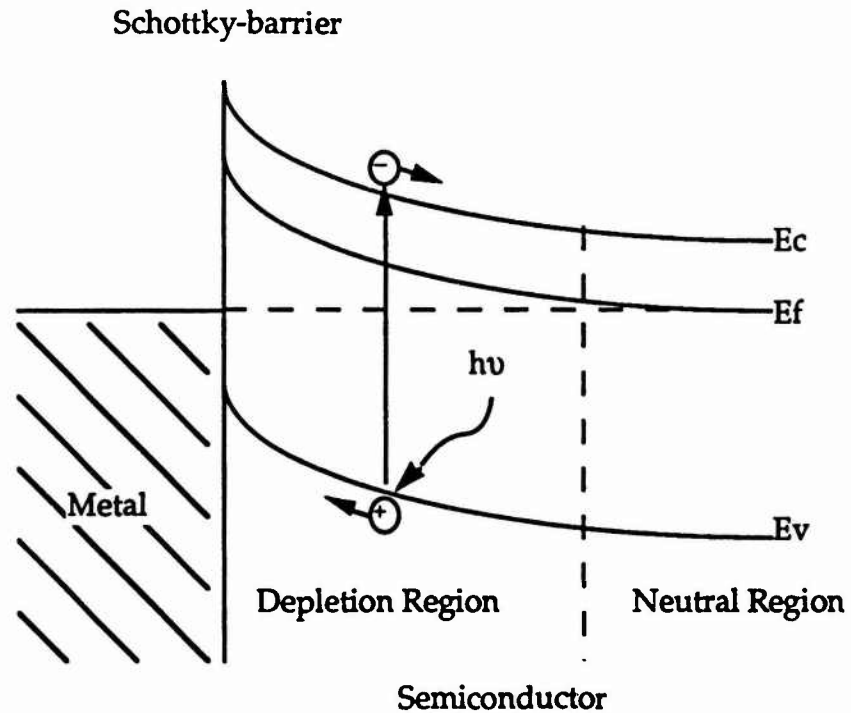


Fig. 6.1 Photovoltaic Effect of Schottky-barrier Diode

the absorbed photon energy is equal or greater than the bandgap energy of the semiconductor, the electron-hole pairs are generated. These carrier can contribute to a current flow. As a result, the conductivity of the semiconductor increases by illumination.

6.1.2 Illumination Effect on FET

In order to investigate optical control of the active integrated antenna, two types of FET's are selected; a MESFET and a high electron mobility transistor (HEMT). Both FET's have the Schottky-barrier contact at the gate. Therefore, the photovoltaic effect described above is expected in both cases.

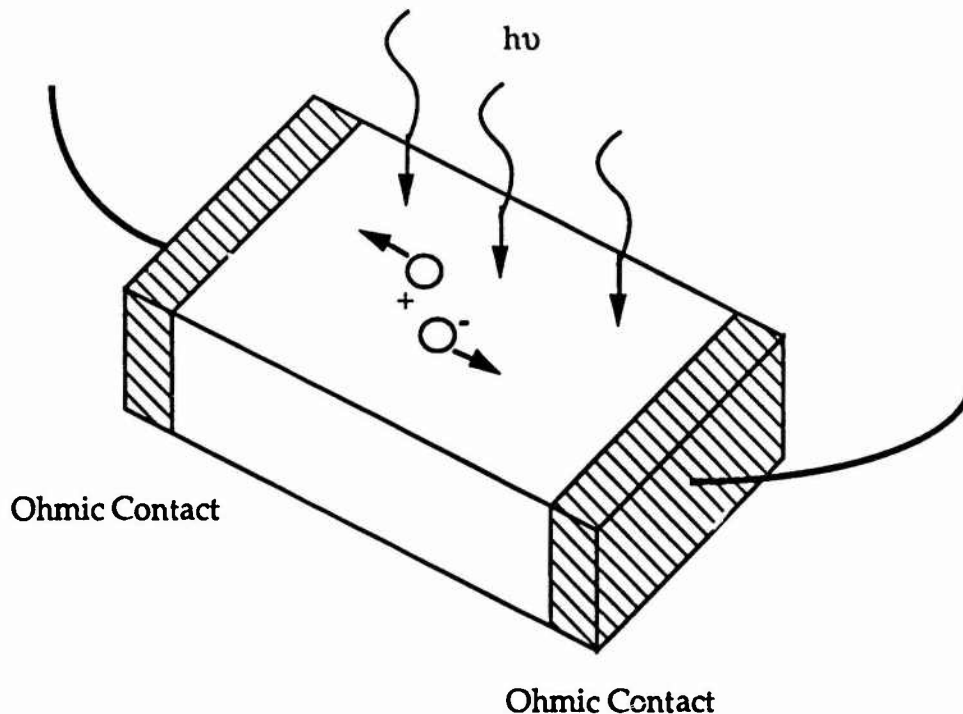
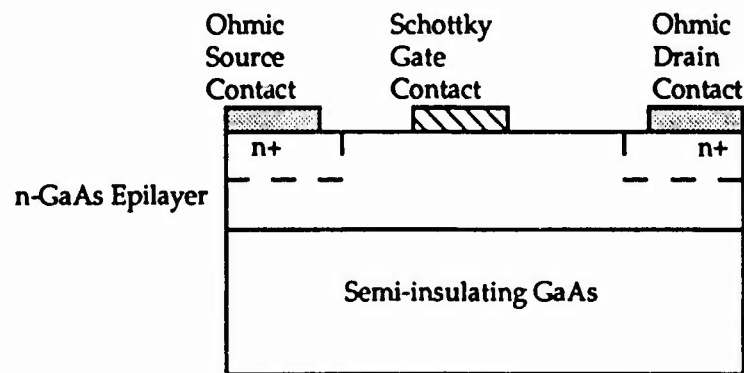


Fig. 6.2 Photoconductivity of Semiconductor Slab

On the other hand, the difference between them is that the latter has a heterojunction structure which is promising for higher operating frequencies. According to the previous section, the photogenerated carrier due to the photoconductive effect can contribute to increase of the majority carrier in the FET resulting in the increase of conductivity. Since a typical cut-off frequency of a MESFET is lower than that of a HEMT, an optically controlled quasi-optical power combining array using a HEMT can be expected to be realized at very high frequencies. Another difference is that of the tuning range due to the wider optical absorption area of the MESFET. This creates a larger change

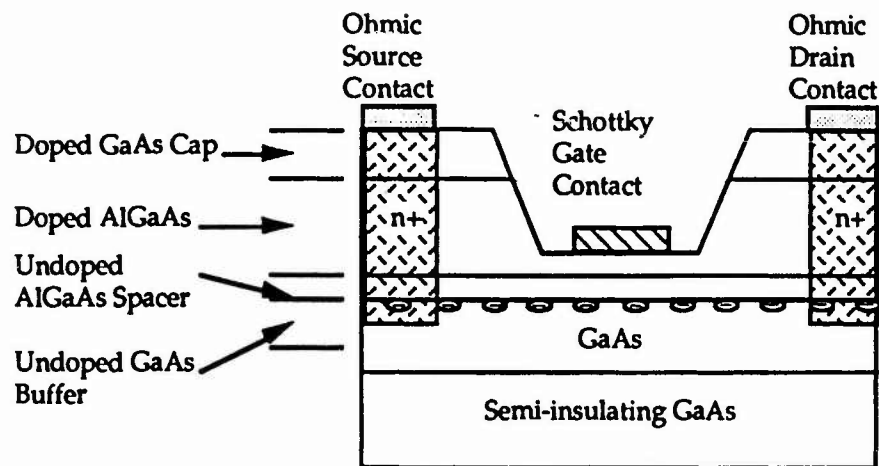
in the circuit parameters such as a gate-source capacitance and drain-source resistance. As a result, a wide tuning range can be expected.

Fig. 6.3 illustrates the cross sections of three FET's; a GaAs MESFET, an AlGaAs/GaAs HEMT and an AlGaAs/InGaAs pseudomorphic HEMT. Among them, the second and the third are categorized as the HEMT. Fig. 6.4 shows energy band diagrams for the MESFET and the HEMT. As described in the previous section, the two main effects take place by illumination; the photovoltaic effect and the photoconductive effect. In the case of the illuminated FET, the photogenerated electron-hole pairs in the depletion region due to the photovoltaic effect are separated by the built-in electric field which sweeps the electrons to the active channel layer while the holes flow in the opposite direction to increase the gate current. This phenomenon is equivalent to the small forward bias[17]. Meanwhile, photogenerated carriers in the active layer due to the photoconductive effect are swept by the electric

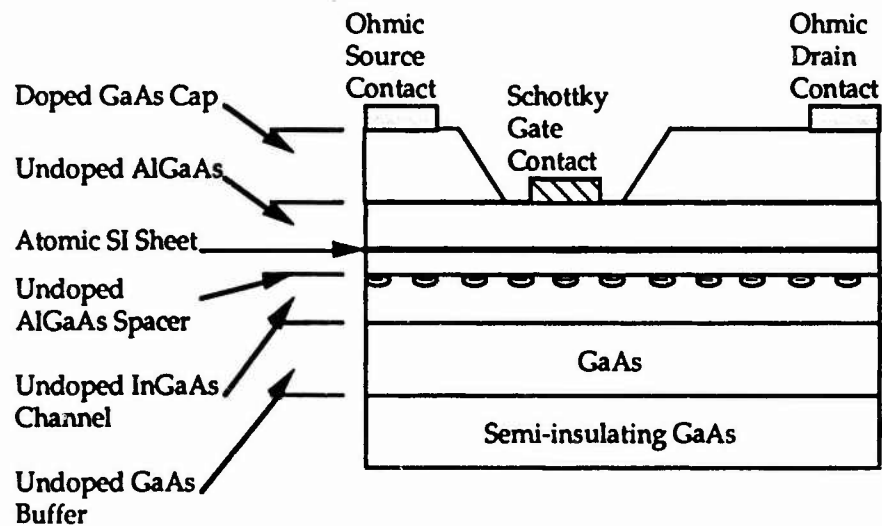


(a) MESFET

Fig. 6.3 Cross Section of FET's

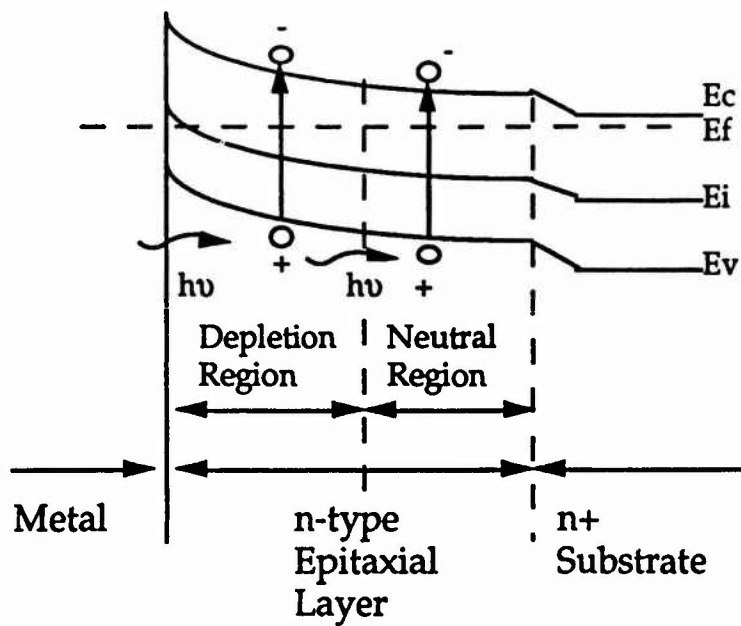


(b) AlGaAs / GaAs HEMT

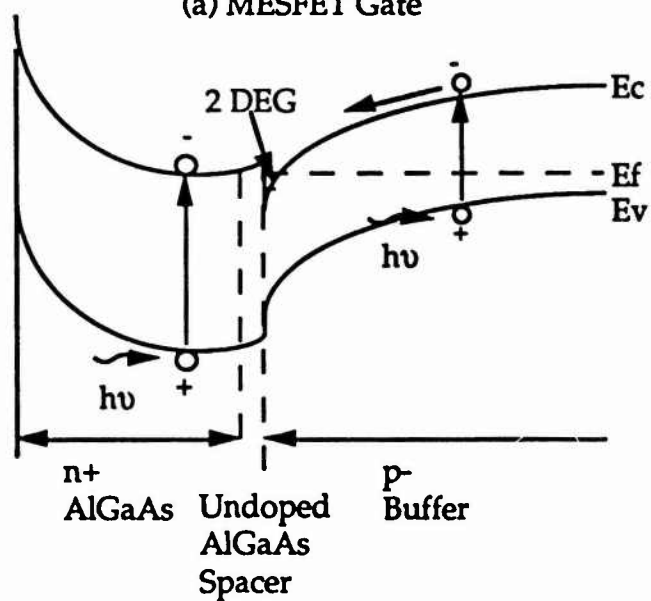


(c) AlGaAs / InGaAs Pseudomorphic HEMT

Fig. 6.3 Cross Section of FET's



(a) MESFET Gate



(b) HEMT Gate

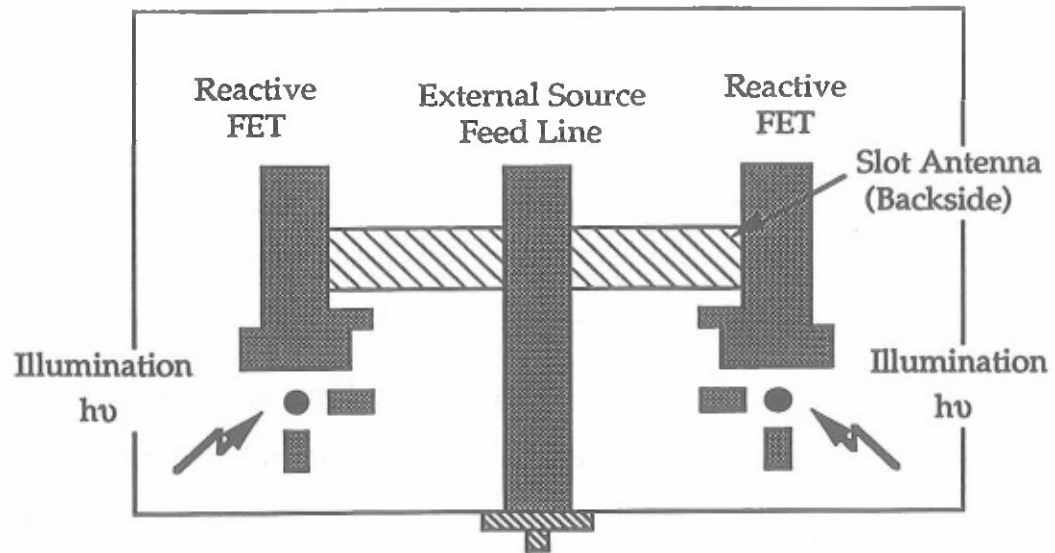
Fig. 6.4 Energy Band Diagram at Gate of MESFET and HEMT

field associated with the band bending and then these carriers can contribute to the drain current. As a result, the drain conductance increases. Generally speaking, the photoconductive effect has high responsibility. Therefore, this phenomenon is made use of for operation at millimeter-wave frequencies. If only the photoconductive effect is desired, the photon energy of the optical source should be selected so as to be greater than the bandgap energy of the active layer but to be smaller than that of the depletion layer. This operation method is important for applications[18],[19].

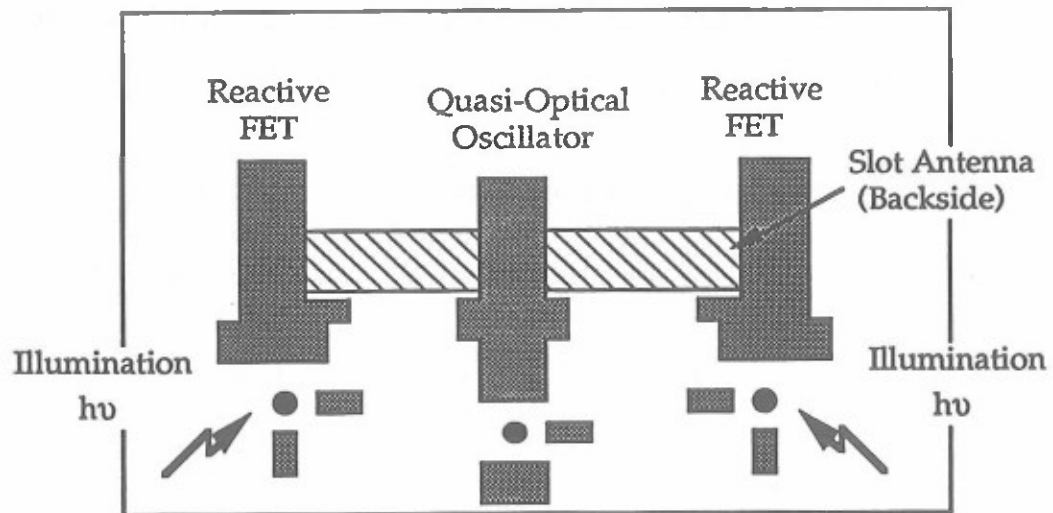
6.2 Optically Controlled Reactive FET

6.2.1 Configuration

To demonstrate the optically controlled reactive FET adaptable to the planar active integrated antenna, two circuits were designed at 10 GHz[23]. Their structures (Circuit R-I and R-II which is the same as Fig. 5.8) are shown in Fig. 6.5. The center microstrip feed line is connected to the external microwave source through an OSM connector in the case of Circuit R-I, while the built-in negative resistance oscillator made of a MESFET is used to construct the quasi-optical oscillator in the case of Circuit R-II. The impedance of the oscillator is designed to have a negative resistance of $-50\ \Omega$. Two reactive MESFET circuits made by the microstrip line are electromagnetically coupled to the slot near the edge of the slot. The center of the feed line of the reactive FET is located at the inside point of $0.02\lambda_s$ from the edge of the slot as described before.



(a) Circuit R-I



(b) Circuit R-II

Fig. 6.5 Optical Control of Reactive FET

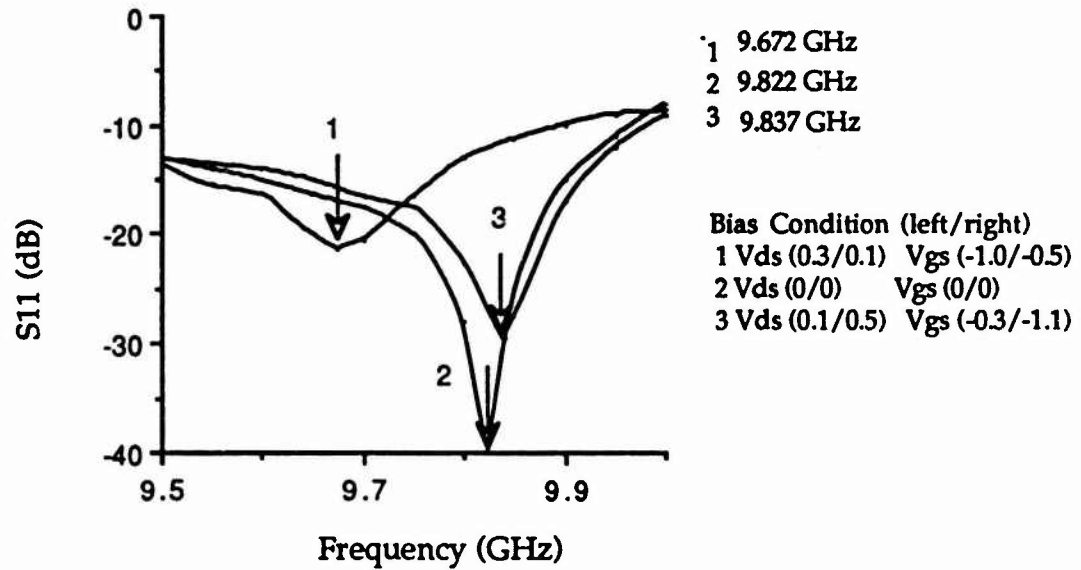
6.2.2 Experimental Results

The FET used for the reactive MESFET is NE 72084 and the substrate used here is Duroid 5870. In both cases, the caps of the two reactive FETs were removed to allow illumination by optical sources. Using Circuit R-I, a shift of the matching frequency through the measurement of S_{11} was observed as shown in Fig. 6.6. The electrical tuning range in Circuit R-I of 150.5 MHz was obtained by changing V_{gs} only. For the investigation of the optical tuning range, the laser ($\lambda=780$ nm) and the fiber illuminator (a quartz halogen lamp with an optical fiber) were used as optical sources. An appropriate bias voltage was selected to obtain the maximum sensitivity for illumination. From the measurement of S_{11} using Circuit R-I, an optical tuning range was found to be 56 MHz by direct illumination of a laser and 110 MHz by the fiber illuminator shown in Fig. 6.6. Using Circuit R-II, an

**Table II : Tuning Range Comparison
of Active Integrated Antenna
with Optically Controlled Reactive FET**

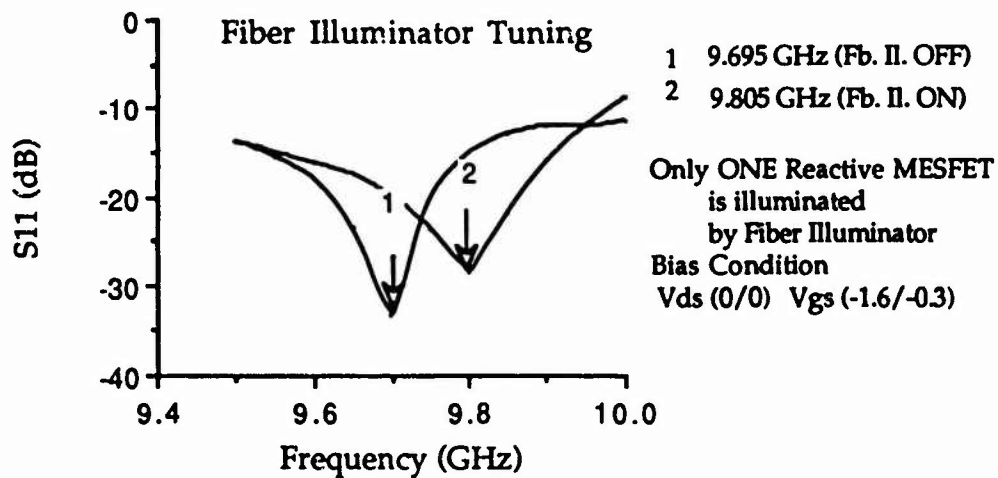
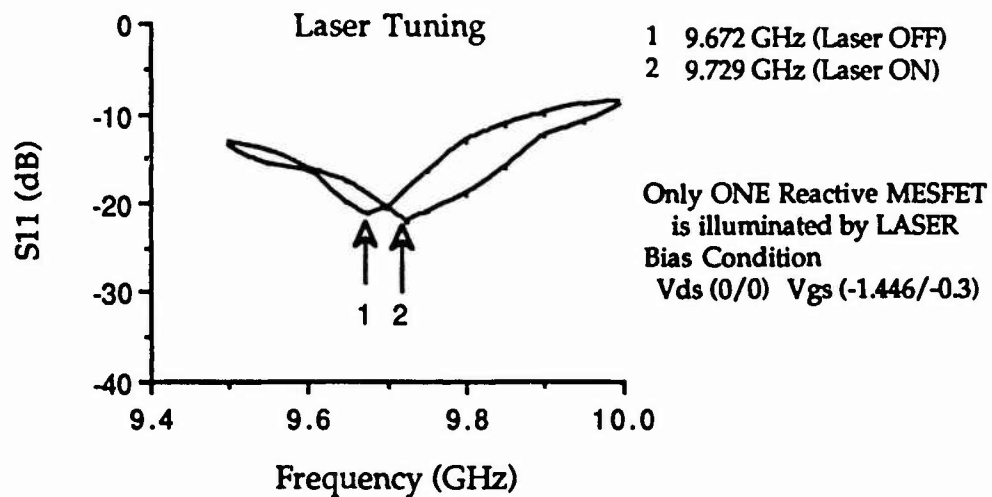
Circuit	Operating Frequency ($V_{ds}=4.0$ V)	Electronic	Optical	
			Laser (780 nm)	Halogen Lamp
R-I	9.82 GHz	155 MHz	56 MHz	110 MHz
R-II	9.64 GHz	33 MHz	5 MHz	12 MHz

optical tuning range due to the laser of 5 MHz and the tuning range due to the fiber illuminator of 12 MHz were obtained. Note that the circuit was not optimized for optical illumination. The optical as well as electrical tuning range of these circuits is summarized in Table II.



(a) Electrical Tuning

Fig. 6.6 Electrical and Optical Tuning Range



(b) Optical Tuning Range

Fig. 6.6 Electrical and Optical Tuning Range

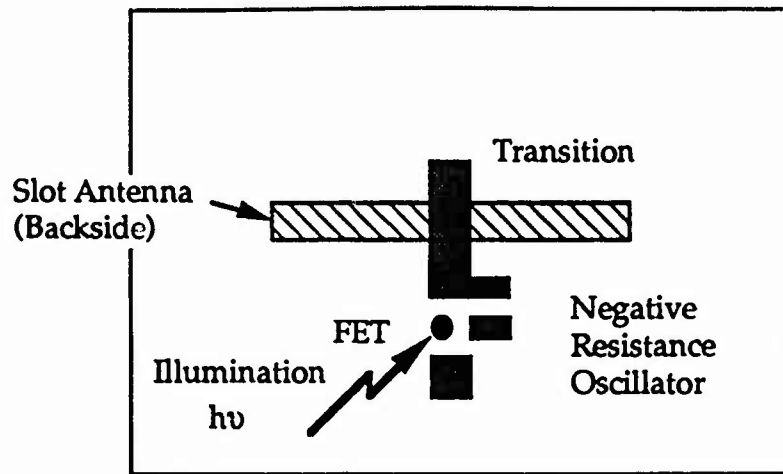
6.3 Optical Tuning Range of Active Integrated Antenna

6.3.1 Circuit Configuration

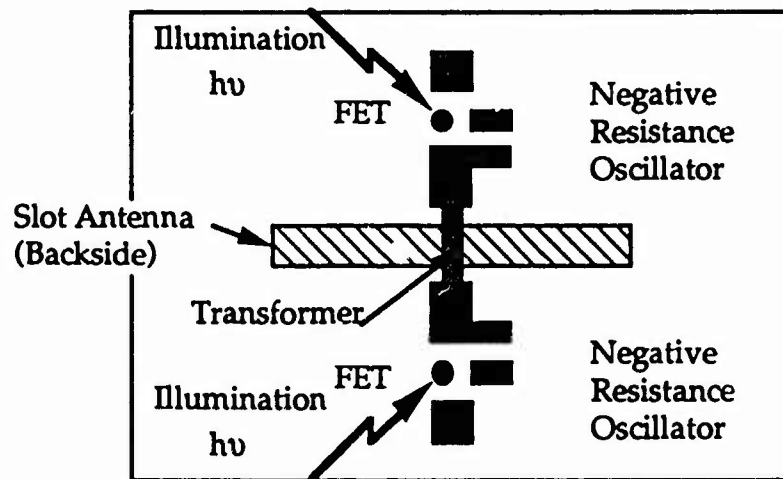
As an alternative way to optically control the active integrated antenna, direct illumination of the negative resistance FET oscillator in the planar active integrated antenna was carried out[47]. For this purpose, two types of active integrated antennas have been demonstrated. Fig. 6.7 shows their configurations as Circuit AA-I and Circuit AA-II. In both cases, the circuit is designed at 10 GHz. Circuit AA-I is a simple active integrated antenna, while Circuit AA-II is a planar active integrated antenna consisting of a double oscillator and a single slot. In Circuit AA-II, the two oscillators were connected in parallel with the slot antenna through a $\lambda/4$ transformer to match the input impedance of the slot. Through this configuration, it is expected that the radiation energy from the slot increases. Note that the tuning range in Circuit AA-II by illuminating only one MESFET oscillator is not the same as the tuning range in Circuit AA-I. This is because the input impedance seen from the slot to the oscillator circuit of Circuit AA-II is different from that of Circuit AA-I.

6.3.2 Electrical and Optical Tuning Range

The FET used was NE 72084 (MESFET) and the substrate used is Duroid 5870. In both cases, the caps of the two reactive FETs were removed for illumination with optical sources. An operating frequency of 12.5 GHz was obtained for Circuit AA-I. The electrical tuning range was 145 MHz by changing both V_{ds} and V_{gs} . By illuminating with a fiber illuminator, the



Circuit AA-I (one oscillator)



Circuit AA-II (two oscillators)

Fig. 6.7 Optically Controlled Active Integrated Antenna

optical tuning range of 50 MHz was obtained at $V_{ds}=4.0$ V and $V_{gs}=-1.7$ V. In addition, due to illumination, the received power in the broadside

direction increased by about 2.5 dB. The operation frequency of Circuit AA-II was 12.1 GHz at $V_{ds}=4.0$ V and $V_{gs}=-1.6$ V. The increase in received power in the broadside direction was 1.4 dB compared with that of Circuit AA-I. An electrical tuning range due to changing V_{ds} and V_{gs} of 250 MHz was obtained. In the case of the optical control, V_{ds} was fixed and only V_{gs} was tuned for maximizing the optical tuning range. In order to compare the difference of the amount of illumination on the MESFETs, both cases of the single-oscillator illumination and the double-oscillator illumination were investigated using Circuit AA-II. Fig. 6.8 shows their results. By cutting the length of the open circuit at the gate and adjusting V_{gs} , an operating frequency was obtained at 10.8 GHz. Under this condition, optical tuning ranges of 50 MHz in single-illumination and 63 MHz in double-illumination were obtained. Saturation may occur in the latter case. The variation of the tuning range is shown in Fig. 6.9. Apparently, an optimum voltage for the maximum sensitivity exists. Using the same method described earlier in this dissertation, the tuning range by the large signal analysis can be evaluated for Circuit AA-I[48]. Fig. 6.10 indicates the simulation result of the variation of R (V_{fb}/V_{in}). Table III indicates these tuning ranges. The agreement is good. Of course, when only the photovoltaic effect takes place, we can estimate the tuning range by including the illumination effect in the change of gate voltage. However, in this case both photo current effects occur. Therefore, this consideration should be carried out under change of nonlinear FET parameters using the large signal analysis.

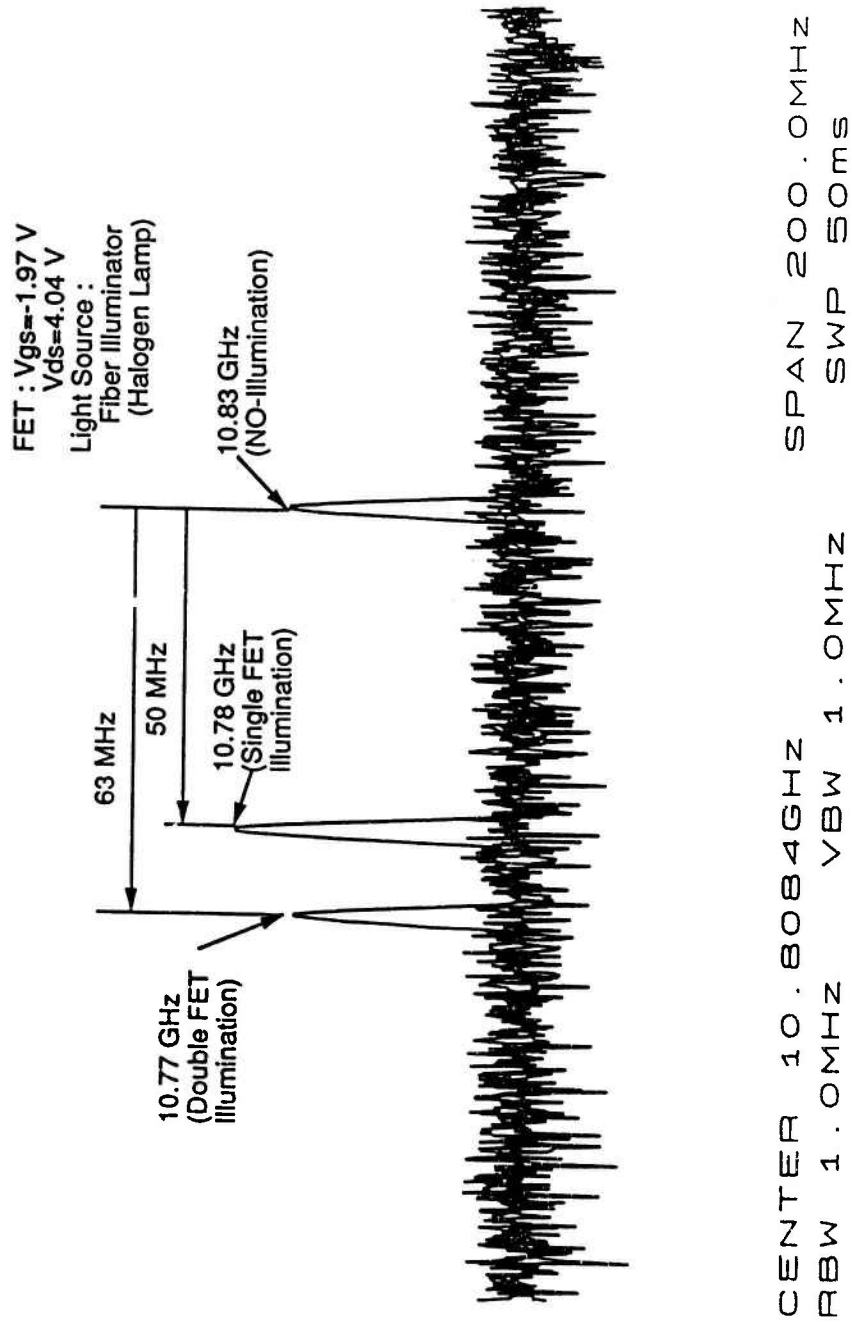


**Fig. 6.8 Operation Spectrum Shift
 of Optically Controlled Active Integrated Antenna**

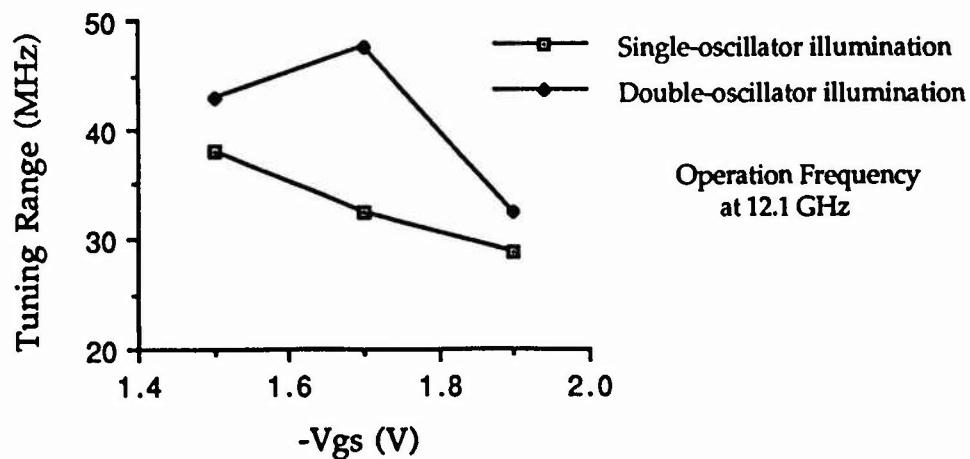


Fig. 6.9 Gate Voltage Dependence of Optical Tuning Range

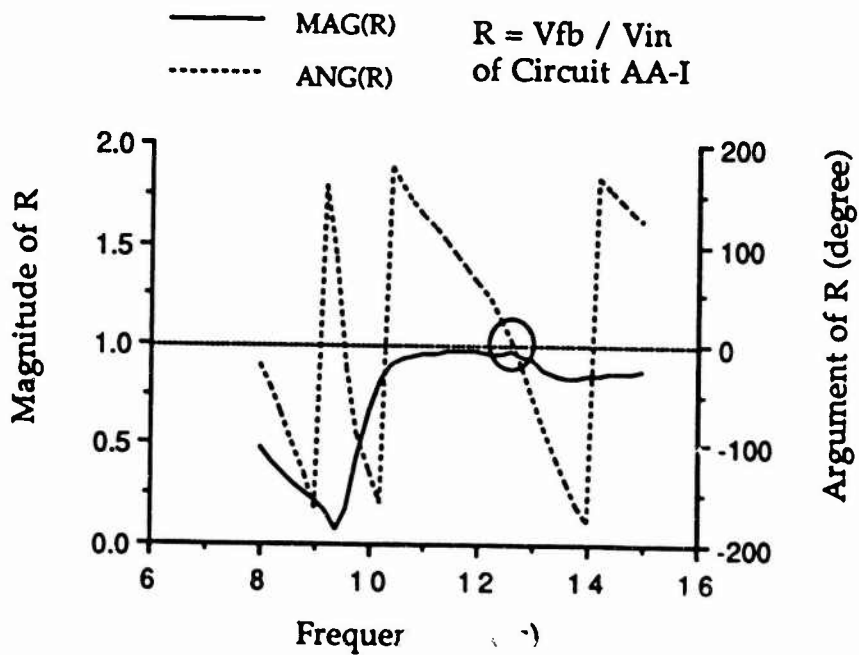


Fig. 6.10 Variation of R with Frequency of Active Integrated Antenna

Table III : Tuning Range Comparison
of Optically Controlled Active Integrated Antenna

Circuit		Operating Frequency (V _{ds} =4.0 V)	Electrical	Optical (Halogen Lamp)
AA-I	(Simulation)	12.6 GHz	5 MHz	--
	(Experiment)	12.5 GHz	145 MHz	50 MHz
AA-II (Experiment)		10.8 GHz	252 MHz	63 MHz
		12.1 GHz	250 MHz	47.5 MHz

6.3.3 Antenna Pattern

The obtained antenna patterns were compared with the theoretical patterns in Fig. 6.11. These antenna patterns at 12.1 GHz indicate the radiation not from a $1\lambda_s$ slot (designed frequency) but from the $1.21\lambda_s$ slot (circuit operation frequency). Although, due to the defects of the experiment set-up, the antenna pattern was distorted in the observation angle beyond 45° , the agreement between the theoretical values and the experimental data within 40° is good. In addition, there was no significant difference between the no-illumination pattern and illumination pattern.

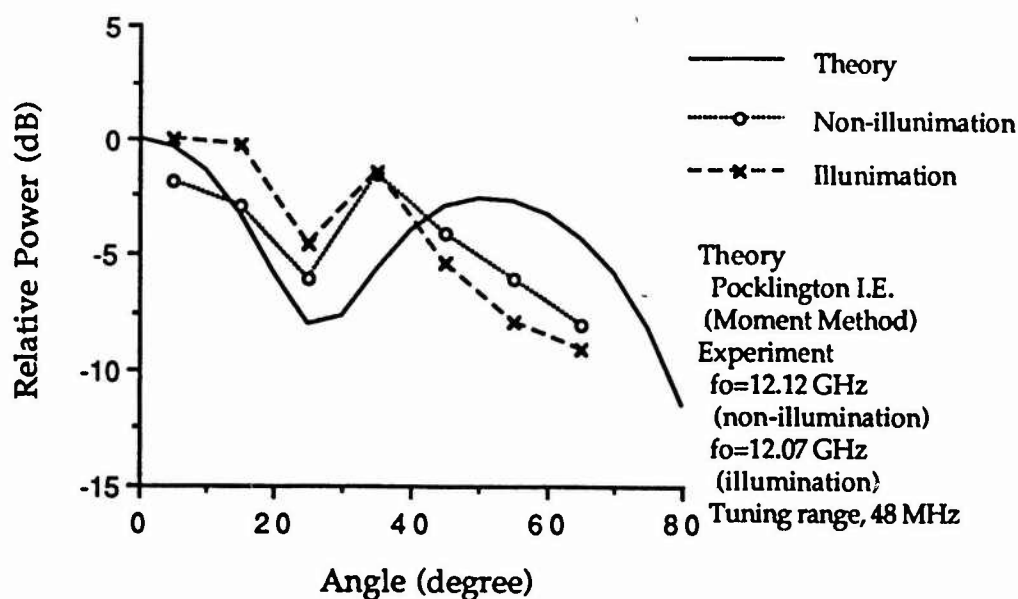


Fig. 6.11 Antenna Pattern Comparison of Optically Controlled Active Integrated Antenna

6.4 2-element Optically Controlled Uniplanar Linear Array

6.4.1 Configuration

The three types of 2-element uniplanar arrays were made by a hybrid MIC technique. The first is the array using a GaAs MESFET[49], while the second is the array using an AlGaAs/GaAs HEMT. The third array uses AlGaAs/InGaAs pseudomorphic HEMT. These three FET's were used to make the difference of illumination effect clear[50]. As an optical source, the halogen lamp was also used. In order to demonstrate a topology for uniplanar monolithic integrated circuit technology, high dielectric constant substrate ($\epsilon_r=10.5$: Duroid 6010) was selected. In the case of the MESFET, the slot radiator coupled with the CPW has dimensions of $0.80 \lambda_s$ by $0.062 \lambda_s$

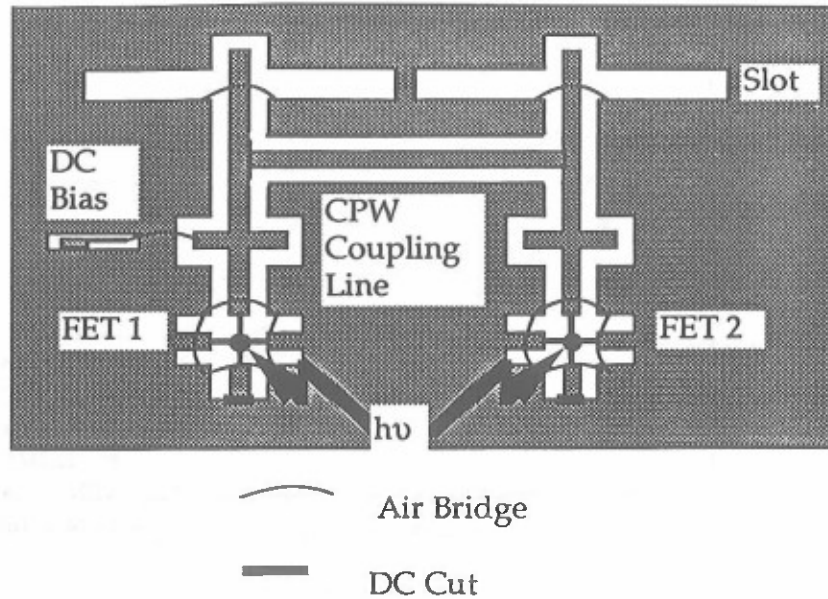


Fig. 6.12 2-element Uniplanar Linear Array

designed at 10 GHz. Meanwhile, in both the cases of the GaAs HEMT and the pseudomorphic HEMT, the dimensions of the slot were $0.51\lambda_s$ by $0.031\lambda_s$ at 10 GHz. These dimensions were determined by the preliminary experience. The configuration of a 2-element active integrated antenna is shown in Fig. 6.12. Each oscillator was designed by using small signal S-parameters. A unit active antenna has a double matching stub configuration. One matching stub consists of a CPW double stub and another constitutes a CPW-slot cross junction at the top of each unit active antenna as shown in Fig. 6.12. A single CPW with the length of $1\lambda_c$ and the characteristic impedance of $50\ \Omega$ was used to accomplish strong coupling between the oscillators. The two modes resulting from the signal phase from the oscillator were incorporated in the circuit design by using the appropriate stub. Due to the use of a high

dielectric constant substrate, physical separation between two slots can be reduced with the length of the coupling CPW of $1 \lambda_c$ which corresponds to $0.55 \lambda_0$ at 10 GHz. Since the separation became less than $1 \lambda_0$, problems of grating lobes are avoided.

6.4.2 Experimental Results

The 2-element MESFET active integrated antenna array operated at 8.8 GHz with $V_{ds}=3.58$ V and V_{gs} =floating gate as shown in Fig. 6.12. Therefore, only one DC power supply for V_{ds} was required to obtain the operating frequencies. The package-type FET used was NE72084. The optical control was carried out by illuminating the cap-removed package-type FET with a halogen lamp in these three cases. Air bridges are provided to suppress unwanted modes in the CPW circuit. The cause of the lower operating frequency may be due to mismatching of the CPW-slot cross, since the receiving power is relatively small. Using this circuit, an optical tuning range was measured and a maximum tuning range of 70 MHz at 8.8 GHz was obtained as shown in Fig. 6.13. Note that only one FET was illuminated. In addition, antenna patterns were observed. Fig. 6.14 shows the typical antenna patterns. No significant change occurs in the antenna pattern due to illumination. Under the strong coupling condition, illumination of the oscillator may only create a change of the resonant frequency.

The 2-element GaAs HEMT active integrated antenna array operated at 10.4 GHz under $V_{ds}=3.5$ V and a floating gate condition. The GaAs HEMT used was NE 32184A. Relatively large receiving power results from good

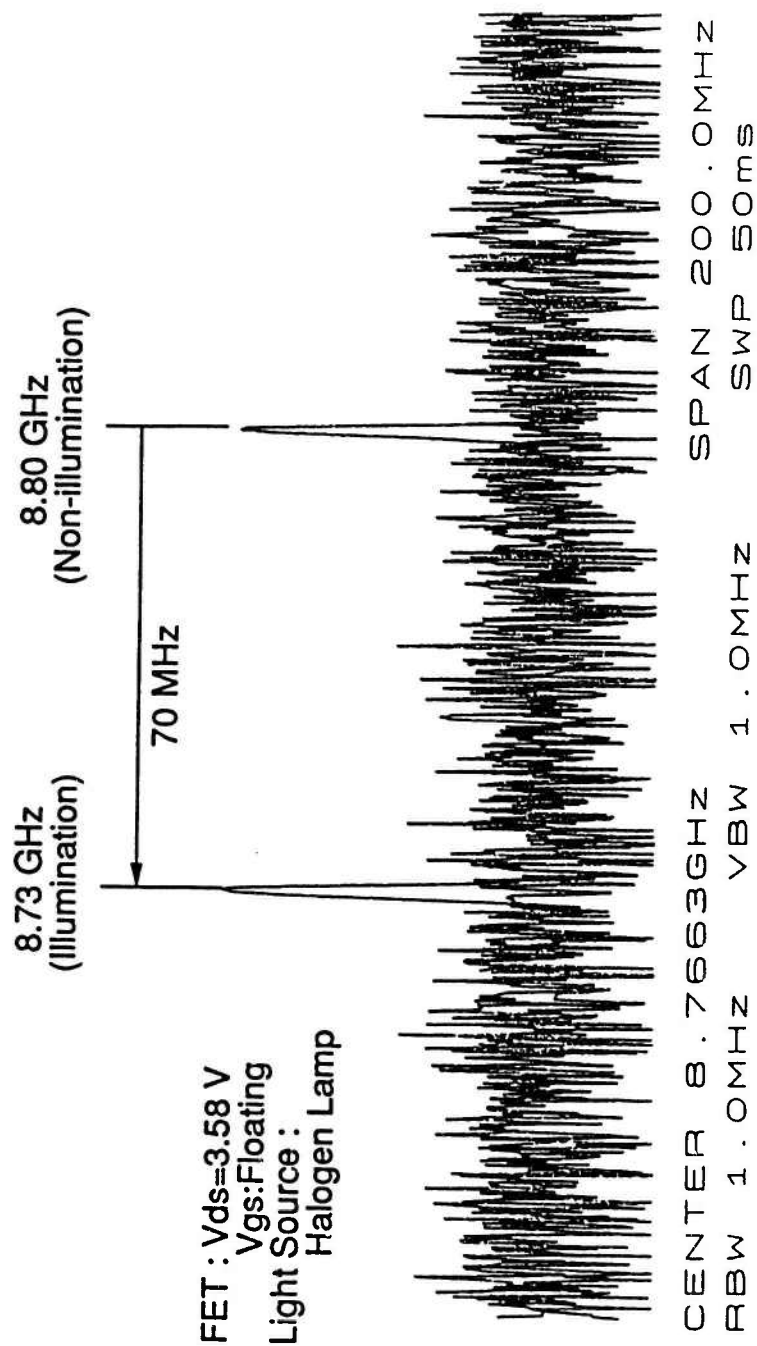
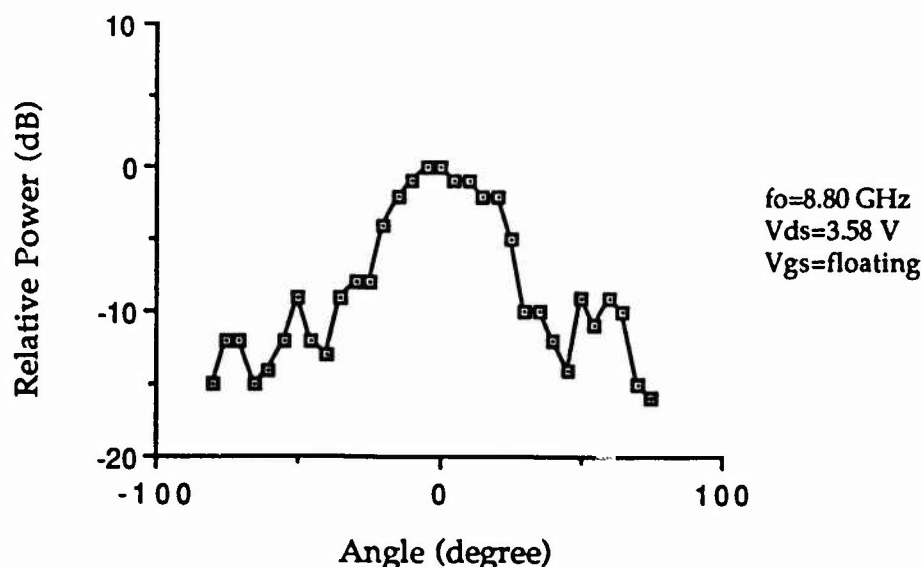


Fig. 6.13 Operation Spectrum Shift
 of Optically Controlled Active Integrated Antenna



**Fig. 6.14 Antenna Pattern of 2-element
Optically Controlled Uniplanar Linear Array**

matching at the CPW-slot cross junction as well as the CPW cross junction. The maximum optical tuning range with single-oscillator illumination was 7 MHz around 10.4 GHz with $V_{ds}=1.5$ V as shown in Fig. 6.15, while a very small tuning range was measured with $V_{ds}=4.4$ V at 10.4 GHz. Compared with the case of the MESFETs, the tuning range was one-tenth.

The third is the AlGaAs/InGaAs pseudomorphic HEMT (NE 32484) circuit operating at 10.5 GHz with $V_{ds}=2.0$ V. By tuning V_{ds} , the maximum tuning range of this circuit is 10 MHz as shown in Fig. 6.16. When V_{ds} increases, the characteristic of the tuning range of the MESFET is different from that of the GaAs HEMT and the pseudomorphic HEMT as shown in Fig. 6.17. This results from the difference of photo detection mechanisms. More details should be investigated by a large signal analysis with equivalent circuit parameters dependent on photon energy.

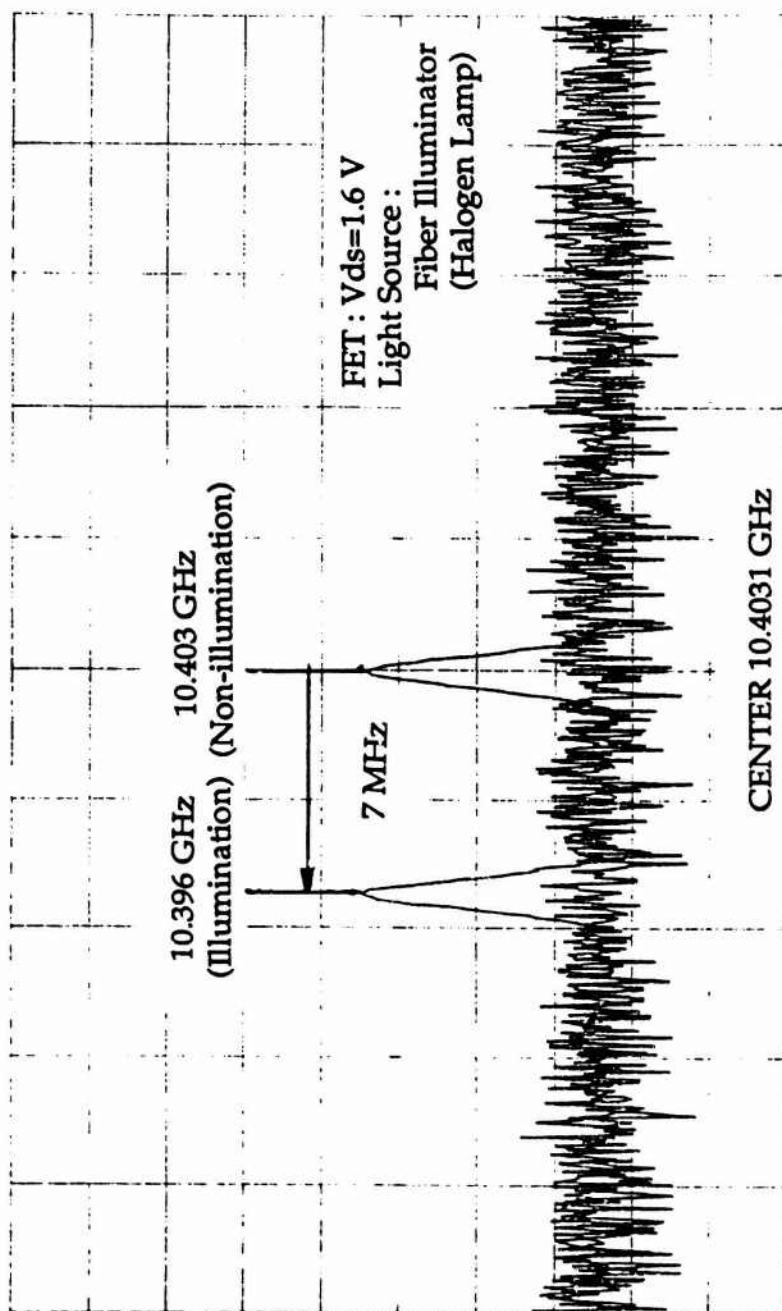


Fig. 6.15 Operation Spectrum Shift of 2-element Optically Controlled Uniplanar Linear Array Using GaAs HEMT

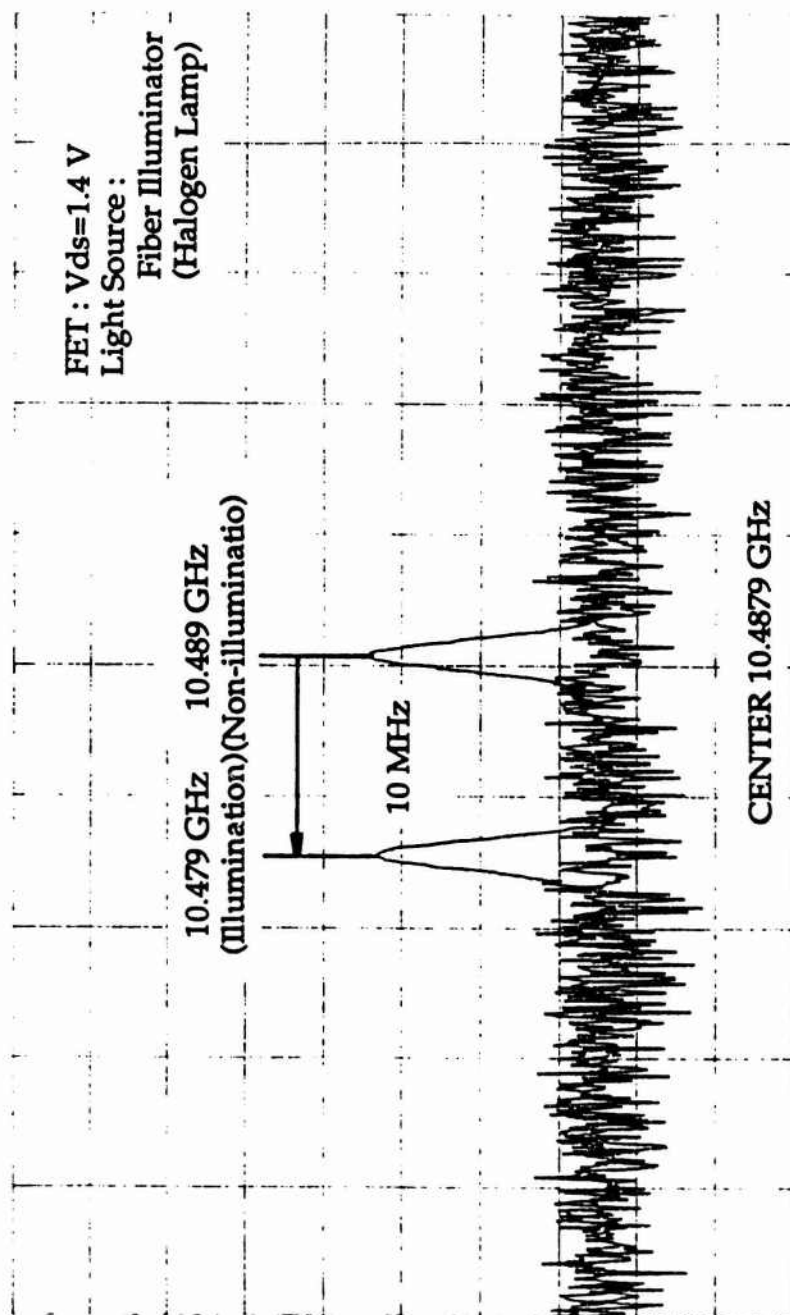


Fig. 6.16 Operation Spectrum Shift of 2-element Optically Controlled
 Uniplanar Linear Array Using Pseudomorphic HEMT

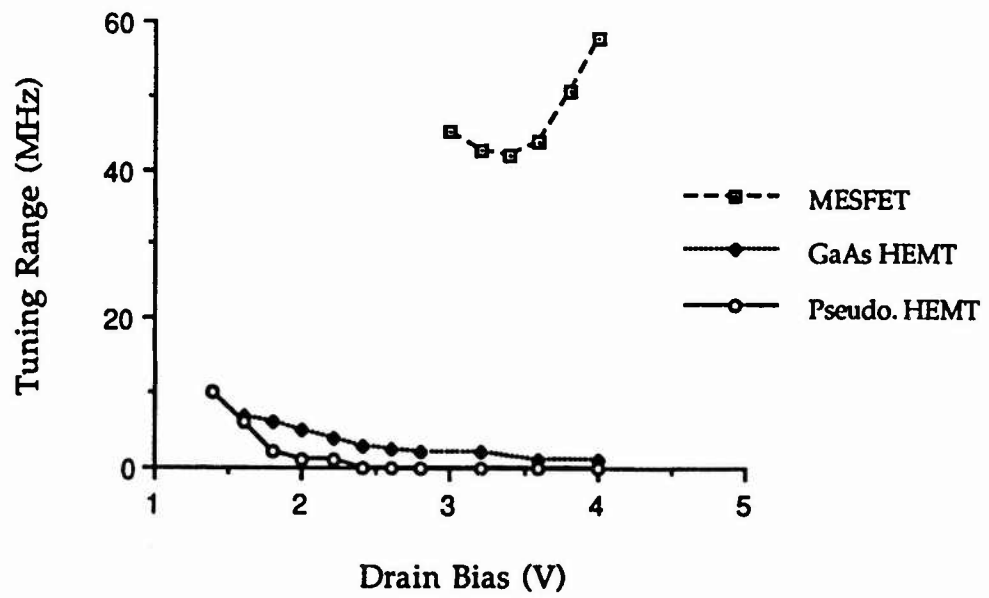


Fig. 6.17 Comparison of
Voltage Dependent Tuning Range

Chapter VII

Conclusions

7.1 Summary

In this dissertation, several methods for the generation of quasi-optical power using slots and FET's have been studied. Many examples for layered and uniplanar active antennas and quasi-optical power combining arrays have been demonstrated.

The prototype active antenna using slot antennas taking into account the configuration useful for MMIC technology are made at first. The oscillator was designed with $-50\ \Omega$ not with $-150\ \Omega$ (three times of the load resistance). The steady state oscillator frequency was confirmed by the large signal analysis using the entire circuit model including the frequency dependent slot input impedance. The tuning range of 100 MHz was obtained at 9.4 GHz by controlling applied DC voltages. To confirm the effectiveness of this design concept at higher frequencies, the active antenna designed at 25 GHz was fabricated. It oscillated at 24 GHz and the agreement of the experimental antenna patterns from both the 9.3 GHz circuit and the 24 GHz circuit with the theoretical pattern is very nice. It was confirmed that this design technique can be applied to the quasi-optical power combining array for higher frequencies. In addition, since this planar active antenna has a simple configuration, this circuit can be fabricated monolithically.

The CPW active antenna using a high dielectric constant substrate to demonstrate the topology for a uniplanar MMIC was also designed at 10 GHz. In spite of involving many unknown factors from the CPW cross junction and the CPW-fed slot, the circuit operated at 8.5 GHz using the same concept as that of the microstrip active antenna. Based on this result, it is facilitated to fabricate the uniplanar quasi-optical power combining array.

Based on the successful results of the active antenna, the design technique described above was applied to the power combining arrays. The feature of the quasi-optical power combining array studied here is the use of the strong coupling technique through the direct connection by a single transmission line. When the linear arrays were designed, the method for the in-phase signal from the adjacent oscillators and the in-phase radiation from each slot were incorporated. The former was attained by controlling the length of the coupling line. The latter was accomplished by inserting an additional $\lambda/2$ transmission line. From the analytical point of view, this coupling line was replaced by an appropriate stub to consider the modes between the adjacent oscillators.

The 6-element periodic and nonperiodic linear arrays operated around 16 GHz. This operating frequency agreed with the predicted operating frequency by the passive part analysis of the circuit and the large signal analysis. The sharp main beams from the antenna pattern measurement agreed with the theoretical pattern very well. The tuning range of the nonperiodic array increased with 75 % compared with that of the periodic

array. To operate the linear array at higher frequencies, the second harmonic spatial power combining array were fabricated. The highest operating frequency in this study was 40 GHz. The second harmonic power was spatially and effectively separated from the fundamental frequency power. For the uniplanar array, 2-element and 4-element quasi-optical power combining arrays using CPW's were also demonstrated. The 4-element second harmonic spatial power combining array operated at 15 GHz. In these cases, only one DC power supply for V_{ds} was required. These results enables us to realize a monolithic millimeter-wave quasi-optical linear array using a large number of FET oscillators.

For the design of the 2-dimensional array, the impedance matching for the multi-feed network as well as the in-phase signal from the oscillator and the in-phase radiation from the slot was taken into account. The design and experimental results of a 2x2 quasi-optical spatial power combiner was reported as a prototype of two dimensional quasi-optical power combiner array. The slot input impedance was incorporated into the circuit designs to evaluate the appropriate mode for the circuit operation. In the H-plane and the E-plane of the 2x2 quasi-optical power combiner array operating at 19 GHz, sum radiation patterns were obtained. Good agreement between the experiment and the theory was obtained around mainlobes in both radiation patterns. By making use of the coupling lines, only one bias network for the drain was necessary. The problem of the grating lobe can also be alleviated

by the use of a high dielectric constant substrate since the distance between the antennas can be reduced in terms of free space wavelength.

By using the successful results from the dual polarized array with 1 oscillator and 4 slots, 16-element 2-dimensional quasi-optical array operating at 7.8 GHz was demonstrated. Due to the different slot alignment to each polarization, two different antenna patterns were obtained. These design concepts are easily adapted for the 2-dimensional monolithic quasi-optical power combining array at higher frequencies using a large number of FET's. In addition, using the technology demonstrated in this study, a compact and potentially low-cost quasi-optical power combining array can be realized.

The FET can be used not only as an active element but as a passive element by designing the FET circuit as a reactive input impedance. The prototype quasi-optical transmitter using a slot and two reactive FET circuits was demonstrated. The structure specifically provides a way to create the wide-band characteristic in the layered planar antenna configuration. Two reactive MESFET's on the slot work as tuning stubs. The resonant frequency of the slot shifted over a range of 1 GHz around the center frequency of 10 GHz (10% tuning range) with negligible changes in the radiation pattern.

The optical illumination of MESFET's in the active integrated antenna circuit was demonstrated. This technique was applied to the oscillator as well as the reactive FET. By optically tuning the reactance of the MESFET, the electrical length of the slot antenna and the circuit operation frequency were

tunable without changing the radiation pattern significantly. In addition, to investigate the illumination effect on the FET's, the GaAs HEMT and pseudomorphic HEMT operating at 8.8 GHz were illuminated by the optical source. Their tuning ranges became one tenth of that of MESFET. The advantage of optical illumination for the active integrated antenna includes simplification of the control circuits, since it is not necessary to provide the control circuits on the chip. Therefore, chances of interference between the RF and control circuit can be reduced and flexibility of design can be enhanced.

7.2 Suggestions for Future Research

Most of the technologies described in this dissertation are of planar construction and are suited for fabrication in monolithic wafer-scale (not chip-scale) integrated circuit forms. Although the techniques mentioned in this study are still in its infancy, realization of simple, multi-functional and compact transceivers can be facilitated with potentially low cost by combining the quasi-optical technology with the optical control method. Further, this technology is very promising for application at millimeter-wave frequencies where a reasonable power output is needed.

The followings are the suggestions for future research. All of them are very important for radars and personal communication.

- (a) Wafer-scale quasi-optical power combining array using microstrip lines or CPW's

Using the techniques described in this study and the MMIC technology, a wafer-scale array can be made on a semiconductor substrate. For this

purpose, smaller antenna such as a slot in a multi-layered substrate and an aperture coupled microstrip patch antenna should be considered to make use of the area of the wafer as effectively as possible. In addition, in order to avoid a mechanical strength problem for the microstrip feed array, a thick substrate should be used. For the CPW feed array, a small antenna and a strong coupling method should be studied.

(b) Conformal chip array

It is possible to make one unit cell of the quasi-optical power combining array in one chip, since the external cavity for the coupling is not required. By connecting with each other, the array surface can have curvature. The connection method, the small antenna and the phase shifter must be studied.

(c) Beam steering and beam switching

The electronically and optically controlled reactive FET can work as a phase shifter. This phase shifter enables radar to steer and switch the beam. It should be studied to obtain a large dynamic tuning range from the reactive FET for a monolithic circuit.

(d) Modified harmonic balance analysis

When the circuit characteristics were investigated, the harmonic balance analysis was used. Although this analysis enables us to analyze the circuit with nonlinear parameters, the convergence problem sometimes arises. To simulate the circuit with good accuracy, the harmonic balance analysis should be modified in such a way to extrapolate the characteristic around nonconverging regions.

(
(e) Analysis for CPW cross junction and CPW-slot cross

To predict an operating frequency accurately in the quasi-optical circuit, data of circuit parameters should be included in the design as much as possible. In this study, unknown parasitic reactances due to discontinuities shifted the operating frequency from the design frequency. The CPW cross junction and CPW-slot cross may be denoted as series and/or shunt capacitances. More efforts on these discontinuities are strongly expected for the design of a uniplanar active integrated antenna.

If these items are resolved, it is believed that the new technology described in this study can make the life of people more convenient.

Bibliography

- [1] T. Itoh, "Active Antennas", Journees In't De Nice Sur Les Antennes, France, Nov.1990, pp 435-438
- [2] S. Kawasaki and T. Itoh, "Active Integrated Antenna Based on Slots with FETs", 1992 URSI Int'l Symposium on Signal, Systems and Electronics, Paris, France, Sep. 1992, pp. 584-587.
- [3] K.D. Stephan and T. Itoh, "A Planar Quasi-Optical Subharmonically Pumped Mixer Characterized by Isotropic Conversion Loss", IEEE Trans. Microwave Theory Tech., vol. 32, pp 95-102, January 1984
- [4] S. Kawasaki and T. Itoh, "Active Planar Integrated Antenna Technology" (Invited Talk), The Fifth Australian Symposium on Millimetre and Submillimetre Waves, Salisbury Australia, August 1992.
- [5] S. Kawasaki and T. Itoh, "Quasi-Optical and Active Antenna Technology", the Conference Proceedings of MM-92, Brighton, UK, Oct. 1992, pp. 311-316.
- [6] Y. Yoshimura, "A Microstripline Slot Antenna" IEEE Trans. Microwave Theory Tech., vol.20, pp760-762, Nov. 1972.
- [7] S. Kawasaki and T. Itoh, "A Layered Negative Resistance Amplifier and Oscillator Using a FET and a Slot Antenna", 1991 IEEE MTT-S Int'l Microwave Symposium Dig. vol. 3, Boston, MA, June 1991, pp 1261-1264
- [8] B. Kormanyos and G. Rebeitz, "Active CPW-fed Slot Antennas for Power Combining Applications", The Third Int'l Symp. on NASA Space Terahertz Technology, Ann Arbor MI, Mar. 1992. pp. 32-36.

- [9] J.W. Mink, "Quasi-optical Power Combining of Solid-State Millimeter-wave Sources", IEEE Trans. Microwave Theory Tech., vol MTT-34, pp. 273-279, Feb. 1986
- [10] Z.B. Popovic, R.M. Weikle II, M. Kim and D.B. Rutledge, "A 100-MESFET Planar Grid Oscillator", IEEE Trans. Microwave Theory Tech., vol. 39, pp 193-200, Feb. 1991
- [11] J. Birkeland and T. Itoh, "A 16 Element Quasi-Optical FET Oscillator Power Combining Array with External Injection Locking" IEEE Trans. Microwave Theory Tech., vol.40, pp475-481, Mar. 1992.
- [12] R.A. York and R.C. Compton, "Quasi-Optical Power Combining Using Mutually Synchronized Oscillator Arrays", IEEE Trans. Microwave Theory Tech., vol. 39, pp 1000-1009, June 1991
- [13] S. Kawasaki and T. Itoh, "40 GHz Quasi-Optical Second Harmonic Spatial Power Combiner Using FETs and Slots", 1992 IEEE MTT-S Int'l Microwave Symposium Dig. vol. 3, Albuquerque, NM, June 1992, pp 1543-1546
- [14] S. Kawasaki and T. Itoh, "Quasi-Optical Planar Arrays with FET's and Slots", to be appeared in IEEE Trans. Microwave Theory Tech., Oct. 1992.
- [15] A. Mortazawi, S. Kawasaki and T. Itoh, "A Second Harmonic Power Combining Transceiver", The 3rd Asia-Pacific Microwave Conference Proceedings, Tokyo, Japan, Sep. 1990, pp 225-226
- [16] R. Simons, *Optical Control of Microwave Devices*, Artech House, 1990
- [17] A.A.A. de Salles, "Optical Control of GaAs MESFET's", IEEE Trans. Microwave Theory Tech., vol. 31, pp 812-820, Oct. 1983.
- [18] Y. Yamamoto, K-I. Kawasaki and T. Itoh, "Optical control of microwave

- active bandpass filter using MESFETs", 1991 IEEE MTT-S Int'l Microwave Symposium Dig. vol. 2, Boston, MA, June 1991, pp 655-658
- [19] M.A. Romero, A.L.A. Cunha and A.A.A. de Salles, "Theory and experiment for the HEMTs under optical illumination", 1991 IEEE MTT-S Int'l Microwave Symposium Dig. vol. 2, Boston, MA, June 1991, pp 495-498
- [20] A. Madgar, P.R. Herczfeld and A. Paoletta, "Analytical Model for Optically Generated Currents in GaAs MESFET's", IEEE Trans. Microwave Theory Tech., vol. 40, pp 1681-1691, Aug. 1992
- [21] S. Kawasaki and T. Itoh, "A Slot Antenna with Electronically Tunable Length", 1991 IEEE AP-S Int'l Symposium Dig., Canada, June 1991, pp. 130-133.
- [22] G. Gonzalez, *Microwave Transistor Amplifiers*, Printice-Hall, 1984.
- [23] S. Kawasaki and T. Itoh, "Optical Control of Active Integrated Antenna", Proc. of 22nd European Microwave Conference, Finland, August 1992, pp. 697-701.
- [24] D.M. Pozar, "A Reciprocity Method of Analysis for Printed Slot and Slot-Coupled Microstrip Antenna", IEEE Trans. Antennas Propagat., vol AP-34, pp. 1439-1446, Dec. 1986
- [25] S. Kawasaki and T. Itoh, "2x2 Quasi-Optical Power Combiner Array at 20 GHz", to be appeared in IEEE Trans. Microwave Theory Tech., Mar. 1993.
- [26] S.A. Maas, *Nonlinear Microwave Circuits*, MA: Artech House, 1988.
- [27] R.S. Elliott, *An Introduction to Guided Waves and Microwave*

Circuits, Prentice Hall, 1993.

- [28] K. Kurokawa, "Some Basic Characteristics of Broadband Negative Resistance Oscillator Circuits", *Bell Syst. Tech. J.*, vol. 48, pp. 1937-1955, 1969.
- [29] Joel Birkeland, Ph. D. dissertation, The University of Texas, Austin, 1989.
- [30] Touchstone & Libra Application, EEsof, Lindero Canyon, Westlake, CA.
- [31] D.B. Rutledge, D.P. Neikirk, and D.P. Kasilingam, "Integrated-Circuit Antenna", in *Infrared and Millimeter Waves*, vol. 10, K.J. Button, Ed. New York: Academic Press, 1983, pp. 1-87
- [32] C.A. Balanis, *Antenna Theory*, John Wiley & Sons, 1982.
- [33] C.A. Balanis, *Advanced Engineering Electromagnetics*, John Wiley & Sons, 1989.
- [34] W.L. Stutzman and G.A. Thiele, *Antenna theory and Design*, John Wiley & Sons, 1981.
- [35] R.S. Elliott, *Antenna Theory and Design*, Prentice Hall 1981.
- [36] K.D. Stephan and T. Itoh, "Recent Efforts on Planar Components for Active Quasi-Optical Applications" 1990 IEEE MTT-S Int'l. Microwave Symposium Dig., vol.3, Dallas, Tx, May 1990, pp1205-1208
- [37] R. Simons and R. Lee, "Planar Dielectric Resonator Stabilized HEMT Oscillator Integrated with CPW/Aparture Coupled Patch Antenna", the 1992 IEEE MTT-S Int'l Microwave Symposium, Albuquerque, NM, June 1992, pp. 433-436.
- [38] S. Kawasaki and T. Itoh, "24 GHz FET Oscillator with Slot Antenna for

(Quasi-Optical Transmitter", 16th In't Conf. on IR & MMW, Switzerland, Aug. 1991, pp 286-287

- [39] S. Nogi, J. Lin and T. Itoh, "Mode Analysis and Stabilization of a Spatial Power Combining Array with Strong Coupled Oscillators", to be appeared in IEEE Trans. Microwave Theory Tech., Oct. 1993.
- [40] S. Kawasaki and T. Itoh, "6-Element Periodic and Nonperiodic Linear Arrays for Quasi-Optical Spatial Power Combiner", 1992 Joint Symposia, URSI Radio Science Meeting, Chicago IL, July 1992, p 394
- [41] S. Kawasaki and T. Itoh, "Spatial Harmonic Power Combining Transceiver", Progress In Electromagnetics Res. Symp., Cambridge, MA, July, 1991, p.407.
- [42] S. Kawasaki and T. Itoh, "FET Quasi-Optical Spatial Power Combiner at 20 GHz with Three Oscillators and Slot Radiators in H-Plane", 1992 Asia-Pacific Microwave Conference, Adelaide , Australia, Aug. 1992, pp 751-754
- [43] S. Kawasaki and T. Itoh, "2x2 Quasi-Optical Power Combiner Array at 20 GHz", The Third In't Symp. on NASA Space Terahertz Technology, Ann Arbor MI, Mar. 1992, pp 37-44
- [44] J. Lin, S. Kawasaki and T. Itoh, "Optical Control of MESFET's for Active Filter and Active Antenna", to be appeared in the digest of the seventh international MIOP'93 Conference, Fairground Sindelfinger, Germany, May 1993.
- [45] J.P. McKelvey, *Solid State and Semiconductor Physics*, R.E. Krieger Publishing Company Inc., 1966.

- [46] S.M. Sze, *Physics of Semiconductor Devices*, 2nd Ed., John Wiley and Sons, 1981.
- [47] S. Kawasaki and T. Itoh, "Electronically and Optically Controlled Active Integrated Antenna" , The proceedings of the 1992 International Symposium on Antenna and Propagation, Sapporo, Japan, September 1992, pp. 821-824.
- [48] S. Kawasaki and T. Itoh, "Progress of Optical Control of Quasi-Optical Oscillators Using MESFETs", 17th Int'l Conf. on IR & MMW, Pasadena, CA, Dec. 1992, pp. 354-355.
- [49] S. Kawasaki and T. Itoh, "Optical Control of 2-element CPW Active Integrated Antenna with Strong Coupling", to be appeared in 1993 IEEE AP-S Int'l Symposium Dig., Ann Arbor MI, June 1993.
- [50] S. Kawasaki and T. Itoh, "Optical Tuning Range Comparison of Uniplanar Active Integrated Antenna Using MESFET, GaAs HEMT and Pseudomorphic HEMT", to be appeared in the digest of The Fourth Int'l Symp. on NASA Space Terahertz Technology, Los Angeles, CA, Mar. 1993.